Methods for Inverse Calculation of Distributed Static, Distributed Harmonic, and Traveling Dynamic Structural Loads

by

Benjamin Keith Morris

(Under the Direction of R. Benjamin Davis)

Abstract

Inverse input estimation problems, in which a set of inputs are estimated from sparse, noisy system response measurements, are common in engineering practice. In structural engineering applications, input estimation problems manifest when the forces on a structure are estimated from measurements of structural motion. Structural inverse problems are almost always ill-conditioned, and naïve system inversion yields unacceptable force estimates that amplify noise in the response data. While input force estimation techniques have been well-studied for cases where discrete forces act at known locations, little work has been done about how these techniques can be extended to cases where the force locations are unknown or the forces are distributed over the domain.

This dissertation presents three methods of solving distributed and moving force estimation problems for each of the three types of temporal loading: static, harmonic, and general dynamic. The techniques presented here supplement common techniques for estimating concentrated loads at known locations with additional techniques that enable distributed and moving load estimation. First, a method of estimating distributed static loads is presented along with a method for intelligently placing strain sensors. Second, a method for estimating distributed harmonic forces using a novel form of Tikhonov regularization is described. Lastly, we outline a Kalman filter-based method for estimating moving loads. Because these techniques are all extensions of standard methods, they should be immediately applicable to a wide variety of engineering problems. Addi-

tionally, this manuscript can be viewed as a tutorial that describes the state-of-the-art of structural input estimation techniques.

INDEX WORDS: Structural dynamics, Regularization, Inverse problem, Input estimation, Kalman filter, Transient

Methods for Inverse Calculation of Distributed Static, Distributed Harmonic, and Traveling Dynamic Structural Loads

by

Benjamin Keith Morris

B.S., The University of Georgia, 2018

M.S., The University of Georgia, 2020

A Dissertation Submitted to the Graduate Faculty of The University of Georgia in Partial Fulfillment of the Requirements for the Degree

Doctor of Philosophy

Athens, Georgia

2025

Methods for Inverse Calculation of Distributed Static, Distributed Harmonic, and Traveling Dynamic Structural Loads

by

Benjamin Keith Morris

Major Professor: R. Benjamin Davis

Committee: Beiwen Li
Jin Ye
WenZhan Song

Electronic Version Approved:

Ron Walcott
Dean of the Graduate School
The University of Georgia
August 2025

Acknowledgements

This manuscript represents the end result of an enormous effort over the past five years. At times the journey has seemed more Sisyphean than Herculean, but just as Edison discovered one thousand ways of building an ineffective light bulb before landing on a method that worked, I have proved to myself that grit and perseverance are just as important as raw skill and intelligence. For that reason, I would like to first acknowledge for the sake of my future self that by pure determination, I was able to do something really, really hard. Ben, never forget that your determination is an amazing quality.

To my loving wife Enid, who has always been my light when everything seemed hopeless, and who always seems to know what I need before I realize it myself. There is no chance I would have finished this process without your support.

To my incredible advisor Dr. Ben Davis, who saw something in me seven years ago and decided to mentor me into the scholar I am today. You have given me a love for research in spite of all the challenges, and I couldn't have asked for a better mentor. To my committee members who were always available for questions and discussions pertaining to my research and other academic curiosities. To my lab mates over the years, including but not limited to Ryan, Eetu, Haynes, Haning, Bianca, Cody, Mark, Keaton, Jesse, and Ava, who were always available to discuss academic problems or just laugh and pass the time. Lastly, to my ever-supportive parents Julie and Keith Morris, and my in-laws Nghiem and Sampson Truong who have always been there to help with anything Enid and I need. How lucky I am to have such a robust support system.

Contents

List of Tables

List of Figures

Nomenclature

Roman Symbols

$\boldsymbol{A}$ Force magnitude vector

A (Ch. 2) Influence matrix

A (Ch. 3) Area

A (Ch. 4) Augmented state transition matrix

A^* Discrete augmented state transition matrix

$\boldsymbol{a}$ Vector of control point locations

$\boldsymbol{B}$ Force spacing vector

B Interpolation matrix

C Modal damping matrix

C_M Constant of integration from moment equation

C_θ Constant of integration from slope equation

C_V Constant of integration from shear equation

C_w Constant of integration from deflection equation

c Speed of sound

d Euclidean distance

E Young's modulus

e Mean integrated relative error

F Force location matrix

F_x Distributed truth force

f Arbitrary function

G Noise transition matrix

G^* Discrete noise transition matrix

H (Ch. 3) FRF matrix

H (Ch. 4) Measurement matrix

$\bar{H}$ Pseudo measurement matrix

H_x Physical measurement matrix

h Beam thickness

i (Ch. 3) Imaginary unit

I (Ch. 2) Area moment of inertia

I (Ch. 4) Identity matrix

K (Ch. 2) Condition number ratio

K (Ch. 4) Modal stiffness matrix

K_g Kalman gain matrix

k (Ch. 2) Number of control points

k (Ch. 4) Timestep index

l (Ch. 4) Distance along beam

l (Ch. 2) Number of loading segments

L (Ch. 2 & 4) Beam length

L (Ch. 3) Plate height

M Internal moment

m (Ch. 2) Number of sensors

N Number of generalized coordinates

N_f Number of pulses

N_p Number of peaks in time window

N_s Number of simultaneous pulses on the structure

N_τ Number of pseudo measurement iterations

n_f (Ch. 3) Number of force parameters in each direction

n_s (Ch. 3) Number of measurements

P Estimation error covariance

$\hat{P}$ Complex-valued steady-state response amplitude

$\bar{P}$ Mean peak magnitude

p (Ch. 2) Control point magnitude

p (Ch. 3) Probability density

Q Augmented model covariance matrix

Q^* Discretized augmented model covariance matrix

Q_w Model covariance matrix

Q_z Force covariance matrix

$\boldsymbol{q}$ Generalized coordinates vector

$\hat{\boldsymbol{q}}$ Augmented state vector

q (Ch. 2) Transverse load

q (Ch. 3) Penalty term norm

R (Ch. 3) Cholesky decomposition of covariance matrix inverse

R (Ch. 4) Measurement covariance matrix

R_γ ℓ_1 pseudo measurement variance

r Percentage of beam length

s (Ch. 2) Segment number index

s (Ch. 3) Correlation strength parameter

T Total simulation time

t Time

Δt Timestep duration

t_p Times at which peaks occur

U Harmonic force magnitude

$\boldsymbol{u}$ Force vector

u Force

$\bar{u}$ Normalized force integral

$\hat{u}$ (Ch. 3) Control point magnitude

$\hat{u}$ Force integral

$\boldsymbol{v}$ Measurement noise vector

W Plate width

$\boldsymbol{w}$ Model noise vector

w Transverse deflection

$\boldsymbol{x}$ Physical coordinates vector

x Distance along the beam

$\bar{x}$ Distance along the beam as a fraction of beam length

$\hat{\boldsymbol{x}}$ Physical augmented state vector

x, y Spatial coordinates

Y Acceleration response magnitude

$\boldsymbol{y}$ Measurement vector

y Physical displacement

$\boldsymbol{z}$ Force noise vector

Greek Symbols

α Decay parameter

β Boundary admittance

ε (Ch. 2) Maximum sxtrain

ε (Ch. 4) Mean squared error

ϵ_γ ℓ_1 threshold parameter

η Modal displacement

γ (Ch. 4) ℓ_1 regularization parameter

γ (Ch. 3) Poisson's ratio

κ (Ch. 2) Condition number

κ (Ch. 3) Condition number of H

κ (Ch. 4) Truth force magnitude

Λ Modal damping ratio matrix

λ (Ch. 2) Singular values of $[A]$

λ (Ch. 3) Regularization parameter

λ (Ch. 4) Truth force center point

μ Mean value

μ_f, μ_c, μ_l Spatial functions

ν_f, ν_c, ν_l Spatial functions

ν (Ch. 3) Harmonic pressure magnitude

ν (Ch. 4) Flow velocity

ν_t (Ch. 3) Truth harmonic pressure magnitude

ν_t (Ch. 4) Truth pulse velocity

Ω Natural frequency matrix

ω Forcing frequency

ω_h Upper bound on frequency range

ω_j j^{th} Natural frequency

ω_l Lower bound on frequency range

Φ Mass-normalized mode shape matrix

$\tilde{\Phi}$ Augmented mode shape matrix

ϕ Phase angle

ρ Density

Σ Covariance matrix

Σ_n Noise covariance matrix

$\Sigma_{\hat{U}}$ Force covariance matrix

σ (Ch. 2) Maximum normal stress

σ (Ch. 3) Singular value of H

σ (Ch. 4) Truth force standard deviation

σ_n Noise covariance scaling factor

σ_u Force covariance scaling factor

τ_f, τ_c, τ_l Spatial functions

$\boldsymbol{\xi}$ (Ch. 2) Sensor configuration

ξ (Ch. 3) Sensor location

ξ (Ch. 4) Location along flow direction

ζ_j j^{th} Modal damping ratio

Super/Subscripts

$+$ After measurement update

$-$ Before measurement update

a Approximate

b Bayesian inference

$\dagger$ Pseudo inverse

H Conjugate transpose

i, j (Chs. 2 & 4) Indices

j, k (Ch. 3) Indices

max (Ch. 2 & 3) Maximum

max (Ch. 4) Largest magnitude

min (Ch. 2 & 3) Minimum

n Naïve

o Optimal

p Prior

r (Ch. 2) Rule-of-Thumb

r (Ch. 3) Reduced

SPL Units in dB (SPL representation)

T Transpose

t (Chs. 2 & 4) Truth

t (Ch. 3) Tikhonov regularization

Acronyms

AKF Augmented Kalman Filter

CC Clamped-Clamped

CCCC Clamped-clamped-clamped-clamped

CF Clamped-Free

CS Clamped-Simply-Supported

DFT Discrete Fourier transform

DOF Degree(s) of Freedom

EI Effective independence

FEA Finite element analysis

FRAC Frequency response assurance Criterion

FRF Frequency response function

FRM Frequency Response Matrix

K-LD Kullback–Leibler divergence

LDL Linearly Distributed Load

MAC Modal assurance criterion

MCMC Markov-Chain Monte Carlo

PDF Probability density function

SNR Signal-to-noise ratio

SPL Sound pressure level

SS Simply-Supported

UDL Uniformly Distributed Load

Chapter 1

Introduction

1.1 Motivation

Classical texts on engineering science usually describe physical processes in terms of estimating a system's response to a known input. For instance, the temperature of a solid mass due to a known heat flux over a portion of the surface, the fluid pressure at a point in a domain given the known free-stream velocity, and the displacement at the tip of a beam due to a known force applied to the beam all represent system responses to known inputs. In all of these cases, the known system inputs are used with the system equations to yield an estimate of the system response that is typically stable to small changes in the input.

These descriptions of physical systems are adequate for understanding the underlying physics and for many applications. However, there are many practical applications where the system inputs are unknown and difficult to measure, but the system response can be easily measured. For instance, accelerometers are relatively inexpensive, small, and simple to configure compared to load cells, and can capture the response of a structure at any point while the load cell must be collocated with the force to get an accurate measure of the input. In addition, the number of force sensors required to resolve a distributed load is typically impractical. It is therefore desirable to estimate the force on a structure using structural response measurements. Inverse problems, in which the input to physical systems or system parameters are estimated using sparse measurements of the system response, frequently appear in applications such as control systems, model validation, and structural health monitoring. Structural system identification and input estimation techniques are examples of inverse problems in the structural engineering domain. System identification problems are concerned with the estimation of structural parameters such as stiffness or damping, while input estimation problems are concerned with reconstructing the forces applied to a structure. In either case, structural re-

sponse measurements enable estimation. Although input estimation and system identification are both types of inverse problems with similar considerations, the techniques used to solve these classes of problems are largely disparate. The present work focuses on input estimation problems and describes several techniques for estimating forces on structures.

Fig. 1.1 shows the archetypal flow of inputs and outputs in an input estimation problem. The top row of objects represents the forward problem typical of most engineering science texts. The system is excited by a force configuration, and the result is an estimate of the full response of the system that is typically represented by displacement, strain, or acceleration. The inversion process begins by taking sparse and noisy measurements of the full response. The object "Sparse Measurements" in the flow chart has a dashed border to highlight the fact that it represents an estimate of a subset of the full response. The measurements are passed through a system inverse to yield a force estimate. Note that the system inverse is typically not a direct inversion of the system but is rather based on a numerical or empirical approximation of the forward system. The success of an input estimation technique is evaluated using an error metric between a known truth force and the force estimate. The final error metric is only used to evaluate the inversion method during testing, since the truth force is generally unknown in practice. Inverse problems (input estimation problems,

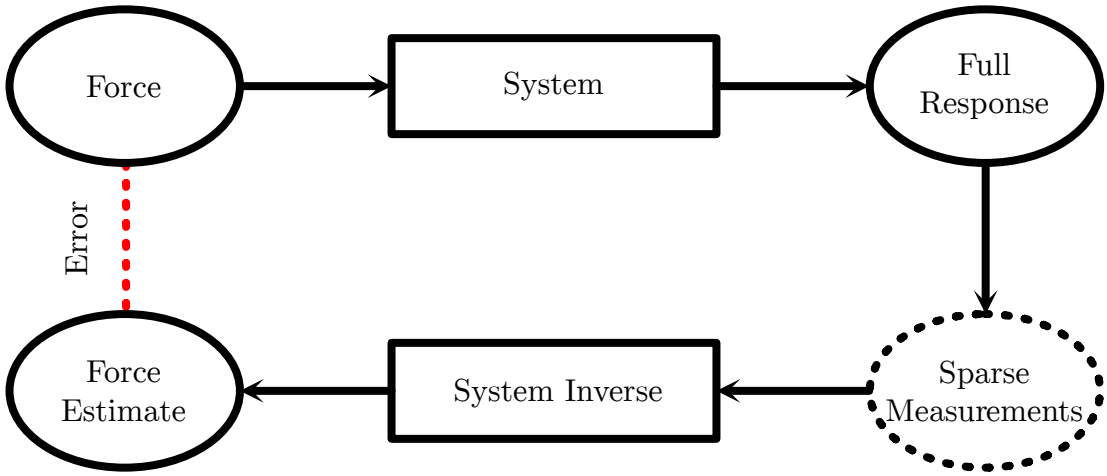

Figure 1.1. Flowchart showing the process of a general inverse problem.

in particular) are typically plagued with numerical difficulties. When the system equations are directly inverted, the resulting equations are often ill-conditioned, and yield input estimates that are extremely sensitive to noise in the response measurements. Further, the problem is ill-posed if the number of measurements

is less than the number of force parameters to be estimated, and the inversion process will not in general find a unique solution. Additionally, the quality of the force reconstruction depends on the amount of information provided by the measurements, which is in turn a function of the physical sensor configuration. Ill-conditioned and ill-posed inverse problems may be made well-conditioned and well-posed by including a regularization term that includes additional information about the expected form of the solution in the inversion process itself. Techniques for intelligent sensor system design have also been developed. The present work describes techniques for obtaining stable force estimates from sparse, noisy response measurements by combining common system inversion techniques with novel sensor placement and regularization techniques. In particular, this document focuses on estimating distributed static forces, distributed harmonic forces, and traveling dynamic forces.

1.2 Literature Review

This section presents a review of the relevant literature on structural input estimation problems. The review is divided into subsections that correspond to methods for solving static, harmonic, and dynamic force estimation problems. A map summarizing the techniques that fall under structural input estimation methods is shown in Fig. 1.2 for convenience. In the figure, the subdomains addressed by the present work are shown in blue.

While there are mathematical differences among the different classes of force estimation problems, there are also similarities. The motivation for developing solution methods is largely the same in all cases. Directly measuring the force applied to a structure is typically infeasible due to the system geometry, difficulties with installing the required types of sensors, or the number of sensors required to resolve the applied load. System inversion methods allow the force on the system to be estimated from sparse structural response measurements, which can be obtained from relatively inexpensive and simple to install sensors such as accelerometers or strain gauges.

Similar mathematical difficulties also exist for all types of inverse problems. When the number of force parameters to be estimated exceeds the number of available response measurements, the problem is underdetermined and ill-posed. In this case, it is impossible to find a unique solution, and force estimates are typically very inaccurate [1]. When the number of force parameters is less than or equal to the number of response measurements, the problem is overdetermined or even determined, and a unique solution can

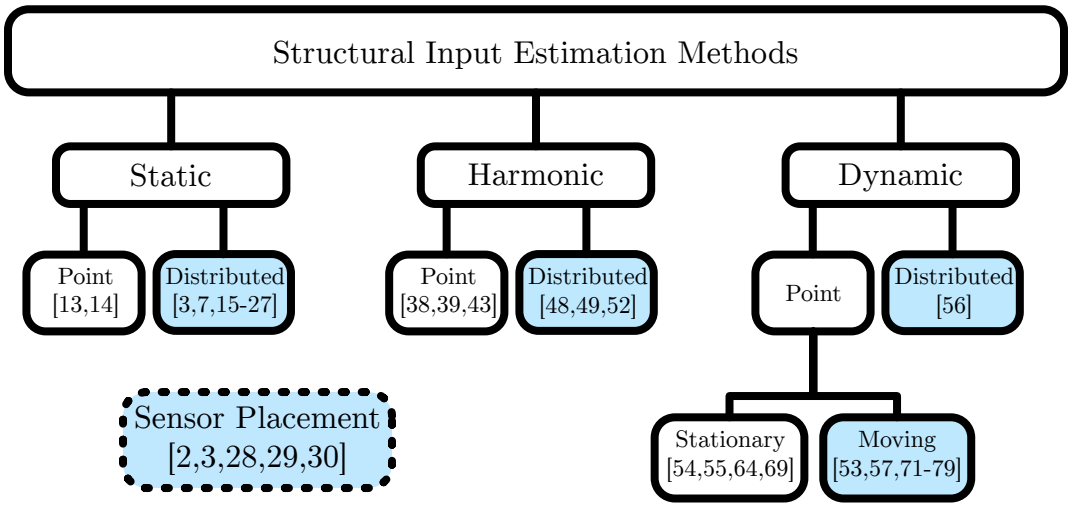

Figure 1.2. Structural input estimation problems tree with citations to works that detail methods of solving each problem type. Problems addressed in the present work are placed in blue boxes.

be found. The problem is often still ill-conditioned even in the overdetermined case, which means that the force estimate is highly sensitive to small changes in the response data [1]. Regularization and intelligent sensor placement methods can be used to improve the conditioning of inverse problems, and regularization can even effectively convert ill-posed problems to well-posed problems by introducing prior information about the solution. The details of the regularization scheme, the sensor placement method, and the inversion technique of the system depend on the type of force estimation problem.

1.2.1 Static Force Estimation

Engineering structures are routinely subject to static or quasi-static distributed loads such as those from pressure or thermal fields. However, the quality of force reconstruction from direct system inversion is typically sensitive to the locations at which the sensors are placed [2, 3]. Although algorithms exist to determine optimal sensor systems, little guidance is available for setting sensor placement in the absence of numerical models [2, 3]. Chapter 2 seeks to provide guidance for designing sensor systems on beam-like structures.

Methods for solving static inverse problems have been extensively studied [4]. Most of the current literature on static inverse problems focuses on applications of structural health monitoring, where structural damage is measured indirectly from quasi-static response data [4–12]. These structural health monitoring problems belong to the broad field of system identification, where the goal is to estimate—and identify changes to—system properties (*e.g.*, stiffness) using only response measurements. While inverse methods for system identification are powerful, they are not generally applicable to the input estimation problems considered here, where the goal is to calculate an applied force using only the measured response.

Inverse force estimation in static and quasi-static systems has also been studied, but not to the same extent as inverse methods for structural health monitoring. The influence coefficient methods model a linear relationship between force and response (typically in the form of strain) as an influence matrix [13–15]. A solution may be attempted by simply inverting the influence matrix, but more accurate solutions can often be found via regularization [16, 17] or rank reduction of the influence coefficient matrix [18, 19]. A Moore-Penrose pseudo-inverse may be used to achieve a least-squares solution for general rectangular influence matrices (corresponding to overdetermined or underdetermined systems). Creating the influence matrix requires the definition of a basis of candidate forces. The estimated load is a linear combination of these candidate forces. The early sets of candidates consisted of point loads at all relevant degrees of freedom [13, 14] or continuous linearly independent functions that spanned the domain [15]. However, a basis consisting of point loads typically has too many unknown variables to be practical, while the success of a basis consisting of functions spanning the domain depends on the shape of the applied loading and the choice of basis functions. More sophisticated candidate sets have been developed that use shape functions from finite element analysis to model the continuous force distribution [19, 20]. Control points are placed across the domain and shape functions are used to interpolate their values at intermediate locations. The control points resemble a point load candidate set, but including shape functions reduces the number of control points needed to approximate an arbitrary distributed load.

Load updating methods have also been studied [21, 22]. In these methods, the load distribution is assumed to take the form of Legendre polynomials across each element of a finite element mesh. An optimization algorithm is then used to minimize the error between the simulated response and the measured response by changing the polynomial coefficients. The load updating method is similar to the influence coefficient method using a pseudo-inverse since both require an assumed form of the forcing, and both seek

a least-squares solution. The order of the assumed polynomial loading can be arbitrarily large, but high-order polynomials introduce more coefficients, which can make the system underdetermined. Hence, the best results are often achieved when a relatively small number of elements and polynomial coefficients are used [22]. The load updating method yields accurate results, but directly optimizing the load parameters is much slower than inverting an influence coefficient matrix, since optimization requires the finite element model to be solved at every iteration.

Machine learning methods for static load prediction have also been developed [23–27]. It is possible to achieve results similar to those from the influence coefficient method by using a feed-forward neural network with a single nonlinear hidden layer and linear output layer [26, 27]. The results show that this neural network approach is much more robust against noise than the influence coefficient method. These results are unsurprising since the influence coefficient method can be thought of as a neural network with a single linear layer where the weight matrix is prescribed rather than learned. In the learned method, the additional hidden layer preprocesses the strain data, and the training process minimizes the network's output error. This method is therefore a generalization of the influence coefficient method. However, the model must be trained with a large amount of force and response data before it can be used for prediction. Additionally, the model contains no underlying physics, so even a well-trained network could predict non-physical results.

Intelligent sensor design can be used to increase the robustness of inverse methods against noise. D-optimal design attempts to minimize the sensitivity of the solution to changes in measurements by changing the sensor configuration [2]. The optimal sensor configuration is determined by generating a set of candidate sensor locations, typically coincident with points on a finite element mesh where sensors could feasibly be placed. A sequential exchange algorithm determines which candidate points to include in the optimal configuration. C-optimal design is similar to D-optimal design, but the objective function is the condition number rather than the sensitivity of the influence matrix [3]. Between these two methods, the C-optimal design produces optimal configurations that produce a lower prediction error than the D-optimal design, suggesting that the condition number of the influence matrix is a better proxy of error than the determinant of the inverse sensitivity [3]. However, C-optimal design is more computationally intensive [3]. A drawback of both techniques is the practical need for discrete optimization algorithms (*e.g.*, sequential exchange, successive reduction). To solve the optimization problem using continuous techniques (e.g., sequential

quadratic programming, particle swarm optimization, etc.), the numerical model of the system would need to be solved at each query point, which may be inefficient and difficult to implement.

The problem of sensor placement may be somewhat alleviated through distributed sensing. If the structural response could be easily queried at any surface point without changing the sensor configuration, it could be possible to tune the measurement points experimentally by querying the system at arbitrary locations and updating the required portions of the numerical model. An early distributed sensor made of constantan wire was proposed by Baz and Poh [28]. The wire changes resistance when subject to axial loads and acts as a distributed strain gauge that can be placed on a structure and probed at any point to obtain a set of discrete measurements. Similar fiber optic sensors have also been developed [29]. A recent study developed a method to determine the strain field on a structural surface using only discrete strain measurements [30]. The method uses a novel interpolation scheme to construct the strain field, effectively changing the question of sensor placement from one of minimizing sensitivity to inversion to one of minimizing interpolation error. However, a designer would still need to carefully choose the locations at which to sample the strain field for force magnitude estimation purposes, since system inversion would still be necessary to estimate the applied load. The present work fills an important literature gap by providing insight into the appropriate placement of sensors for inverse distributed load determination, regardless of whether discrete or distributed sensors are used.

Many techniques exist for solving inverse problems, but only some provide much insight into the underlying mechanics. The present work uses an analytical influence coefficient method to predict loading on a 1D beam and gain insights into the mathematical structure of the influence matrix. Additionally, we use analytical equations to apply a continuous C-optimal design strategy and develop rules of thumb for near-optimal sensor placement. We assume the loading on a 1D beam may be modeled as a piecewise uniformly-distributed load (UDL) or linearly-distributed load (LDL) defined by a set of control points. We limit ourselves to perfectly determined systems, where the number of strain sensors equals the number of control point magnitudes to be estimated, and we assume that the control points are uniformly spaced. Without these limitations, searching for optimal sensor configurations and developing rules of thumb would be infeasible. By focusing on perfectly determined systems, we can isolate the benefits of optimized sensor placement without the confounding effects caused by least-squares solutions. The rules-of-thumb developed in the present work will allow technicians to instrument structures such as press rollers, aircraft wings,

marine propellers, structural support beams, etc. and obtain reasonable load estimates without the need to directly optimize the sensors' locations.

1.2.2 Harmonic Force Estimation

Many engineering structures are subject to harmonic distributed loads during normal operation. For example, the unsteady aerodynamic load on an airfoil [31,32] and the acoustic loading on a rocket thruster [33–35] can be described as spatially distributed harmonic load. Identification of the applied loading in such cases is important for the specification of environments, structural health monitoring, and active control. To facilitate the improved inverse calculation of distributed harmonic loads, Chapter 3 presents a new regularization technique based on generalized Tikhonov regularization that is suitable for under-determined problems. The regularization method is inspired by Bayesian inference and takes advantage of prior knowledge of the force field to obtain accurate force estimates.

Techniques for estimating continuously distributed loads from partial response measurements have been actively investigated for the past few decades [13, 14, 19, 20, 36, 37]. The primary difficulty with this type of problem is that the number of forces that can be estimated without additional assumptions is limited by the number of response measurements. It is therefore necessary to include additional information about the force by either regularizing the problem or describing the distributed force using a finite number of parameters. The force can be described as a set of point loads, but the number of point loads needed to adequately resolve a distributed load frequently makes the number of sensors required infeasible [13, 14]. It is also possible to describe the force as a linear combination of distributed loads that span the domain, but the precision of this method depends on the spatial shape of the truth force and the choice of distributed loads that form the basis [37]. A more general method models the load on small segments of the domain as shape functions [19, 20, 36]. The shape function method enables a smaller number of parameters to accurately resolve a continuously distributed load, but the spatial resolution of the estimate is still limited by the spatial resolution of the shape functions.

Given response measurements, a structural model, and a geometric model of external load, input estimation can be performed by a number of methods. For structures that can be modeled as linear, the FRF matrix describes the relationship between response and load. The FRF matrix can be inverted and multiplied by the measured response to calculate the force [38, 39]. This method is similar to the influence coefficient method

commonly used to estimate static and quasi-static loads, but the FRF matrix is inverted at each frequency of interest [13, 14, 19, 20, 36]. The FRF inversion method is straightforward to implement and computationally efficient, but can suffer from ill-conditioning, especially near resonance frequencies. Direct inversion of the FRF matrix is adequate for estimating the magnitudes of small sets of point loads or distributed loads on beam-like structures, but the number of sensors required to accurately resolve distributed loads on 2D (plate-like) or general 3D structures is frequently infeasible due to the high number of force parameters. The direct inversion method can be improved by using ℓ_q regularization to incorporate information about the expected solution into the least squares problem [40, 41]. Classical regularization introduces a penalty term that favors solutions with certain global characteristics based on the q-norm of the solution, where q is the order of the norm (e.g., 1-norm, 2-norm). Tikhonov (ℓ_2) regularization promotes qualities such as small magnitudes [17, 42] or continuity [43], while ℓ_1 regularization promotes sparsity [44]. The 1- and 2-norms are the most common choices for regularization, but q, the order of the norm, is often tuned to find the optimal norm in machine learning and hierarchical Bayesian methods [45, 46]. However, regardless of the value of q, the additional information provided to the problem by ℓ_q regularization usually only promotes global qualities in the solution and does not incorporate specific prior knowledge.

Force reconstruction methods based on Bayesian inference have become increasingly common in recent years [47–53]. Instead of estimating the load by inverting a deterministic system model, Bayesian methods model the force, noise, and modeling errors using probability distributions and use Bayes' theorem to estimate the probability distribution of the force given the measured data. The resulting distribution can be maximized to produce the force that is most likely to have caused the measured response. Bayesian techniques have been shown to yield excellent input estimates even in the under-determined case [47]. An advantage of Bayesian techniques over deterministic techniques is the inclusion of the prior distribution, which provides the method with additional information about the expected form of the solution. This additional information effectively converts the under-determined problem into an even- or over-determined problem. The prior distribution acts functionally like a regularization term that penalizes estimates that are far from the expected solution, but it differs from classical regularization schemes because it can easily include more specific information beyond global qualities such as smoothness or sparsity [40].

The present work describes an input estimation method based on direct inversion of the FRF matrix augmented with a Bayesian-inspired Tikhonov regularization term that captures prior knowledge of the

spatial distribution of the force. The regularization term emerges naturally from a Bayesian derivation, but the regularization itself takes place in a standard linear regularization framework. Due to the simplicity of the direct inversion technique, we expect our method to be immediately applicable to distributed harmonic load estimation problems from a variety of disciplines including acoustics, fluid dynamics, and aeroelasticity.

1.2.3 Dynamic Force Estimation

Many engineered structures are subject to dynamic loading during normal operation. For monitoring and control applications, it is useful to know these forces in real time. Traveling dynamic loads on structures (*e.g.*, vehicles traveling across a bridge or fluid vortices convecting across an airfoil) are typically difficult to measure directly, so an estimation approach based on system inversion is desirable. In Chapter 4, we demonstrate how the assumed or measured velocity of a traveling force can be incorporated into an augmented Kalman filter (AKF) to produce an improved time-domain force estimate.

Chapter 3 demonstrates how harmonic forces can be estimated in the frequency domain by inverting the FRF matrix. In the case of transient dynamic forcing, where the force cannot be resolved into its frequency components, time-domain techniques are required. It is still possible to frame linear transient problems as matrix inversion problems by concatenating the equations of motion at each time step and solving the force at all time steps simultaneously [54–57]. Framing these problems as matrix inversion problems is attractive because the formulation is simple to implement and the aforementioned matrix regularization techniques are still directly applicable, but the resulting problem is computationally burdensome. As the matrix size scales with the length of the time series, the computational load scales super-linearly. Computational efficiency can be improved somewhat by solving time windows sequentially rather than the entire time series simultaneously, but the length of the window becomes a parameter that affects both the efficiency and accuracy of the estimation [57]. Matrix methods for transient force estimation are also not suitable for real-time applications, since the process operates on full time series rather than single time steps.

Techniques based on Bayesian inference have become increasingly popular for solving inverse problems because of their ability to easily incorporate measured information and prior knowledge into a single estimate. Bayesian techniques directly relate the probability distribution of the force estimate to the probability distributions of the measurements and prior knowledge of the force from existing data. Bayesian techniques for transient load estimation can operate on entire time series [45, 58] or single samples [59, 60], and

have been shown to produce high-quality input estimates in a wide range of applications. Regularization is included in Bayesian inference methods via the prior distribution [61]. The family of classical ℓ_q regularization terms have equivalents using the prior distribution, and the Bayesian regularization term can be simply interpreted in terms of the prior distribution's mean and covariance if the prior distribution is Gaussian. In addition, Bayesian inference is suitable for both linear and non-linear applications, while classical matrix techniques can only be used for linear systems [62]. However, many Bayesian techniques–hierarchical Bayesian methods in particular–do not have a closed-form solution, and the maximum *a posteriori* estimate that represents the most likely force estimate given the posterior distribution must be calculated via computationally intensive techniques such as Markov chain Monte Carlo (MCMC).

The Kalman filter is one of the most widely used techniques based on Bayesian inference. Although the Kalman filter is most commonly used for full state estimation from sparse measurements, variants such as the augmented Kalman filter (AKF) augment unknown parameters such as the force to the state so that simultaneous input-state calculation can be accomplished using the standard Kalman filter equations [63–66]. The Kalman filter is an optimal filter that finds the state estimate that minimizes the estimate uncertainty at each timestep, and has a closed-form solution. It is computationally efficient compared to matrix-based and hierarchical Bayesian methods, and it is suitable for real-time applications. It is also suitable for nonlinear applications through its extended Kalman filter variant [67, 68]. However, the Kalman filter's closed form is derived from Bayes' theorem by assuming the prior and likelihood distributions are Gaussian normal. Because Gaussian normal prior distributions are analogous to ℓ_2 regularization schemes, regularization in the Kalman filter is limited to ℓ_2 regularization with the regularization strength controlled by the model covariance. However, it is possible to incorporate ℓ_1 regularization into the Kalman filter using relevance vector machines [69] or pseudo-measurements [70]. In the latter case, the Kalman filter measurement equations are used to enforce a ℓ_1 regularization constraint without modifying the original Kalman filter equations.

Moving load problems, in which the location and magnitude of one or more moving point forces are estimated from response measurements, have been studied extensively. Moving load estimation techniques are most commonly applied in weigh-in-motion applications where the weight of a moving train or road vehicle is estimated during travel [71–74]. The force estimation technique usually begins by measuring vehicle speed directly using radar or strain pulses [72], and using the estimated velocity as input to the force estimation process. In this way, the number of parameters to estimate is reduced by half, and the known

locations help to more accurately predict the force magnitude. The force magnitude may be estimated in either the time domain directly [75, 76], or estimated first in the frequency domain and transformed into the time domain after solving [77, 78]. In either case, the equations of motion yield a matrix equation that can be inverted using the classical regularization techniques discussed previously [57, 74, 76, 79]. The underlying equations for the traditional methods of solving the moving load identification problem are simple to implement and yield adequate results for weigh-in-motion systems. However, these methods rely on the assumption that the force velocity is known and constant, all loads travel at the same speed, and all loads are point loads. Although force velocity can be measured for other types of traveling forces, such as fluid pressure fields, the assumption that all forces are point loads traveling at the same speed restricts the utility of these methods to weigh-in-motion systems.

In the present work, we replace the Lagrangian framework used by traditional weigh-in-motion techniques (in which each point force is treated as an object with its own position and magnitude) with an Eulerian framework that observes the forces that are present at each degree of freedom (DOF) in the domain at each timestep. Our method consists of a standard AKF that includes a convecting force model that assumes a constant velocity for all forces. However, because the velocity only serves to place the forces near the proper locations, the method is robust to small changes in the velocity of each force. We also apply ℓ_1 regularization through pseudo-measurements using the method of Zhang [70] to reduce the spatial smearing that occurs due to the assumption that forces occur at all points in the domain. We believe that our method will be applicable to a wide range of problems where loads travel with approximately constant velocity across a domain, including weigh-in motion systems and vortex pressure estimation in flowing fluids.

1.2.4 Outline of Present Work

The present work presents techniques for solving force estimation problems in each of the three types of temporal loading: static, harmonic, and general dynamic. First, a method for estimating distributed static loads is presented. The method is based on inverting an influence coefficient matrix that describes the relationship between the applied load and the response to strain. The influence coefficient matrix for classical beams with various boundary conditions is derived analytically, and a sensor placement method based on minimizing the condition number of the influence coefficient matrix is used to encourage solutions that reject noise in the measurements. The methods used here are applied to analytical equations but could

easily be adapted for purely numerical methods. The results show that the reconstruction quality can be greatly improved by using an intelligent sensor design, but the results are insensitive to small changes in the sensor configuration near the optimal configuration. Hence, adequate results will likely be achieved as long as sensors are placed intelligently, even if the configuration is suboptimal.

A similar inversion method for harmonic distributed load estimation is presented in the following chapter, but the frequency response matrix is inverted at each frequency of interest rather than inverting an influence coefficient matrix once. However, the chapter on harmonic load estimation also includes a novel technique for including prior knowledge about the spatial form of the force distribution at each frequency. The technique is inspired by the prior distribution term from Bayesian inference techniques but is implemented using a standard Tikhonov regularization scheme. The results show that regularizing the system inversion using a spatial prior enables a large number of force parameters to be estimated from a relatively small number of measurements. Regularization converts the ill-posed input estimation problem into a well-posed analogue. The regularization techniques applied to distributed harmonic loading can also be applied directly to the distributed static loading problem from the previous chapter.

Finally, a method for estimating the location and magnitude of traveling loads in the time domain is presented. The method is based on the AKF, which enables online force estimation but disables the regularization technique used for harmonic force estimation. Instead, a convecting force model is used instead of the standard zero-order hold force model traditionally used in the AKF. The force model embedded in the AKF is functionally equivalent to a regularization term and allows the user to specify the speed at which the force moves across the domain. A pseudo-measurement technique is also used to encourage sparse force estimates, which makes the method suitable for estimation of concentrated forces. The results show that the convecting force model yields much better results than the standard zero-order hold AKF. The results presented here are mostly focused on the estimation of concentrated moving loads, but results suggest that the method is also suitable for distributed moving load estimation if the pseudo-measurement technique is not used.

The primary contributions of this work are as follows:

1. A novel sensor system design technique for static distributed load estimation is developed.

2. Linear influence coefficient equations that relate the static distributed load on a structure to its stress response are derived analytically.

3. A novel framework inspired by Bayesian inference for incorporating prior spatial information about static and harmonic distributed loads via standard Tikhonov regularization is introduced.

4. Experimental validation of the novel scheme for incorporating spatial priors using acceleration response measurements from a structural experimental model subject to a harmonic acoustic pressure field.

5. A convecting force model is appended to an augmented Kalman filter (AKF) technique to enable traveling force estimation using the standard Kalman filter.

6. The AKF with traveling force model is enhanced with a pseudo-measurement which, in conjunction with the convecting force model, enables the estimation of both concentrated and distributed traveling loads.

Chapter 2

Static Distributed Force Estimation

This chapter presents a method for estimating static distributed forces on beam-like structures from strain measurements by inverting an influence coefficient matrix. In an effort to provide designers with guidance, we also identify optimal sensor configurations for predicting static distributed loads on beams with classical boundary conditions. The loading distribution on the structure is assumed to be either a piece-wise linearly-distributed load (LDL) or a uniformly-distributed load (UDL), allowing for continuously-distributed loads to be estimated using the magnitudes of a small number of control points. Given the simplicity of the beam structure, the equations of the influence coefficient method are derived analytically, which allows for the sensor placement to be specified using continuous optimization methods. "Rules of thumb" for sensor placement are presented based on the optimization results. Results show that the optimal and rule-of-thumb sensor configurations are more resistant to input noise than naïve configurations, with the rule-of-thumb configurations yielding similar force predictions relative to the optimal configurations. We expect the rules of thumb to be useful guidelines for engineers designing tests on beam-like structures such as aircraft wings or marine propellers where the inverse calculation of distributed loads is of interest. The results in this chapter are published in Ref. [36].

2.1 Methods

2.1.1 Load-Strain Relationships

For an Euler-Bernoulli beam of uniform cross-section and uniform Young's modulus E, the transverse deflection w is related to the applied transverse loading q by

$$EI\frac{d^4w}{dx^4} = q(x), \tag{2.1}$$

where I is the area moment of inertia of the beam's cross section and x is the distance along the beam. Under the same assumptions, the relationship between loading and internal moment M is

$$\frac{d^2M}{dx^2} = q(x). \tag{2.2}$$

Eqs. (2.1) and (2.2) provide a relationship between the applied loading and the structural response. Because strain sensors are commonly used in static structural measurement, we now derive a relationship between strain and internal moment. The normal stress due to bending at the outermost fiber of the beam is given by the well-known relationship

$$\sigma(x) = \frac{M(x)h}{2I}, \tag{2.3}$$

where h is the beam's thickness, and σ is the maximum normal stress in the cross section. Moment may be related directly to strain via Hooke's law

$$\frac{M(x)h}{2I} = E\varepsilon(x), \tag{2.4}$$

where ε is the strain of the outermost material fiber. Notice that if the applied loading q can be separated into a product of integrable spatially-varying terms and constant magnitudes, Eq. (2.2) may be twice integrated and combined with Eq. (2.4) to obtain a linear relationship between strain and applied load.

2.1.2 Distributed Loading Configurations

The relationship between loading and strain given by Eqs. (2.2) and (2.4) is valid for arbitrary static loading on a uniform beam. We assume this loading may be approximated by either a piecewise UDL or piecewise LDL function spanning the beam. Both of these approximating functions are defined by a finite number of control points representing the value of the function at the control point positions. A schematic

of a beam with applied UDL and LDL loading is shown in Fig. 2.1. In the case of a piecewise UDL or LDL, Eqs. (2.2) and (2.4) may be rewritten as a linear system of equations. The loading distribution for a piecewise UDL with k control points is defined as

$$q(x) = p_i, \quad a_{i-1} < x < a_i, \tag{2.5}$$

where p represents the control point values, and a is the control point locations. By convention, $a_0 = 0$, and the k control points are located at the right side of each segment as shown in Fig. 2.1a. The control points for both UDL and LDL configurations divide the beam into segments. Segments are numbered consecutively from left to right.

Figure 2.1. (a) UDL and (b) LDL loading configurations with five control points each.

It can be shown via double integration of Eq. (2.2) that the general equation for the moment in segment i due to the loading in Eq. (2.5) is

$$\begin{aligned} M_i(x) = p_i \left(a_i x - \frac{x^2 + a_i^2}{2} \right) + \sum_{j=i+1}^{l-1} p_j \left(a_j x - \frac{a_j^2}{2} - a_{j-1} x + \frac{a_{j-1}^2}{2} \right) \\ + p_l \left(\frac{a_{l-1}^2}{2} - a_{l-1} x \right) + C_V x + C_M, \qquad i < l, \\ M_i(x) = -\frac{p_i x^2}{2} + C_V x + C_M, \qquad i = l, \end{aligned} \tag{2.6}$$

where l is the number of loading segments, and C_V and C_M are constants of integration, which are determined by the boundary conditions. For a general UDL, $l = k$. Eq. (2.6) is applicable for $l > 1$. The corresponding moment equation for $l = 1$ is given in B. The values of C_V and C_M for the four classical beam boundary conditions (clamped-free (CF), simply supported-simply supported (SS), clamped-clamped (CC), and clamped-simply supported (CS)) are shown in A.

The loading distribution for an LDL with k control points is defined as

$$q(x) = \left(\frac{p_{i+1} - p_i}{a_{i+1} - a_i}\right)(x - a_i) + p_i, \quad a_i < x < a_{i+1}. \tag{2.7}$$

The first control point for a piecewise LDL is placed at the beam's root, and subsequent points are placed at the right side of each segment as shown in Fig. 2.1b. Note that the loading configuration described in Eq. (2.7) linearly interpolates between the control point values. The general equation for the moment in segment i may be written for a beam subject to a piecewise LDL

$$\begin{aligned}
M_i(x) &= p_i(\mu_f(i,x)) + p_{i+1}(\mu_c(i+1,x) - \mu_f(i,x)) + p_l(\mu_l(l,x) - \mu_c(l-1,x)) - p_{l+1}\left(\mu_l(l,x) + \frac{x^2}{2}\right) \\
&\quad + \sum_{j=i+2}^{l-1} p_j(\mu_c(j,x) - \mu_c(j-1,x)) + C_V x + C_M, && i < l-1, \\
M_i(x) &= p_i(\mu_f(i,x)) + p_{i+1}(\mu_l(i+1,x) - \mu_f(i,x)) - p_{l+1}\left(\mu_l(l,x) + \frac{x^2}{2}\right) \\
&\quad + C_V x + C_M, && i = l-1, \\
M_i(x) &= p_l\left(\left(\frac{-1}{a_{l+1} - a_l}\right)\left(\frac{-x^3}{6} + a_l\frac{x^2}{2}\right) - \frac{x^2}{2}\right) \\
&\quad + p_{l+1}\left(\left(\frac{1}{a_{l+1} - a_l}\right)\left(\frac{-x^3}{6} + a_l\frac{x^2}{2}\right)\right) + C_V x + C_M, && i = l,
\end{aligned} \tag{2.8}$$

where $l = k-1$ and $\mu_f(s,x)$, $\mu_c(s,x)$, and $\mu_l(s,x)$ correspond to the influence of the first, intermediate, and last load segments, respectively, and are functions of segment number, s, and the spatial variable, x. Eq. (2.8) is applicable for $l > 2$. The corresponding moment equation for $l \leq 2$ is given in B. The expressions for $\mu_f(s,x)$, $\mu_c(s,x)$, and $\mu_l(s,x)$ are

$$\begin{aligned}
\mu_f(s,x) &= \left(\frac{-1}{a_{s+1} - a_s}\right)\left(\frac{-x^3}{6} + a_s\frac{x^2}{2} + a_{s+1}^2\left(\frac{x(a_{s+1} - 2a_s)}{2a_{s+1}} + \frac{a_s}{2} - \frac{a_{s+1}}{3}\right)\right) \\
&\quad - \frac{x^2}{2} + a_{s+1}x - \frac{a_{s+1}^2}{2} && (2.9) \\
\mu_c(s,x) &= \left(\frac{-1}{a_{s+1} - a_s}\right)\left(x\left(\frac{a_{s+1}}{\sqrt{2}} - \frac{a_s}{\sqrt{2}}\right)^2 - \frac{a_s^3}{6} + a_s\frac{a_{s+1}^2}{2} - \frac{a_{s+1}^3}{3}\right) \\
&\quad - \frac{x^2}{2} + a_{s+1}x - \frac{a_{s+1}^2}{2} && (2.10) \\
\mu_l(s,x) &= \left(\frac{-1}{a_{s+1} - a_s}\right)\left(\frac{a_s^2}{2}x - \frac{a_s^3}{6}\right) - \frac{x^2}{2} && (2.11)
\end{aligned}$$

The values of C_V and C_M for the four classical beam boundary conditions are given in A.

Note that the moment equations for both UDL and LDL are linear in $\boldsymbol{p}$, which is the vector of control point values. Hence, Eqs. (2.6) and (2.8) may be rewritten in matrix form

$$\boldsymbol{M} = [A]\boldsymbol{p}, \tag{2.12}$$

where $[A]$ is the influence matrix relating the applied load to internal moment, and $\boldsymbol{M}$ is a discrete vector of internal moments at any number of evaluation points. Combining Eqs. (2.4) and (2.12) yields a relationship between applied loading and strain

$$[A]\boldsymbol{p} = \frac{2EI}{h}\boldsymbol{\varepsilon}. \tag{2.13}$$

Given discrete strain measurements, the influence matrix $[A]$ may be inverted to calculate a UDL or LDL approximation of an arbitrary distributed loading.

2.1.3 Condition Number and Error

The solution of Eq. (2.13) by inversion tends to amplify errors in the strain data. The condition number for inversion, κ, quantifies the sensitivity of the solution $\boldsymbol{p}$ to changes in the input, $\boldsymbol{\varepsilon}$. The condition number for inversion of an arbitrary square influence matrix $[A]$ of size k is defined as

$$\kappa = \frac{\lambda_{\text{max}}}{\lambda_{\text{min}}} = \|[A]\|\|[A]^{-1}\|, \tag{2.14}$$

where λ_{max} and λ_{min} are the largest and smallest singular values of $[A]$, respectively, and $\|*\|$ denotes the matrix 2-norm [1]. Analogous definitions of the condition number for non-square matrices also exist, but these are not needed for the perfectly determined systems studied here. Because the condition number represents the sensitivity of the system matrix inversion to measurement noise, the condition number will be used as a proxy for error in the inverse-calculated loads.

Figs. 2.2 and 2.3 show condition number and error plots on a beam using two sensors across the domain of possible sensor placements. Here, x_i is the location of sensor i along the beam, L is the length of the beam, and $\bar{x}_i = x_i/L$. For the error calculations in Fig. 2.3, a known UDL or LDL configuration with $\boldsymbol{p} = [17.1, 8.3]^T$ is applied to a wide-flange I beam (metric designation W 200 $\times$ 165 $\times$ 41.7) with $E = 200$ GPa, $I = 4.09 \times 10^{-5}$ m^4, $L = 3.5$ m and $h = 0.205$ m. In the UDL case, $\boldsymbol{a} = [6.15, 12.3]^T$, and in the LDL case, $\boldsymbol{a} = [0, 12.3]^T$. The strain is calculated using Eq. (2.13). A perturbation of 0.01% of the measured strain (-0.01% for the first strain, 0.01% for the second) is added to the strain values. A different

perturbation percentage must be used for each sensor to calculate a meaningful error map since applying the same percent perturbation to each sensor results in output error equal to the applied perturbation percentage. Eq. (2.13) is then used to calculate the load configuration from the corrupted strain data. Fig. 2.3 presents the relative error between the first element of the true loading p_1 and the first element of the predicted loading. From the two figures, it is clear that sensor configurations with large associated errors also have influence matrices with large condition numbers. However, sensor configurations with large condition numbers do not necessarily yield large errors. These low-dimensional results show that minimizing condition number should also yield near-minimum error.

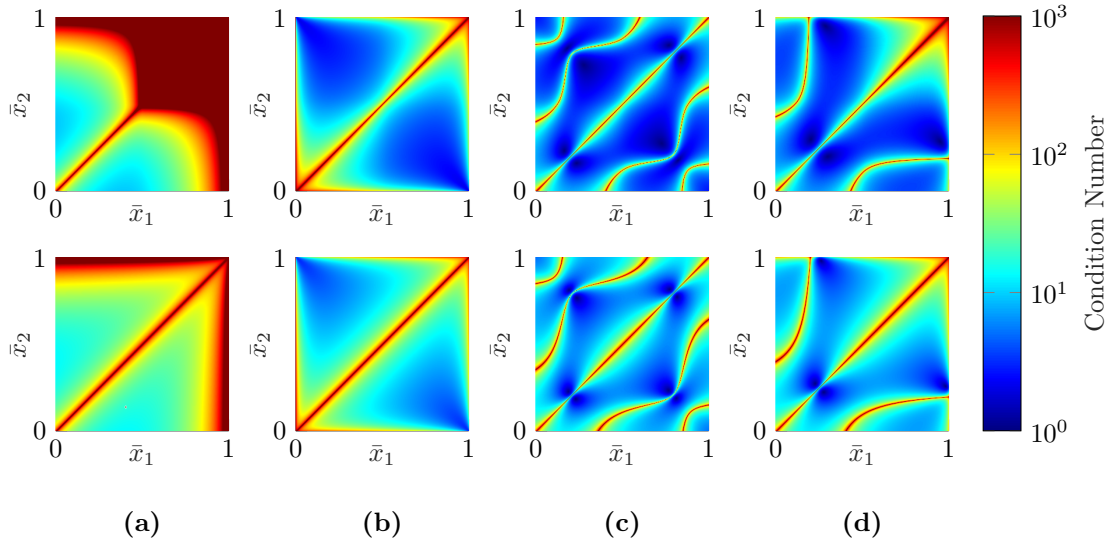

Figure 2.2. Condition number of the 2×2 influence matrix at all combinations of measurement locations x_1 and x_2 for UDL (top) and LDL (bottom) assumed loading configurations and (a) CF, (b) SS, (c) CC, and (d) CS boundary conditions.

In the present work, the optimal sensor configuration for a given number of sensors is found by minimizing the condition number of the influence matrix. Formally,

$$\boldsymbol{\xi} = \arg\min_{\boldsymbol{\xi}} \quad \kappa \qquad s.t. \quad 0 \leq x_i \leq L \quad \text{for} \quad 1 \leq i \leq m \tag{2.15}$$

where $\boldsymbol{\xi}$ is a sensor configuration vector containing the locations x_i of m sensors along the beam. Note that κ exhibits symmetry since, for example, a sensor configuration $\boldsymbol{\xi} = [x_1, x_2]^T$ is equivalent to configuration $\boldsymbol{\xi} = [x_2, x_1]^T$. In principle, this symmetry could be exploited to introduce m more constraints to the optimization problem of the form $x_i < x_{i+1}$. However, given our study's relatively small parameter spaces,

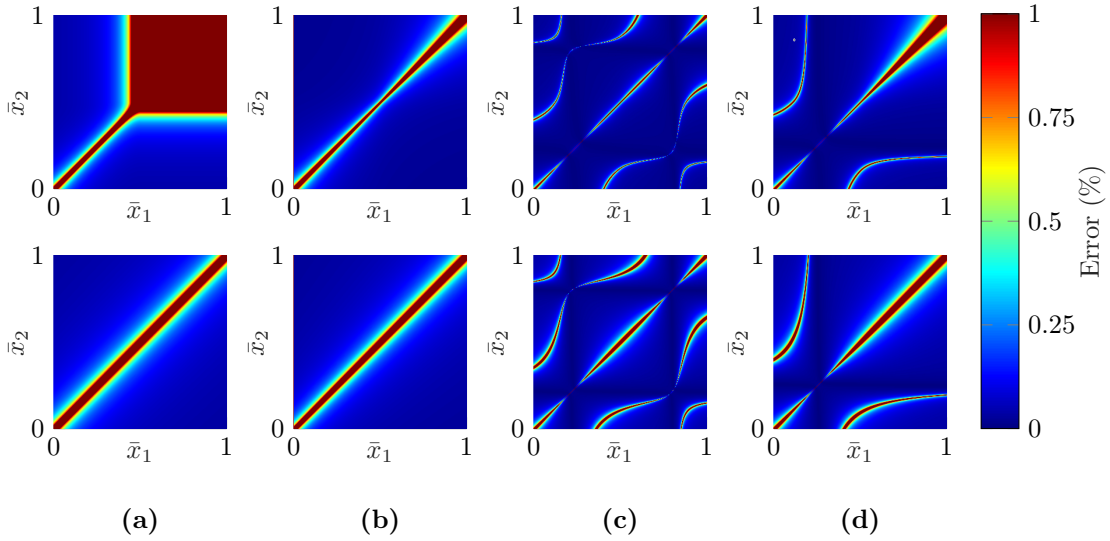

Figure 2.3. Relative error between the first magnitude of a known loading configuration and a prediction of the same loading configuration using synthesized strain data with a 0.01% perturbation and a 2×2 influence matrix at all combinations of measurement locations x_1 and x_2 for UDL (top) and LDL (bottom) assumed loading configurations and (a) CF, (b) SS, (c) CC, and (d) CS boundary conditions.

the unconstrained problem may be solved efficiently without constraining the domain. As seen in Fig. 2.2c and 2.2d, the κ parameter space typically has many local minima, even with only two sensors. Further, the number of local minima is expected to increase considerably as the number of sensors increases. Classical gradient-based algorithms (e.g., sequential quadratic programming, interior-point method) often fail to find the global minimum when many local minima are present [80]. To circumvent this issue, a particle swarm optimization (PSO) algorithm is used here to search the parameter space more thoroughly, making the discovery of the global optimum far more likely. PSO is a stochastic optimization method that has been widely applied to optimization problems across several disciplines [81]. The algorithm is initialized by randomly scattering "particles" across the parameter space. Each particle knows the value of the optimization hypersurface at its current location, the position at which it found its personal best solution, and the best solution found by a set of its nearest neighboring particles. The particles update their positions at each iteration based on these three pieces of information. This way, the particles can search for minima across a wide parameter space. For each sensor configuration, a swarm size of $20m$ is selected. Since the particle swarm algorithm is not guaranteed to find a global minimum, the algorithm is executed four times during optimization, and the

configuration that yields the lowest κ is taken as the optimal configuration. It should be noted that, while the PSO is not guaranteed to find the global minimum in a single execution, it is much more likely to find the global minimum than a single execution of a gradient-based method on a domain containing several local minima. A gradient-based method could be applied repeatedly with different initial points to find the global minimum, but the chances of finding the global minimum would be no better than using the PSO.

For each loading type (UDL or LDL) and boundary condition (CF, SS, CC, or CS), a "rule-of-thumb" is also developed by inspection of the optimal sensor configurations. These rules-of-thumb are equations that seek to generalize the optimal configurations for an arbitrary number of sensors. In practice, we expect the rules-of-thumb to be a set of guidelines that approximate the optimal configurations, and allow practitioners to intelligently design sensor systems on beam-like structures in the absence of a detailed numerical model. The success of each rule-of-thumb is checked by defining a condition number ratio K as the ratio of the condition number of the influence matrix associated with the locally optimal sensor configuration nearest the rule-of-thumb configuration, κ_o (calculated using a sequential quadratic programming optimization algorithm with the rule-of-thumb configuration as the initial condition) to the condition number of the influence matrix associated with the rule-of-thumb, κ_r

$$K = \kappa_o / \kappa_r. \tag{2.16}$$

A value of K near one indicates the rule of thumb should yield similar error to the true optimal configuration.

In the present work, we limit ourselves to perfectly determined systems ($k = m$), loading configurations with uniformly-spaced control points, and the classical boundary conditions described above (CF, SS, CC, CS). While rules of thumb could in principle be developed for arbitrary combinations of k and m and loading with control points at arbitrary locations, we do not investigate these cases due to the increase in the size of the parameter space and the enormous effort required to develop rules-of-thumb. We do not consider other boundary condition configurations partly due to the larger associated parameter space, but mostly because every new configuration requires a new set of analytical equations for the influence coefficient matrix. These configurations could be studied efficiently using numerical techniques, but the optimization strategies presented here require analytical expressions.

As a note on sensor configuration design, κ for an arbitrary matrix tends to increase with the size of the matrix. This is implied by Eq. (2.14) since the ratio of the largest singular value of a matrix to its smallest

will tend to increase as more singular values (corresponding to a higher-rank matrix) are introduced. Hence, for perfectly determined cases where $k = m$, results that are more resistant to sensor noise may be achieved by reducing m. Alternatively, a rank-reduction technique could be used to reduce error for cases where a large k is required [19]. For the more general case where $k \leq m$, better resistance to noise may be achieved by increasing m while keeping k as low as possible. The resulting over-determined system may be solved via a Moore-Penrose pseudo inverse to obtain a least-squares solution. In the present work, we only investigate determined systems, and we do not use rank-reduction. By formally investigating strain sensor placement without using any techniques to improve the results further, we can understand the extent to which the accuracy of inverse-calculated loads may be improved by intelligent sensor placement alone.

2.2 Results

2.2.1 Optimization Results

Figs. 2.4-2.11 show the optimal sensor configurations for every combination of load distribution type (UDL, LDL) and boundary condition (CF, SS, CC, CS), with $2 \leq m \leq 8$. Also shown are the corresponding rule-of-thumb sensor configurations described in Tables 2.1 and 2.2 for $2 \leq m \leq 8$.

The optimal sensor configurations for CF beams are similar for UDL and LDL loading. In both cases, a sensor is placed at the beam's root, another is placed near the middle of the first segment, and subsequent sensors are placed in each of the following loading segments. For UDL loading, no sensors are placed in the final segment, and intermediate sensors are placed between 55% and 75% of their corresponding segment's span. The lack of a sensor in the tip segment is unsurprising since Eqs. (2.6) and (A.3) show that only the load magnitude of the final segment affects the strain in the final segment. Therefore, more information is gained by placing sensors nearer the root. If placing a sensor near the root provides that sensor with the most possible information about all the forces, it may be natural to wonder why all sensors are not placed in the first segment. Suppose all sensors are placed near each other. In that case, the strain response for all sensors will be very similar, and the row vectors of the influence matrix will point in approximately the same direction, implying linear dependence, a nearly singular matrix, and a large condition number. Hence, optimal sensor placements will typically separate the sensors while simultaneously providing as much unique information as possible.

For a CF beam under LDL loading, a sensor is placed in the final segment, but intermediate sensors are placed at 20% of their segment's span. Eqs. (2.8) and (A.7) show that only the two load magnitudes associated with the last LDL segment influence the strain in the last segment. Furthermore, when a sensor is placed near the root of segment i, the measured strain depends more on p_{i+1} than p_i. Hence, the optimal configurations shown in Fig. 2.8 allow each sensor to be more sensitive to the control point magnitude at the tip of its segment. When the sensors are ordered from root to tip, the influence matrix has a nearly upper-triangular structure for both UDL and LDL loading with CF boundary conditions, except that an additional non-zero diagonal exists below the main diagonal. The rules of thumb developed for the CF boundary condition cases are visually similar to the true optimal configurations.

The optimal configurations for both UDL and LDL loading with SS boundary conditions—Figs. 2.5 and 2.9—are symmetric about the center of the beam. For UDL loading, the sensors are placed near the midpoint of each segment. Sensor placement for LDL loading is slightly more complicated, but sensors tend to be placed near their corresponding control points, with sensors near the beam's midpoint placed closer to their control points than sensors near the root or the tip. Due to this symmetry, when the sensors are ordered from root to tip, the influence matrices for UDL and LDL loading take on a form where

$$A_{i,j} = A_{m+1-i,m+1-j}, \tag{2.17}$$

i.e., column (or row) j of A is the reverse of column (or row) $m + 1 - j$. The rules of thumb developed for the SS boundary condition cases are visually similar to the true optimal configurations.

Given the symmetry of the SS boundary condition cases, the asymmetry in the optimal configurations for CC boundary conditions is unexpected. Symmetric optimal configurations exist for some m (see, e.g., Fig. 2.6, m = 2, 4, 5, and 8; Fig. 2.10, m = 4, 5, 7), but the cases for which symmetric configurations exist do not seem to follow any particular pattern. We could not develop robust rules of thumb that hold for large m with CC boundary conditions. However, the presented rules of thumb hold reasonably well for small numbers of sensors ($m < 10$). The rules of thumb are developed by assuming symmetry in all cases. This assumption is justified by recognizing that even in cases where symmetry is not present, the asymmetry is due mainly to the movement of a small subset of the sensors. No special form of the influence matrix exists for optimal sensor configurations with CC boundary conditions.

The optimal configurations for CS boundary conditions do not follow an intuitive pattern. For UDL loading, the optimal configurations tend to resemble somewhat either an optimal CF (one sensor at the clamped end, other sensors distributed among the remaining segments, as seen in the m=8 case) or SS configuration (sensors placed near the midpoint of each segment, as seen in the m=6 case). However, over several runs of the particle swarm optimization algorithm for a given m, two local optima resembling an optimal SS configuration and an optimal CF configuration emerge. The corresponding condition numbers of these configurations are consistently within approximately 10% of each other, and the configuration with the smaller condition number varies depending on m. Hence, there are two configurations for a given number of sensors that should yield similar results. We suspect the existence of multiple similar optima can be explained by the similarity of CS boundary conditions to both CF and SS boundary conditions. To develop the rule of thumb, we arbitrarily decide that the configuration resembling the optimal CF configuration should be the target. Consequently, the rule of thumb does not resemble the globally optimal solution for some configurations.

A more apparent trend emerges for the CS boundary condition with LDL loading. For $m \geq 6$, sensors form two groups near the root and the tip, with at least one segment gap between them. The sensor group near the clamped side somewhat resembles the optimal configurations for CF boundary conditions, where two sensors are placed at and near the root, and the remaining sensors are placed uniformly across the span. The group near the simply-supported end resembles the optimal configurations for SS boundary conditions, where the sensors are placed uniformly along the beam with an offset on either end. Upon adding a sensor, the optimal configurations show the existing sensors compressing toward the root and tip, and the additional sensor added to one of the groups. Occasionally, one of the existing sensors will switch from one group to the other. This trend persists for $m > 8$. The order in which sensors are added to each group and the configurations where sensors move from one side to the other are unclear, so we assume new sensors are added to each group alternately. No special form of the influence matrix exists for optimal sensor configurations with CS boundary conditions for either UDL or LDL loading.

Table 2.1. Rules of thumb for sensor placement for an assumed UDL loading with constant spacing in $\boldsymbol{a}$ and $k = m$. In the context of this table, i is the subscript of the corresponding sensor placement x_i, and "to" means "up to and including".

BC	m	Eq (%)	Segment #	Notes
CF	Any	$\begin{bmatrix} x_1 \\ x_2 \\ x_3 \text{ to } x_{m-1} \\ x_m \end{bmatrix} = \begin{bmatrix} 0 \\ 60 \\ 55 + (i-3)\frac{62.5-55}{m-4} \\ 74.5 \end{bmatrix}$	$\begin{bmatrix} 1 \\ 1 \\ i-1 \\ m-1 \end{bmatrix}$	Linear from 55% to 62.5% between x_3 and x_{m-1}
SS	Any	$\begin{bmatrix} x_1 \text{ to } x_m \end{bmatrix} = \begin{bmatrix} 50 - \frac{100}{4m}\sin(2\pi\frac{i}{m+1}) \end{bmatrix}$	$\begin{bmatrix} 1 \text{ to } m \end{bmatrix}$	
CC	2	$\boldsymbol{\xi} = \begin{bmatrix} 56 & 44 \end{bmatrix}^T$	$\begin{bmatrix} 1 & 2 \end{bmatrix}^T$	
	3	$\boldsymbol{\xi} = \begin{bmatrix} 70 & 20 & 50 \end{bmatrix}^T$	$\begin{bmatrix} 1 & 3 & 3 \end{bmatrix}^T$	
	>3	$\begin{bmatrix} x_1 \text{ to } x_m \end{bmatrix} = \begin{bmatrix} 50 + 45\sin(4\pi\frac{i}{m+1}) \end{bmatrix}$	$\begin{bmatrix} 1 \text{ to } m \end{bmatrix}$	
CS	2	$\boldsymbol{\xi} = \begin{bmatrix} 40 & 60 \end{bmatrix}^T$	$\begin{bmatrix} 1 & 1 \end{bmatrix}^T$	
	3	$\boldsymbol{\xi} = \begin{bmatrix} 71 & 92 & 86 \end{bmatrix}^T$	$\begin{bmatrix} 1 & 1 & 3 \end{bmatrix}^T$	
	4	$\boldsymbol{\xi} = \begin{bmatrix} 58 & 84 & 62 & 70 \end{bmatrix}^T$	$\begin{bmatrix} 1 & 1 & 3 & 4 \end{bmatrix}^T$	
	> 4	$\begin{bmatrix} x_1 \\ x_2 \\ x_3 \\ x_4 \text{ to } x_m \end{bmatrix} = \begin{bmatrix} 0 \\ 25 \\ 90 \\ 80 + (i-3)\frac{65-80}{m-4} \end{bmatrix}$	$\begin{bmatrix} 1 \\ 2 \\ 2 \\ 4 \text{ to } m \end{bmatrix}$	Linear from 80% to 65% between x_4 and x_m

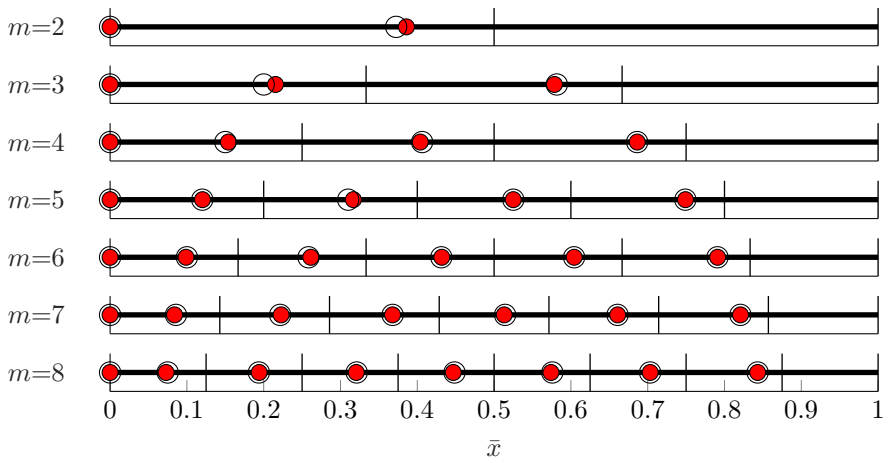

Figure 2.4. Optimal (red dots) and rule-of-thumb (black circles) sensor configurations for a UDL loading configuration and CF boundary conditions at various m. The vertical lines indicate the loading segments.

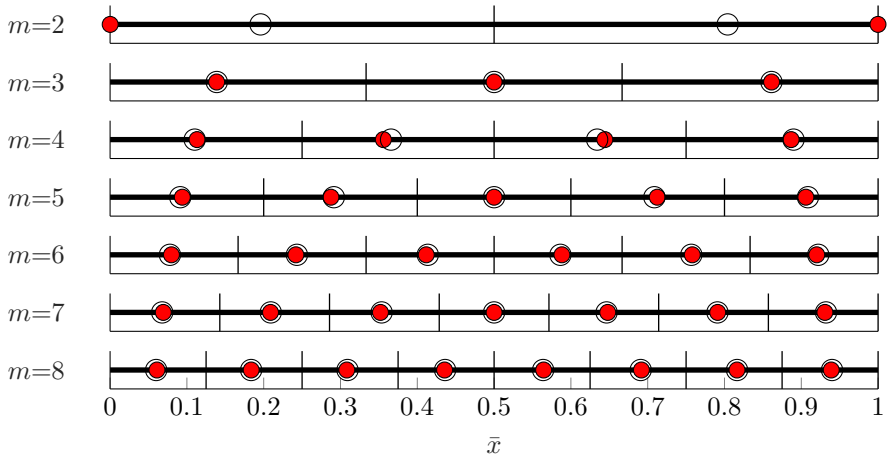

Figure 2.5. Optimal (red dots) and rule-of-thumb (black circles) sensor configurations for a UDL loading configuration and SS boundary conditions at various m. The vertical lines indicate the loading segments.

Fig. 2.12 shows the evolution of K with increasing numbers of sensors for every combination of load distribution function type and boundary condition. Also shown is the evolution of the ratio between κ_o and the condition number of the influence matrix associated with a naïve configuration $\boldsymbol{\xi}_n$, κ_n. Two naïve configurations are constructed, each meant to represent a configuration developed based on the intuition of an intelligent designer. The "cantilevered-like" naïve configuration is constructed by dividing the beam into m equal segments and placing a sensor at the root of each segment. The cantilevered-like configuration is shown in the bottom plot of Fig. 2.14. The "clamped-like" naïve configuration is constructed by first placing one sensor near either end of the beam (0.01% and 99.99% of span). The beam is then divided into $m - 2$

Table 2.2. Rules of thumb for sensor placement for an assumed LDL loading with constant spacing in $\boldsymbol{a}$ and $k = m$. In the context of this table, i is the subscript of the corresponding sensor placement x_i, and "to" means "up to and including". For the SS and CC cases, the sensor configurations are symmetric about $L/2$, and only half the sensors from 0 to $L/2$ (inclusive) are reported.

BC	m	Eq (%)	Segment #
CF	Any	$\begin{bmatrix} x_1 \\ x_2 \\ x_3 \text{ to } x_m \end{bmatrix} = \begin{bmatrix} 0 \\ 40 \\ 20 \end{bmatrix}$	$\begin{bmatrix} 1 \\ 1 \\ i-1 \text{ to } m-1 \end{bmatrix}$
SS	2	$\boldsymbol{\xi} = \begin{bmatrix} 0.1 & 99.9 \end{bmatrix}^T$	$\begin{bmatrix} 1 & 1 \end{bmatrix}^T$
	3	$\boldsymbol{\xi} = \begin{bmatrix} 23 & 0 & 77 \end{bmatrix}^T$	$\begin{bmatrix} 1 & 2 & 2 \end{bmatrix}^T$
	>3	$\begin{bmatrix} x_1 \text{ to } x_{\lfloor \frac{m-1}{2} \rfloor} \end{bmatrix} = \begin{bmatrix} 30 + (i-1)\frac{2-30}{\lfloor (m-1)/2 \rfloor - 1} \end{bmatrix}$ $x_{m/2} = 90$, even m $x_{\lfloor m/2 \rfloor + 1} = 0$, odd m	$1 \text{ to } \lfloor \frac{m-1}{2} \rfloor$ $\frac{m}{2} - 1$, even m $\lfloor \frac{m}{2} + 1 \rfloor$, odd m
CC	2	$\boldsymbol{\xi} = \begin{bmatrix} 24 & 76 \end{bmatrix}^T$	$\begin{bmatrix} 1 & 1 \end{bmatrix}^T$
	3	$\boldsymbol{\xi} = \begin{bmatrix} 44 & 51 & 62 \end{bmatrix}^T$	$\begin{bmatrix} 1 & 2 & 2 \end{bmatrix}^T$
	4	$\boldsymbol{\xi} = \begin{bmatrix} 55 & 75 & 25 & 46 \end{bmatrix}^T$	$\begin{bmatrix} 1 & 1 & 3 & 3 \end{bmatrix}^T$
	5	$\boldsymbol{\xi} = \begin{bmatrix} 62 & 98 & 0 & 2 & 38 \end{bmatrix}^T$	$\begin{bmatrix} 1 & 1 & 3 & 4 & 4 \end{bmatrix}^T$
	>5	$\begin{bmatrix} x_1 \\ x_2 \\ x_3 \text{ to } x_{\lfloor \frac{m-1}{2} \rfloor} \end{bmatrix} = \begin{bmatrix} 0 \\ 40 \\ 15 \end{bmatrix}$ $x_{m/2} = 15$, even m $x_{(m-1)/2+1} = 0$, odd m	$\begin{bmatrix} 1 \\ 1 \\ i-1 \end{bmatrix}$ $m/2$, even m $(m-1)/2 + 1$, odd m
CS	2	$\boldsymbol{\xi} = \begin{bmatrix} 26 & 97 \end{bmatrix}^T$	$\begin{bmatrix} 1 & 1 \end{bmatrix}^T$
	3	$\boldsymbol{\xi} = \begin{bmatrix} 48 & 56 & 94 \end{bmatrix}^T$	$\begin{bmatrix} 1 & 1 & 2 \end{bmatrix}^T$
	4	$\boldsymbol{\xi} = \begin{bmatrix} 48 & 57 & 1 & 82 \end{bmatrix}^T$	$\begin{bmatrix} 1 & 1 & 3 & 3 \end{bmatrix}^T$
	5	$\boldsymbol{\xi} = \begin{bmatrix} 0 & 13 & 39 & 95 & 75 \end{bmatrix}^T$	$\begin{bmatrix} 1 & 2 & 2 & 3 & 4 \end{bmatrix}^T$
	>5	$\begin{bmatrix} x_1 \\ x_2 \text{ to } x_{\lfloor m/2 \rfloor} \\ x_{\lceil m/2 \rceil} \\ x_{\lceil m/2 \rceil + 1} \text{ to } x_{m-2} \\ x_{m-1} \\ x_m \end{bmatrix} = \begin{bmatrix} 0 \\ 40 + (i-2)\frac{10-40}{\lfloor m/2 \rfloor - 2} \\ 95 \\ 40 + (i - (\lceil m/2 \rceil + 1))\frac{10-40}{m - \lceil m/2 \rceil - 2} \\ 90 \\ 70 \end{bmatrix}$	$\begin{bmatrix} 1 \\ i-1 \\ \lceil m/2 \rceil - 2 \\ i \\ m-2 \\ m-1 \end{bmatrix}$

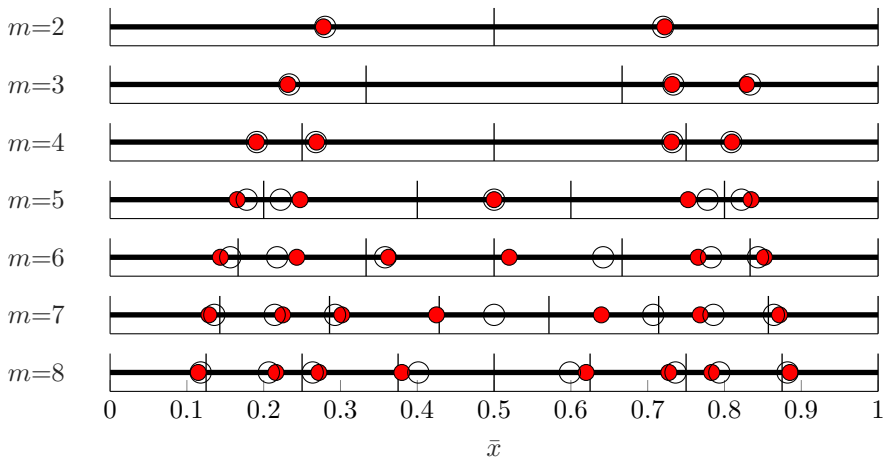

Figure 2.6. Optimal (red dots) and rule-of-thumb (black circles) sensor configurations for a UDL loading configuration and CC boundary conditions at various m. The vertical lines indicate the loading segments.

patches, and the remaining sensors are placed at the center of each patch. The clamped-like configuration is shown in the bottom plot of Fig. 2.17. The cantilevered-like naïve configuration is used for the CF and CS boundary conditions, while the clamped-like naïve configuration is used for the SS and CC boundary conditions.

In the cantilevered configurations, K is close to one for all m, suggesting that the rule of thumb is very close to the true optimal configuration. Similarly, K for the simply supported configurations is above 0.9 for most m. For the clamped-clamped and clamped-simple configurations, the condition ratio begins decreasing for configurations with greater than approximately ten sensors, suggesting the rules of thumb do not approximate the true optimal configurations very well at high m. However, $K > 0.7$ for all $m < 10$, indicating a reasonably good match for small sensor configurations. Note for the UDL CS configuration that, since there typically exist two local minima with similar condition numbers and the rule-of-thumb configuration does not resemble the global minimizer for some m, κ_o is calculated using a particle swarm algorithm to ensure the global minimum is used instead of the local minimum nearest the rule-of-thumb configuration. Results are similar for the UDL CS case using either the particle swarm or sequential quadratic programming method.

Since $K > 0.3$ at all $m < 30$ for every loading/boundary condition combination, k_o is on the same order of magnitude as k_r. By comparing Figs. 2.2 and 2.3, we can see that changes to condition number

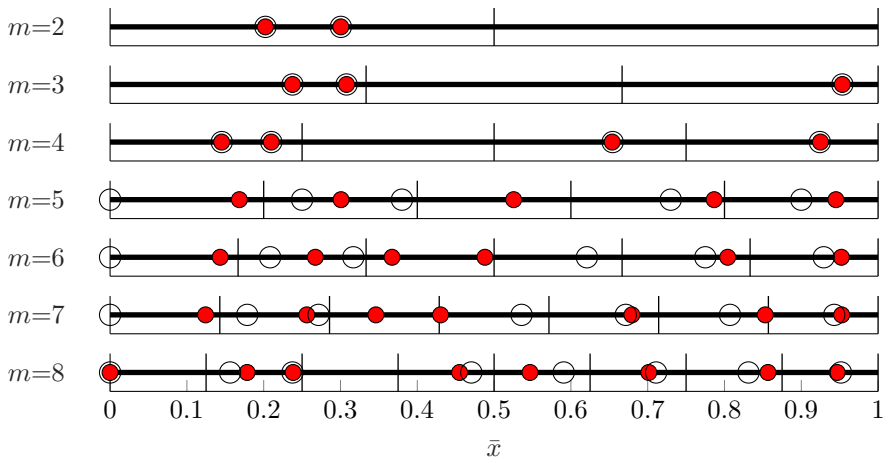

Figure 2.7. Optimal (red dots) and rule-of-thumb (black circles) sensor configurations for a UDL loading configuration and CS boundary conditions at various m. The vertical lines indicate the loading segments.

within an order of magnitude typically result in only small changes in estimation error. It is therefore likely that predictions using either the rule-of-thumb or optimal sensor configuration would yield similar results even at relatively low K. In contrast, the naïve condition number ratio $K_n = \kappa_o/\kappa_n$ quickly falls below 0.1 with increasing m for all configurations, indicating an order-of-magnitude difference or greater in condition numbers between the naïve and locally-optimal configurations, and a corresponding significant increase in sensitivity to noise.

2.2.2 Case Studies

We present two case studies to demonstrate how an optimized sensor placement leads to more accurate inverse calculations of distributed loading. The first case study inverse-calculates the static pressure loading on an aircraft wing, while the second seeks to determine the applied piecewise UDL loading on a clamped-clamped beam. Before describing the case studies in detail, we first consider the use of discretized UDL or LDL representations of distributed loads.

If an arbitrary truth function is approximated in a least-squares sense using a UDL or LDL function, the accuracy will depend on the number of loading segments, l. The mean integrated relative error of an

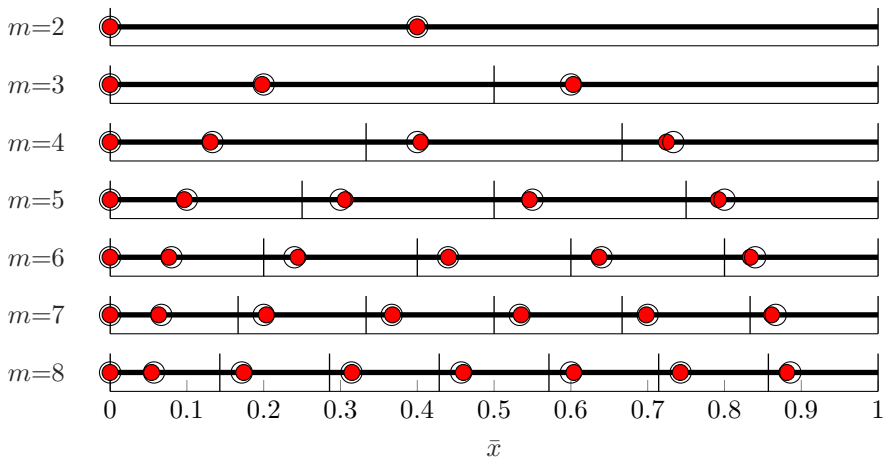

Figure 2.8. Optimal (red dots) and rule-of-thumb (black circles) sensor configurations for an LDL loading configuration and CF boundary conditions at various m. The vertical lines indicate the loading segments.

approximating function $f_a(x)$ compared to a truth function $f_t(x)$ is defined as

$$e_{f_a} = \frac{\int_0^L |f_t(x) - f_a(x)| dx}{\int_0^L |f_t(x)| dx}, \tag{2.18}$$

where the subscript on e is the approximating function. To investigate the relationship between e and l, a random truth function is generated by interpolating five points between 0 and L via cubic spline interpolation. Three of the five points are placed randomly between 0 and L, and the remaining points are placed at the beam's ends. Each point is assigned a random value between 2 and 10. A UDL function with l segments is fit to the resulting truth function by setting the value of each segment to the mean value of the truth function across that segment. An LDL function with l segments is fit in a least-squares sense to the resulting truth function. The script used to generate the best-case LDL fit is available in Ref. [82]. For each l, ten truth functions are generated, and the average error between the truth functions and the UDL and LDL approximations is presented in Fig. 2.13. The figure shows that a best-fit LDL function converges at lower l than a best-fit UDL function. The LDL error curve has a slight advantage because an LDL with l segments has $k = l + 1$ control points, but shifting the LDL error curve a unit to the right to convert the x axis to k yields similar results to those shown.

Fig. 2.13 suggests that an LDL is preferred when the loading is continuous. However, the second case study illustrates that UDL is better able to inverse-calculate a discontinuous truth function.

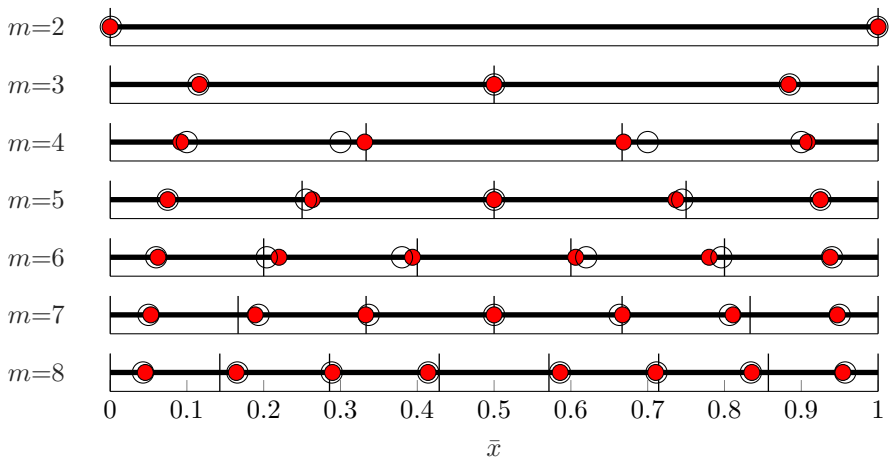

Figure 2.9. Optimal (red dots) and rule-of-thumb (black circles) sensor configurations for an LDL loading configuration and SS boundary conditions at various m. The vertical lines indicate the loading segments.

2.2.2.1 Aircraft Wing

This case study is based on the aircraft pressure loading reported in Ref. [83]. Consider a turbo-jet-propelled fighter plane with a wing length $L = 5.5$ m. The aluminum wing ($E = 70$ GPa) is assumed to have CF boundary conditions and to be uniform along its length with a thickness of 0.18 m and a moment of inertia of 8×10^{-4} m^4. At a Mach number of 0.8, the shape of the static load distribution as a function of distance along the wing is shown in Ref. [83] and reproduced as the truth loading in Fig. 2.15. This load distribution is obtained by integrating the measured pressure distribution along the wing's chord. An LDL approximation with 100 uniformly-spaced control points is used to synthesize the corresponding strain at any locations along the wing using Eq. (2.13). The high-resolution LDL loading used to calculate the forward strains is an adequate approximation of the desired continuous loading.

The synthesized strain data are now used to reproduce an LDL approximation of the original loading with $k = 8$. Three sensor configurations of eight sensors each are used to predict the loading. These configurations include the rule-of-thumb configuration for an LDL with CF boundary conditions described in Table 2.2 ($\boldsymbol{\xi}_r$), the locally optimal sensor configuration nearest the rule-of-thumb configuration ($\boldsymbol{\xi}_o$), and a cantilevered-like naïve configuration ($\boldsymbol{\xi}_n$). The three sensor configurations are shown in Fig. 2.14. The sensor placements $\boldsymbol{\xi}_r$ and $\boldsymbol{\xi}_o$ are similar, while $\boldsymbol{\xi}_n$ is only similar to the other configurations at the root

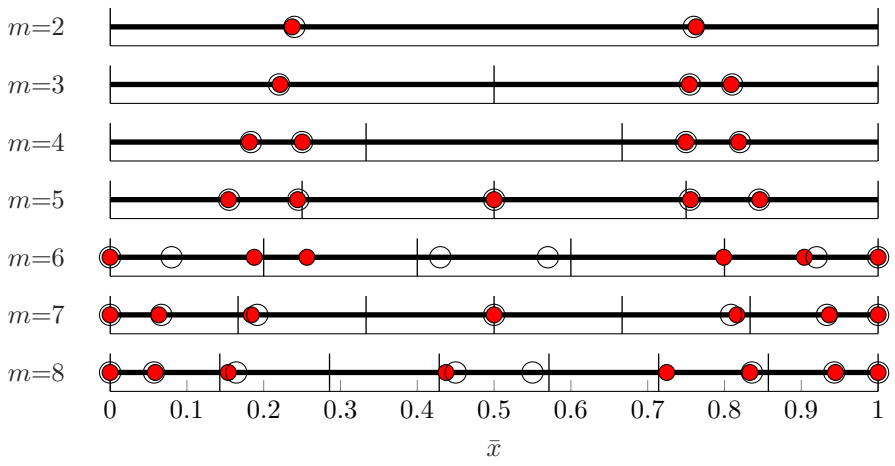

Figure 2.10. Optimal (red dots) and rule-of-thumb (black circles) sensor configurations for an LDL loading configuration and CC boundary conditions at various m. The vertical lines indicate the loading segments.

and high spanwise locations. The condition numbers of the influence matrices associated with the three configurations are $\kappa_r = 432$, $\kappa_o = 431$, and $\kappa_n = 2978$.

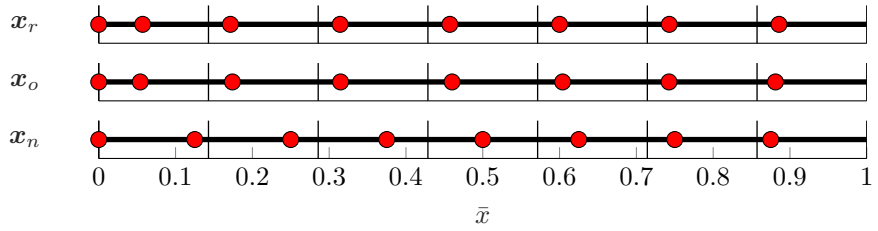

Figure 2.14. Rule-of-thumb, refined, and naïve sensor configurations for a cantilevered beam with assumed LDL loading and $m = 8$.

For each sensor configuration, the load distribution is reconstructed from the synthesized strain data using Eq. 2.13. A typical load reconstruction for each sensor configuration is shown in Fig. 2.15, where q_t is the true load profile, and q_{max} is the largest value of q_t. Load distributions q_r, q_o, and q_n are predicted using sensor configurations $\boldsymbol{\xi}_r$, $\boldsymbol{\xi}_o$, and $\boldsymbol{\xi}_n$, respectively. The strain data used to generate the reconstruction are corrupted with random noise with a standard deviation of 0.1% of each strain measurement from the rule-of-thumb configuration. The same noise vector is applied to all sensor configurations for consistency. For the load reconstruction in Fig. 2.15, $e_{x_r} = 3.51\%$, $e_{x_o} = 3.57\%$, and $e_{x_n} = 14.94\%$. The results using $\boldsymbol{\xi}_r$ and $\boldsymbol{\xi}_o$ are nearly identical, while the results using $\boldsymbol{\xi}_n$ have half an order of magnitude more error. Note that e_{x_o}

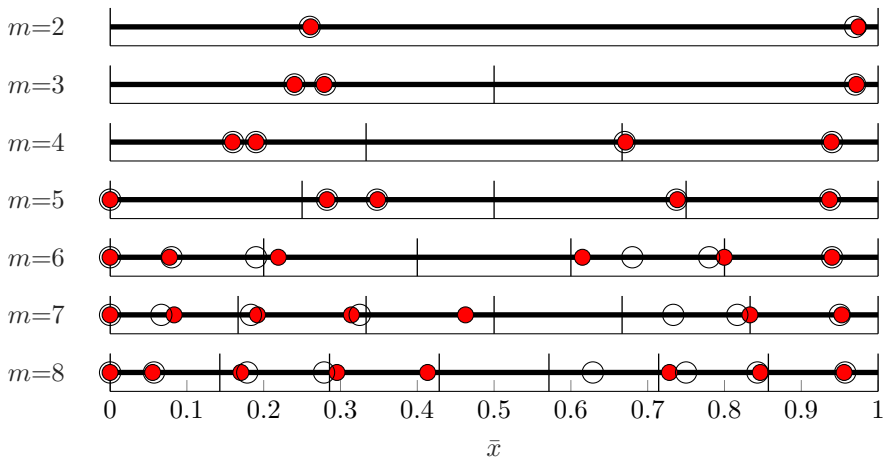

Figure 2.11. Optimal (red dots) and rule-of-thumb (black circles) sensor configurations for an LDL loading configuration and CS boundary conditions at various m. The vertical lines indicate the loading segments.

is slightly higher than e_{x_r}, despite the influence matrix associated with $\boldsymbol{\xi}_o$ having a slightly lower condition number. From our trials, this result is not atypical. The difference between the two errors depends on the specific noise profile applied to the strain data. This shows that error in the reconstruction is insensitive to changes in condition number as long as the condition number is near a minimum. Fig 2.16 shows how error evolves with the standard deviation of the applied noise (referred to as the "noise level"). Noise with a known standard deviation (presented as a percentage of each strain measurement) is applied to each set of strain measurements, the load profiles are reconstructed, and the error between each reconstruction and the truth loading is calculated. The presented error is the average error over 1000 applied noise profiles. The mean integrated relative error increases linearly with the amount of noise on the strain data regardless of sensor configuration. However, the slope corresponding to the $\boldsymbol{\xi}_r$ and $\boldsymbol{\xi}_o$ configurations is significantly less than that of the naïve configuration. Hence, the errors in the predicted loading using the rule-of-thumb or optimal sensor configurations are less sensitive to noise in the inputs than predictions using a naïve configuration.

2.2.2.2 Piecewise UDL Loading

Consider a beam of length $L = 3.5$ m. The beam is constructed of steel ($E = 200$ GPa) with a square cross section of side length $h = 0.3$ m and CC boundary conditions. A piecewise UDL with eight uniformly-spaced control points and $p = [10, 5, 0, 0, 3, -3, 7, -8]$ is applied to the beam. In this case, the strain at the

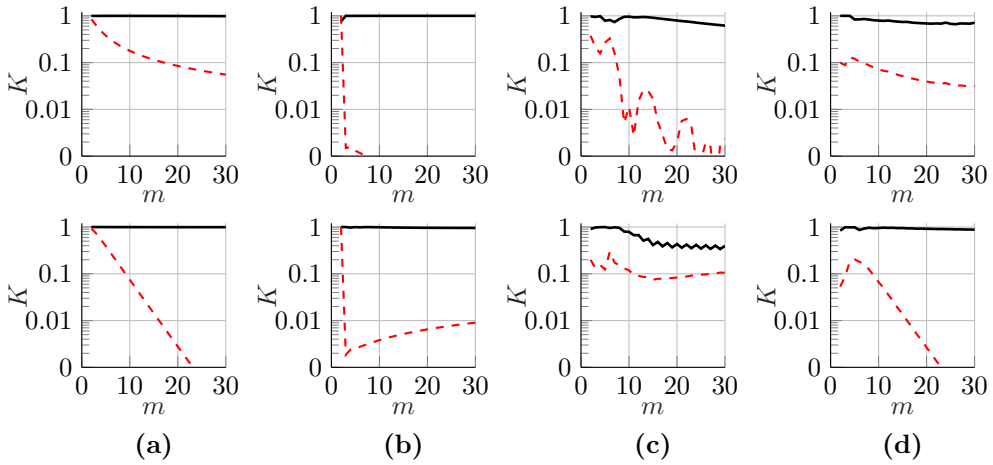

Figure 2.12. Condition number ratio (K, black, solid) and naïve condition number ratio (K_n, red, dashed) using different numbers of sensors for UDL (top) and LDL (bottom) assumed loading configurations and (a) CF, (b) SS, (c) CC, and (d) CS boundary conditions.

sensor locations may be calculated directly using the analytical influence coefficient matrix for the applied UDL.

The synthesized strain data are used to inverse-calculate the applied UDL. Like in the preceding case study, three sensor configurations of eight sensors each are used to predict the loading. The configurations include the rule-of-thumb configuration for a UDL with CC boundary conditions described in Table 2.1 ($\boldsymbol{\xi}_r$), the locally optimal sensor configuration nearest the rule-of-thumb configuration ($\boldsymbol{\xi}_o$), and a clamped-like naïve configuration. The three configurations are shown in Fig. 2.17. In this case, $\boldsymbol{\xi}_r$ and $\boldsymbol{\xi}_o$ are similar, but not as similar as in the wing case study. The naïve configuration, $\boldsymbol{\xi}_n$, is similar to the other two configurations except for the two sensors at the endpoints. The condition numbers of the influence matrices associated with the three configurations are $\kappa_r = 40.36$, $\kappa_o = 34.58$, and $\kappa_n = 680.44$.

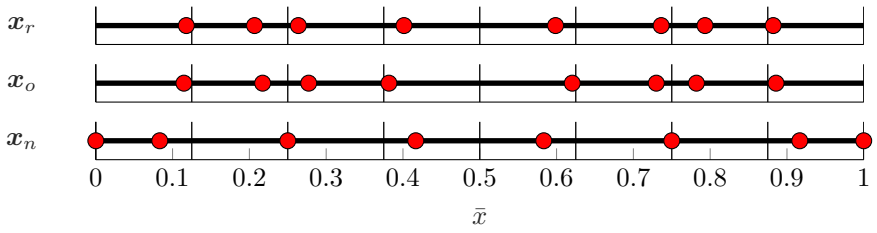

Figure 2.17. Rule-of-thumb, refined, and naïve sensor configurations for a clamped-clamped beam with assumed UDL loading and $m = 8$.

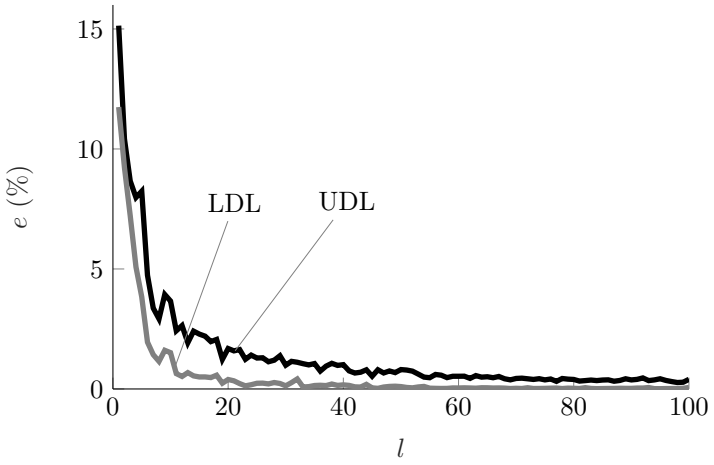

Figure 2.13. Integrated relative error between an arbitrary truth loading and the best-fit UDL or LDL for different numbers of segments l. Each point represents the average error among 10 truth configurations.

The load distribution is inverse-calculated for each sensor configuration in the same way as the previous case study. A typical inverse-calculation for each sensor configuration is shown in Fig. 2.18. The strain data used to generate the reconstruction are corrupted with random noise with a standard deviation of 2% (relative to the strains measured in the rule-of-thumb sensor configuration). The same noise vector is applied to all sensor configurations for consistency. For the load reconstruction in Fig. 2.18, $e_{x_r} = 20.41\%$, $e_{x_o} = 20.33\%$, and $e_{x_n} = 300.24\%$. In this case, since the approximating UDL function can exactly determine the truth loading, the prediction error is purely due to measurement error. Applying no noise to the input data yields a perfect reconstruction for all three sensor configurations. The error associated with the naïve configuration is much higher than the other two configurations, and the predicted distribution does not resemble the truth distribution. The prediction results associated with $\boldsymbol{\xi}_r$ and $\boldsymbol{\xi}_o$ are similar to each other as expected, and approximate the shape of the truth function well.

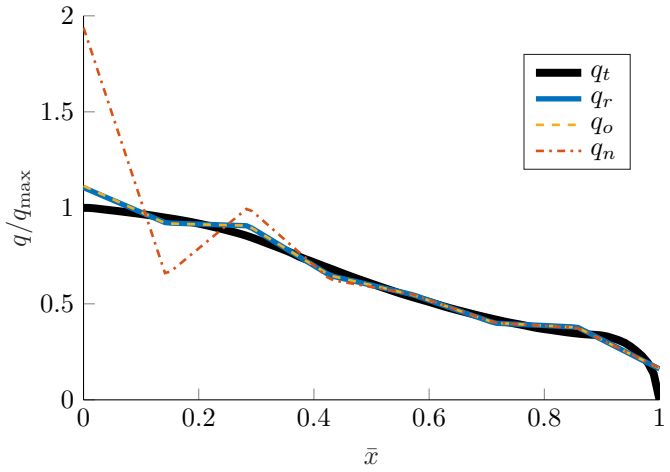

Figure 2.15. Normalized truth and approximate loading on a cantilevered aircraft wing. The truth loading q_t is reproduced from [83]. Approximate loads are generated using an LDL with eight control points and 0.1% added noise.

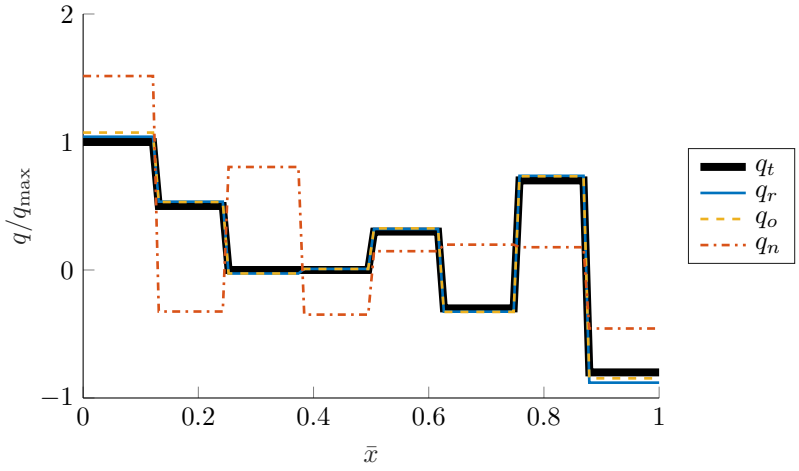

Figure 2.18. Normalized truth and approximate loading on a clamped-clamped beam. Approximate loads are generated using a UDL with 8 control points and 2% added noise.

Fig. 2.19 shows how error evolves with standard deviation of the applied noise. Noise with a known standard deviation (presented as a percentage of each strain measurement) is applied to each set of strain measurements, the load profiles are reconstructed, and the error between each reconstruction and the truth

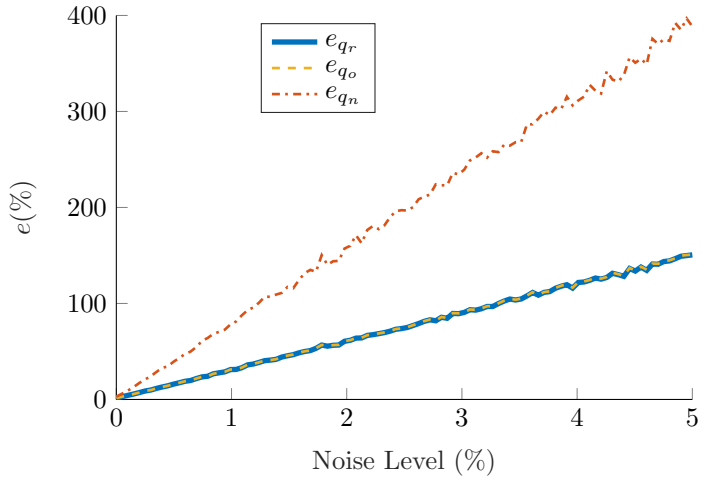

Figure 2.16. Mean integrated relative error versus strain gauge noise level for an assumed LDL load configuration with cantilevered (CF) boundary conditions using eight sensors. Displayed error is the average over 1000 random noise profiles.

loading is calculated. The presented error is the average error over 1000 applied noise profiles. At a noise level of 0%, the error for all three configurations is 0% as expected. Similar to the LDL case study in Section 2.2.2.1, the mean integrated relative error increases linearly with the amount of noise on the strain data. The slope corresponding to the $\boldsymbol{\xi}_r$ and $\boldsymbol{\xi}_o$ configurations is significantly less than that of the naïve configuration. Hence, the errors in the predicted loading using the rule-of-thumb or optimal sensor configurations are much less sensitive to noise in the inputs than predictions using a naïve configuration. Results using the naïve configuration yield output errors over 100% for input noise levels over 1.8%, while the rule-of-thumb and optimal configurations yield less than 100% output noise for noise levels up to 12.2%. Further, the results from the rule-of-thumb and optimal configurations are nearly identical for this case where $K = 0.86$, which shows that results are insensitive to changes in condition number near condition number minima. An optimal or near-optimal sensor configuration can increase the robustness of the solution to input noise by nearly an order of magnitude when using eight sensors. The trends shown in Fig. 2.12 suggest that the advantage would increase with increasing numbers of sensors.

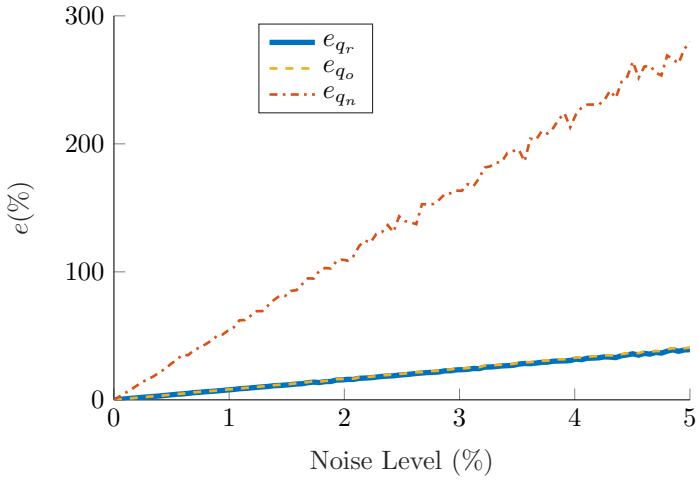

Figure 2.19. Mean integrated relative error versus strain gauge noise level for an assumed UDL load configuration with CC boundary conditions using 8 sensors. Displayed error is the average over 1000 random noise profiles.

2.3 Conclusions

An influence coefficient method capable of predicting general static distributed loading on beam-like structures is presented here. The method approximates arbitrary distributed loading as LDL or UDL functions, defined using control points with set locations and variable magnitudes. The simple form of the LDL and UDL functions allows the influence coefficient matrix to be derived analytically. The spatial resolution of the resulting force estimate is limited by the number of force control points distributed across the beam, which is itself limited by the number of structural response sensors. The accuracy of the force estimate is highly dependent on both the noise level of the strain data and the sensor placement. The present work includes a thorough study of optimal sensor placements for various numbers of sensors and structural boundary conditions. Patterns seen across the optimal sensor configurations are further used to construct rules of thumb for sensor placement that can guide sensor system design on beam-like structures so that reasonable approximations of the applied load may be obtained without directly optimizing the sensor system. Results from the presented case studies show that our rules of thumb can be as robust in practice as optimal configurations. Without guidance from the optimization studies in the present work, engineers would need

to rely on their intuition when designing sensor configurations, which could easily lead to ill-conditioned systems and erroneous results.

The present work is the first study to construct the influence matrix using analytical relationships between the applied load and internal moment. Hence, we are able to place sensors at arbitrary locations, which allows for the use of continuous optimization methods. Using these optimization techniques on a continuous domain, we show that the condition number of the influence matrix is a good surrogate for error, but that an optimal condition number does not necessarily correspond exactly to an optimal error. Sensor configurations corresponding to near-optimal condition numbers may perform as well or better than the configuration with the optimal condition number.

Finally, a few limitations of the present technique are noted along with their possible workarounds. First, as the number of sensors increases, the matrix condition number tends to increase. A large number of control points is necessary to resolve forces with short-wavelength spatial variation, which may lead to a large condition number. The effects of ill-conditioning may be reduced for large matrices by using regularization or a rank-reduction algorithm similar to Ref. [19]. Second, the analytical equations for the influence matrix presented here are only appropriate for beam-like structures with boundary conditions at the endpoints. Deriving similar equations for more complicated structures would likely be infeasible. Instead, the influence matrix for an assumed UDL or LDL distribution could be calculated numerically using commercial finite element analysis packages. The values in each column of the influence matrix can be calculated as either internal moment or strain response values at all sensor locations due to a unit value of the corresponding control point. Previous studies have used this method [13, 14, 19]. While the analytical equations and associated results presented here are not a replacement for numerical methods, they may serve as guidelines for practitioners in the absence of detailed models.

Chapter 3

Harmonic Distributed Force Estimation

Systems such as rocket engines, submarine propellers, and airplane wings are routinely subject to distributed dynamic loads, but these loads are often difficult to measure directly. Given a structural dynamic model and a set of steady-state response measurements, it is theoretically simple to estimate the harmonic input force(s) that produced the response by inverting the FRF matrix. However, in practice, these inverse force determination problems are prone to numerical errors. Classical inversion techniques can be augmented using Tikhonov regularization, which discourages overfitting and enforces a unique solution by penalizing solutions with large magnitudes or large gradients. However, the prior information that can be included in a Tikhonov regularization scheme is limited. Methods based on Bayesian inference have recently emerged as powerful input estimation schemes incorporating prior knowledge of the form of the force, thereby reducing the number of sensors required for an adequate solution. In this chapter, we propose a formulation for generalized Tikhonov regularization that enables a force prior to be embedded in the regularization term. Numerical results show that this novel Tikhonov regularization method yields high-quality distributed acoustic pressure estimates using synthesized acceleration measurements from a steel plate. The inverse load identification technique is also used with experimental measurements and shows strong agreement with the the experimentally measured pressure field.

3.1 Methods

The force estimation method described here inverts the system FRF by using a novel Tikhnov regularization scheme to incorporate prior knowledge of the spatial form of the force. First, we introduce the system equations and define the FRF matrix. Next, we introduce an interpolation-based method for reducing

the ill-posedness of the problem by reducing the number of force parameters. Results show that this interpolation method is unnecessary when regularization is used. We then derive the novel generalized Tikhonov regularization method that allows a spatial prior to be incorporated into the inversion process. Finally, we introduce the effective independence method for sensor system design along with several error metrics and other quantities that are used in the presentation of the results.

3.1.1 Physical Equations

The equations of motion for a damped linear structure in modal coordinates are

$$\ddot{\boldsymbol{\eta}} + 2\Lambda\Omega\dot{\boldsymbol{\eta}} + \Omega^2\boldsymbol{\eta} = \Phi^T\boldsymbol{u}, \tag{3.1}$$

where $\boldsymbol{\eta}$ is a vector of modal displacements, Φ is the mass-normalized matrix of normal modes, $\boldsymbol{u}$ is the applied force in physical coordinates, Λ is a diagonal matrix where the j^{th} diagonal entry is the j^{th} modal damping ratio ζ_j, and Ω is a diagonal matrix where the j^{th} diagonal entry is the j^{th} structural natural frequency ω_j. The relationship between modal displacements $\boldsymbol{\eta}$ and physical displacements $\boldsymbol{y}$ is

$$\boldsymbol{y} = \Phi\boldsymbol{\eta}. \tag{3.2}$$

Assuming harmonic forcing of the form

$$\boldsymbol{u} = \text{Re}\left(\boldsymbol{U}e^{i\omega t}\right), \tag{3.3}$$

where $\boldsymbol{U}$ is the complex-valued forcing amplitude, ω is the forcing frequency, t is time, and $i \equiv \sqrt{-1}$. At steady-state, the system response will take the same temporal form as the forcing, so Eqs. (3.1)—(3.3) can be used to yield a relationship between the complex-valued, steady-state acceleration response amplitude, $\boldsymbol{Y}$, and forcing amplitude, $\boldsymbol{U}$,

$$\boldsymbol{Y}(\omega) = H(\omega)\boldsymbol{U}(\boldsymbol{\omega}) = \sum_{j=1}^{N} \frac{-\omega^2\Phi_j\Phi_j^T}{\omega_j^2 + 2i\zeta_j\omega_j\omega - \omega^2}\boldsymbol{U}(\boldsymbol{\omega}), \tag{3.4}$$

where N is the number of included modes. The ratio $\boldsymbol{Y}(\omega)/\boldsymbol{U}(\omega) \equiv H(\omega)$ is known as the acceleration frequency response function (FRF). Other FRF formulations can be derived for other types of structural response measurements, such as displacement, strain, or velocity. The FRF matrix can be obtained from a

structural dynamic model (e.g., a finite element model) or can be populated with post-processed experimental data.

In the inverse force determination problem, response measurements will only be available at certain degrees of freedom (DOFs). In this case, the relationship between the response and forcing amplitudes can be expressed as

$$\boldsymbol{Y}(\boldsymbol{\xi}, \omega) = H(\boldsymbol{\xi}, \omega)\boldsymbol{U}(\omega), \tag{3.5}$$

where $\boldsymbol{\xi}$ is a sensor configuration that removes all rows from H except those associated with measured DOFs. When the there are more forces to estimate than there are response measurements, the problem is an under-determined (i.e., ill-posed). In practice, systems subject to distributed loading are almost certain to be ill-posed because the number of discrete force estimates required to spatially resolve the loading will exceed the number of response measurements that can be practically obtained. The following sections propose a technique that incorporates additional information into the system inversion, thereby enabling unique solutions to ill-posed inverse problems of this form.

3.1.2 Force Basis

The dimension of $\boldsymbol{U}(\omega)$ in Eq. (3.5) may be reduced by representing the continuous, distributed force as a linear interpolation between sparse control points. Suppose the distributed load can be approximated as a linear combination of interpolating functions and frequency-varying amplitudes

$$\boldsymbol{U}(\omega) = B\hat{\boldsymbol{U}}(\omega), \tag{3.6}$$

where B is an interpolation matrix and $\hat{\boldsymbol{U}}(\omega)$ is a vector of amplitudes. Control points with amplitude $\hat{\boldsymbol{U}}(\omega)$ are placed around the edge and interior of the area where the load is applied, and B maps the contribution from each control point onto the force at each DOF. Substituting Eq. (3.6) into Eq. (3.5) yields a relationship between the control point magnitudes and system response

$$\boldsymbol{Y}(\boldsymbol{\xi}, \omega) = \hat{H}(\boldsymbol{\xi}, \omega)\hat{\boldsymbol{U}}(\omega). \tag{3.7}$$

where $\hat{H} = HB$ can now be treated as a single matrix that can be inverted to estimate the force. The number of unknowns is now equal to the number of control points rather than the number of DOFs. Including an interpolation scheme as part of the FRF is not equivalent to estimating a set of sparse point loads and inter-

polating afterward. Including the interpolation into the FRF assumes a load at every DOF that is included in the calculation of the forward problem but parameterizes the load so that there are fewer unknowns to estimate.

The matrix B can be calculated numerically using Eq. (3.6) by setting one $\hat{U}_j = 1$ and all others equal to zero. The j^{th} column of B can be calculated by linearly interpolating the control points onto all structural DOFs. In the case of bilinear interpolation among uniformly-spaced control points on a rectangular grid, the force amplitude at any degree of freedom may be written in terms of the magnitudes of the surrounding control points

$$\begin{aligned} U_j = &\left(1 - \frac{x_j - x_0}{x_1 - x_0}\right)\left(1 - \frac{y_j - y_0}{y_1 - y_0}\right)\hat{U}_{00} + \left(1 - \frac{x_j - x_0}{x_1 - x_0}\right)\left(\frac{y_j - y_0}{y_1 - y_0}\right)\hat{U}_{01} \\ &+ \left(\frac{x_j - x_0}{x_1 - x_0}\right)\left(1 - \frac{y_j - y_0}{y_1 - y_0}\right)\hat{U}_{10} + \left(\frac{x_j - x_0}{x_1 - x_0}\right)\left(\frac{y_j - y_0}{y_1 - y_0}\right)\hat{U}_{11}, \end{aligned} \tag{3.8}$$

where x_j and y_j are the coordinates of the j^{th} degree of freedom, $\hat{U}$ is a control point at coordinates (x, y) and the subscripts represent the control point immediately below (0) or above (1) the degree of freedom of interest in the x and y directions respectively. For example, $\hat{U}_{01}$ is the control point immediately below DOF j in the x direction, and immediately above DOF j in the y direction. If B is the identity matrix, control points are placed at every DOF, and the problem is equivalent to Eq. (3.5).

3.1.2.1 Derivation of the regularization term

The proposed regularization technique, though fundamentally deterministic, is derived using Bayesian inverse methods. Frequency dependence is dropped from the notation in the following derivation for brevity. Bayes' rule can be expressed as

$$p(\hat{\boldsymbol{U}}|\boldsymbol{Y}) \propto p(\boldsymbol{Y}|\hat{\boldsymbol{U}})p(\hat{\boldsymbol{U}}), \tag{3.9}$$

where $p(\hat{\boldsymbol{U}}|\boldsymbol{Y})$ is the posterior distribution that represents the probability of a force configuration given the measured system response, $p(\boldsymbol{Y}|\hat{\boldsymbol{U}})$ is the likelihood distribution that represents the probability of the measured system response given a force configuration, and $p(\hat{\boldsymbol{U}})$ is the prior distribution that represents the probability that a given force configuration occurs. The likelihood is modeled as a complex normal distribution:

$$p(\boldsymbol{Y}|\hat{\boldsymbol{U}}) \sim \mathcal{N}_c(\hat{H}\hat{\boldsymbol{U}}, \sigma_n^2\mathbf{I}), \tag{3.10}$$

where σ_n^2 is the variance of additive noise (physically, the noise's power). The prior distribution is also modeled as a complex normal distribution:

$$p(\hat{\boldsymbol{U}}) \sim \mathcal{N}_c(\mathbf{0}, \sigma_u^2 \Sigma_{\hat{U}}), \tag{3.11}$$

where $\Sigma_{\hat{U}}$ is the force covariance matrix, and σ_u determines the overall force level. We propose the following form of the force covariance matrix:

$$\Sigma_{\hat{U},jk} = \frac{\hat{U}_{p,j}\hat{U}_{p,k}^{\dagger}}{\hat{\boldsymbol{U}}_p^{\dagger}\hat{\boldsymbol{U}}_p} \exp\left(\left(1 - \frac{1}{s}\right)\frac{d_{jk}}{d_{\max}}\right), \tag{3.12}$$

where $\Sigma_{\hat{U}}$ is a covariance matrix describing the correlation between entries in $\hat{\boldsymbol{U}}$, $\hat{\boldsymbol{U}}_p$ is a prior estimate of $\hat{\boldsymbol{U}}$, d_{jk} denotes the Euclidean distance between $\hat{U}_j$ and $\hat{U}_k$, $d_{\max}$ is the largest Euclidean distance between any two $\hat{U}$, s is a prior correlation parameter, and $*^{\dagger}$ denotes the conjugate transpose. The values for $\hat{\boldsymbol{U}}_p$ can be chosen based on simulation results, measured values, or practitioner experience. A vector of ones indicates no prior knowledge and penalizes forces with a large magnitude. The parameter s defines the strength of the spatial correlation between parameter pairs, where $s = 0$ indicates no spatial correlation, and $s = 1$ indicates perfect correlation. The analyst chooses s based on the spatial form of the force. Larger values more strictly penalize rapid spatial variation in estimated loads, and a value of 0 indicates the loads are completely independent. Spatial correlation is plotted versus normalized distance for a few values of s in Fig. 3.1. A value of $s = 0.6$ is used throughout the present work.

Substituting Eqs. (3.10) and (3.11) into Eq. (3.9), defining $\lambda^2 = \sigma_n^2/\sigma_u^2$, and rearranging yields an expression for the posterior distribution,

$$p(\hat{\boldsymbol{U}}|\boldsymbol{Y}) \propto \exp\left[-\frac{1}{\sigma_n^2}\left(\left|\left|\ddot{\boldsymbol{Y}} - \hat{H}\hat{\boldsymbol{U}}\right|\right|_2^2 + \lambda^2 \hat{\boldsymbol{U}}^{\dagger}\Sigma_{\hat{U}}^{-1}\hat{\boldsymbol{U}}\right)\right]. \tag{3.13}$$

The first term inside the parentheses in Eq. (3.13) comes from the likelihood distribution, while the second term comes from the prior distribution. Though not in standard form, Eq. (3.13) describes a complex normal distribution on $\hat{\boldsymbol{U}}$. Rearranging to standard form and extracting the mean of that distribution yields a closed-form solution:

$$\hat{\boldsymbol{U}} = ((\hat{H})^{\dagger}(\hat{H}) + \lambda^2 \Sigma_{\hat{U}}^{-1})^{-1}(\hat{H})^{\dagger}\boldsymbol{Y}. \tag{3.14}$$

The prior distribution of $\hat{\boldsymbol{U}}$ enables generalized Tikhonov regularization, and warrants additional discussion. Components of $\hat{\boldsymbol{U}}$ that are *a priori* expected to be larger receive larger values in the diagonal of

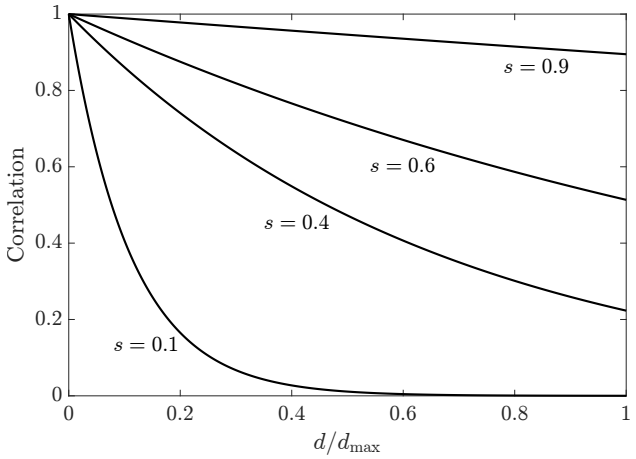

Figure 3.1. Correlations on the off-diagonal of Σ versus normalized distance for a few values of the correlation parameter, s.

$\Sigma_{\hat{U}}$. This means that the "variances" of those components are higher, so large values are penalized less. Each off-diagonal entry describes the correlation between a pair of loads. If two loads are highly correlated, there is a harsh penalty when their values are different. Load components that are close together have higher correlations in Eq. (3.12) because the harmonic force coefficients are expected to be spatially smooth. A larger value of s indicates a preference for greater smoothness.

3.1.3 Regularization

Equation (3.7) can be inverted directly to estimate the applied load, but the problem is ill-posed if the number of control points exceeds the number of measurements. For complicated load distributions like those commonly seen in steady aerodynamic or acoustic loading, the number of measurements required for an even-determined problem can still be infeasible even when using interpolation to reduce the number of unknowns. A regularization term based on the force prior term in Sec. 3.1.2.1 can be introduced to include additional assumptions about the problem that help the inversion to yield a unique, meaningful solution. We propose a regularization term that allows prior knowledge of the expected force to be included.

The inverse problem Eq. (3.7) can be reformulated as an equivalent least-squares minimization problem

$$\hat{\boldsymbol{U}}(\omega) = \underset{\hat{\boldsymbol{U}}}{\arg\min} \quad ||H(\boldsymbol{\xi}, \omega) B \hat{\boldsymbol{U}}(\omega) - \boldsymbol{Y}(\boldsymbol{\xi}, \omega)||_2^2. \tag{3.15}$$

Calculating the Cholesky decomposition $\Sigma_{\hat{U}}^{-1} = R^{\dagger}R$ of the force covariance in Eq. (3.12), substituting into the prior term from Eq. (3.13), and combining the prior term from Eq. (3.13) with Eq. (3.15) yields a minimization problem with a generalized Tikhonov penalty term,

$$\hat{\boldsymbol{U}}(\omega) = \underset{\hat{\boldsymbol{U}}}{\arg\min} \quad ||H(\boldsymbol{\xi},\omega)B\hat{\boldsymbol{U}}(\omega) - \boldsymbol{Y}(\boldsymbol{\xi},\omega)||_2^2 + \lambda^2(\omega)||R\hat{\boldsymbol{U}}||_2^2. \tag{3.16}$$

The value of $\lambda(\omega)$ may be calculated at each frequency using the L-curve method [84]. The regularized force reconstruction can be calculated using Eq. (3.14) or via generalized singular value decomposition [40]. When $\hat{\boldsymbol{U}}_p = 1$ and $s = 0$, the regularization scheme reduces to standard-form Tikhonov regularization.

We now briefly note the difference between the formulation in Eq. (3.16) and classical generalized Tikhonov regularization. The pressure field estimation equation using classical generalized Tikhonov regularization is

$$\hat{\boldsymbol{U}}(\omega) = \underset{\hat{\boldsymbol{U}}}{\arg\min} \quad ||H(\boldsymbol{\xi},\omega)B\hat{\boldsymbol{U}}(\omega) - \boldsymbol{Y}(\boldsymbol{\xi},\omega)||_2^2 + \lambda^2(\omega)||L(\hat{\boldsymbol{U}} - \hat{\boldsymbol{U}}_p)||_2^2, \tag{3.17}$$

where L is either the identity matrix or a derivative operator [40]. In this form, the force prior is moved from the regularization matrix R to a bias term, and the regularization matrix is used to encourage qualities such as small estimation magnitudes (if L is the identity) or smoothness (if L is a derivative operator) in the global solution. The classical formulation is less flexible in practice than the formulation in Eq. (3.16) because the force prior is not agnostic of scale. Since the force prior has to have an accurate magnitude when used as a bias term, the numerical model for the prior must be very accurate, and the method cannot be used for the common case where the spatial form of the force can be modeled but the magnitude is unknown. When the prior is instead included in the regularization matrix, only the relative magnitudes in the force prior matter, and force components with a relatively large corresponding prior component are penalized less than force components with a relatively small prior component.

3.1.4 Effective Independence

The EI method is a common and efficient method for sensor placement. The EI method places sensors so that the linear independence of the mode shape matrix at the sensor points is maximized [85]. At each iteration, an effective independence matrix is calculated as

$$E = \Phi_r(\Phi_r^T\Phi_r)^{-1}\Phi_r^T, \tag{3.18}$$

where E is the effective independence matrix, and Φ_r is the mode shape matrix containing all modes with natural frequencies in the frequency range of interest and all degrees of freedom in the candidate set for sensor placement. The degree of freedom corresponding to the smallest diagonal entry of E is removed from the candidate set, and the process is repeated until the candidate set is reduced to the desired number of sensors.

3.1.5 Error Metrics

We define an error metric $e_{\hat{u}_a}$ so that force estimates can be directly compared across space and frequency

$$e_{u_a} = \frac{\int_A \int_{\omega_l}^{\omega_h} |\boldsymbol{U}(\omega) - \boldsymbol{U}_a(\omega)| d\omega dA}{\int_A \int_{\omega_l}^{\omega_h} |\boldsymbol{U}(x,\omega)| d\omega dA}, \tag{3.19}$$

where $\boldsymbol{u}$ is the truth load at all DOFs, $\boldsymbol{u}_a$ is an approximate load at all DOFs, and A is the area over which the load acts. The choice of ω_l is somewhat arbitrary but is larger than 0 since the problem tends to be ill-conditioned near zero regardless of sensor configuration when using acceleration measurements, and the large errors in this region tend to confound the interpretation of the error metric.

The frequency response assurance criterion (FRAC) is a standard tool in vibration analysis for checking the similarity between FRFs and is used here as a secondary error metric to check the similarity between force estimates and the truth. The FRAC takes values between zero and one where zero indicates no correlation and one indicates perfect correlation between the two vectors, and is defined in this context as

$$\text{FRAC} = \frac{|\sum_{\omega_l}^{\omega_h} \boldsymbol{U}(\omega)\boldsymbol{U}_a(\omega)^\dagger|^2}{\sum_{\omega_l}^{\omega_h} \boldsymbol{U}(\omega)\boldsymbol{U}(\omega)^\dagger \sum_{\omega_l}^{\omega_h} \boldsymbol{U}_a(\omega)\boldsymbol{U}_a(\omega)^\dagger}. \tag{3.20}$$

We also apply the modal assurance criterion (MAC), another standard tool often used to check the similarity between mode shapes, to check the similarity between the truth and estimated pressure distributions at a given frequency. Like the FRAC, the MAC takes values between 0 and 1, where a value of 1 indicates perfect correlation and a value of 0 indicates no correlation. The MAC as applied to pressure distributions is defined as

$$\text{MAC} = \frac{|\boldsymbol{U}^\dagger \boldsymbol{U}_a|^2}{(\boldsymbol{U}^\dagger \boldsymbol{U})(\boldsymbol{U}_a^\dagger \boldsymbol{U}_a)}. \tag{3.21}$$

3.1.6 Post-Processing

The force estimation methods described here produce a set of force parameters that describe the estimated force magnitude $\boldsymbol{U}$ at discrete locations. These discrete forces are converted to a pressure representation for direct comparison to a known pressure distribution. The force-to-pressure conversion is typically accomplished by normalizing the force magnitudes by an effective area over which they act. All of the force locations in the present work are arranged on a uniform rectangular grid, so the equivalent pressure at each force location is estimated as

$$\nu = \frac{U}{\Delta x \Delta y}, \tag{3.22}$$

where ν is the equivalent pressure magnitude, and Δx and Δy are the uniform horizontal and vertical distances between force locations. If an interpolating force basis is used, Δx and Δy are the distances between the final interpolated forces, not the force basis control points themselves. Equation (3.22) is used to convert experimental pressures to forces for error calculation via Eqs. (3.19), (3.20), and (3.21), and to convert force estimates to pressures for visualization.

The pressure is converted to a decibels (dB) scale via

$$\nu_{\text{SPL}} = 10 \log_{10} \left(\frac{\nu^2}{\nu_{\text{ref}}^2} \right), \tag{3.23}$$

where ν_{SPL} is the pressure in dB, ν is the fluctuating pressure amplitude, and ν_{ref} is the reference pressure ($\nu_{\text{ref}} = 20\mu$Pa in air at standard atmosphere and pressure).

3.2 Results

Our method is validated both numerically and experimentally. Section 3.2.1.1 validates the new Tikhonov regularization method on a simple pressure distribution and illustrates some features about how the method behaves for different numbers of sensors and parameters. Section 3.2.1.2 numerically investigates the efficacy of the method as applied to a more realistic configuration of a steel plate coupled to an acoustic duct. Section 3.2.2 experimentally validates the results from Section 3.2.1.2 using real experimental data from a coupled acoustic-structural system.

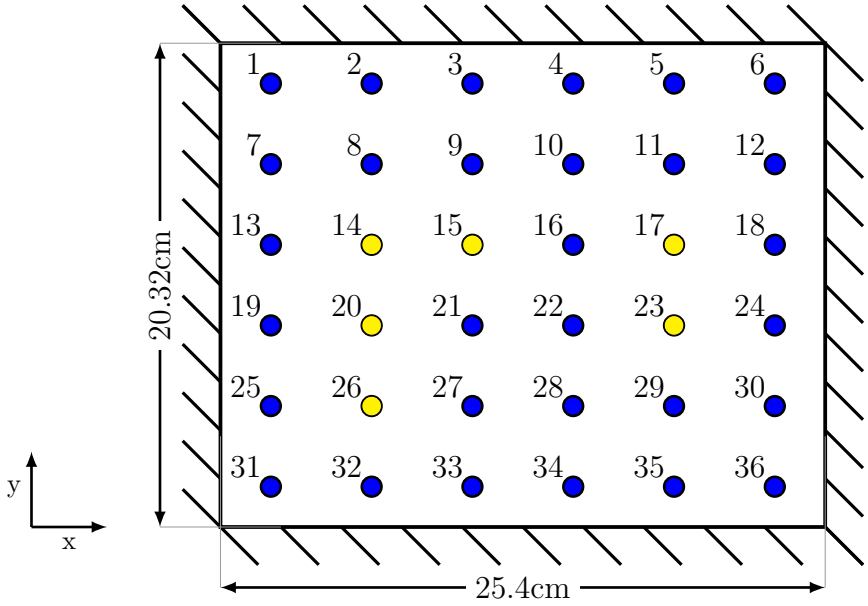

Figure 3.2. Schematic of the structural CCCC plate model. The numbers and circular markers (blue and yellow) indicate the locations and indices of structural DOFs for the simulated and experimental acoustic-structural system. The yellow markers indicate response measurement locations suggested by the EI method.

3.2.1 Numerical Validation

3.2.1.1 Parameter Study

We first study the reconstruction quality of the Tikhonov regularization method as a function of number of sensors, number of force parameters, and the choice of regularization scheme. Consider a rectangular steel plate of width $W = 25.4$ cm (10 in), height $L = 20.32$ cm (8 in), Young's modulus $E = 200$ GPa, density $\rho = 7700$ kg/m^3, and Poisson's ratio $\gamma = 0.3$. The plate is clamped on all sides (CCCC) and is shown in Fig. 3.2. A FEA model of the plate is used to calculate the structural natural frequencies and mode shapes using the commercial software ANSYS. The plate is subject to a frequency-independent distributed load of the form

$$\nu_t(x, y, \omega) = \text{sinc}\left(2\pi\left(\frac{x}{W} - \frac{1}{2}\right)\right)\text{sinc}\left(2\pi\left(\frac{y}{L} - \frac{1}{2}\right)\right), \tag{3.24}$$

which is a two-dimensional sinc load centered at the center of the plate and has three peaks in either direction. The pressure field is converted to force at every DOF by multiplying pressure by the effective area of that DOF. Tikhonov regularization is used to estimate the sinc loading on the plate using between $3 \leq n_s \leq 30$

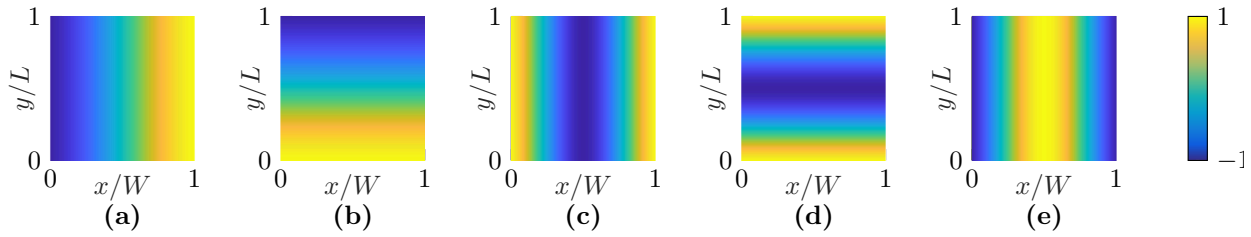

Figure 3.3. Representative acoustic pressure mode shapes on the plate surface computed using ANSYS. Mode (a) 5 ($\omega_n = 731.7$ Hz), (b) 9 ($\omega_n = 889.9$ Hz), (c) 27 ($\omega_n = 1595.2$ Hz), (d) 33 ($\omega_n = 1713.4$ Hz), and (e) 34 ($\omega_n = 1762.8$ Hz)

response measurements. Each estimation attempt assumes a force basis based on bilinear interpolation as proposed in Sec. 3.1.2 with between $2 \leq n_f \leq 21$ control points in each direction. For simplicity, the number of control points in each direction is equal, so the total number of control points on the plate is n_f^2. For each combination of n_f and n_s, the EI method is used to determine a suitable sensor configuration. Additionally, the force estimation is attempted using three regularization configurations: generalized regularization with a force prior calculated as the truth pressure value at each control point ($\hat{U}_p(x,y) = \nu(x,y)$) and $s = 0.6$, standard regularization with a penalty term based solely on estimation magnitude (($\hat{\boldsymbol{U}}_p = 1$)) and $s = 0$, and no regularization at all. For error calculation purposes, we let $\omega_l = 282$ Hz and $\omega_h = 2139$ Hz corresponding to the first and 14$^{\text{th}}$ structural natural frequencies.

The results of the parameter study are shown in Fig. 3.4. The error bounds in this figure are defined from 0-200% for all subfigures because force reconstructions with error in excess of 200% are typically unacceptable. When generalized regularization with a force prior and non-zero smoothing parameter is used, the error decreases as n_f increases due to an improved ability of the interpolating force basis to approximate the distributed loading (Fig. 3.4a). The highest error occurs in the overdetermined region ($n_s \geq n_f^2$) near the bottom of Fig. 3.4a. Classical system inversion theory suggests that without regularization, an even- or overdetermined system is required to obtain an acceptable solution, but an underdetermined system with $n_s < n_f^2$ may be adequate when using generalized regularization with a high-quality prior. Hence, priority should be given to increasing the force resolution over maintaining a determined system if it is known that the prior closely matches the truth. In this case where $\boldsymbol{U}_p = \boldsymbol{U}$, the error depends little on n_s since the

inversion process does not need additional information from the measurements to estimate the shape of the load.

Standard form regularization with only a magnitude-based penalty term and no smoothing parameter (Fig. 3.4b) yields much larger error at all combinations of n_s and n_f than the generalized regularization case. The error in this case also now depends strongly on n_s, where error is reduced as the number of sensors is increased. This suggests that the larger the difference between the prior and the truth force, the more error will be attenuated as additional sensors are used. Error also decreases as n_f is increased owing to the improved spatial resolution. Even when no prior knowledge of the form of the force is available, it may still be more advantageous to prioritize an adequate force resolution over maintaining a determined system by limiting the number of forces in the loading model. System inversion without regularization performs poorly at every combination of n_f and n_s. In this case, the best results are obtained when the system is overdetermined or even-determined ($n_s \geq n_f^2$), but the error exceeds 100% even in this region.

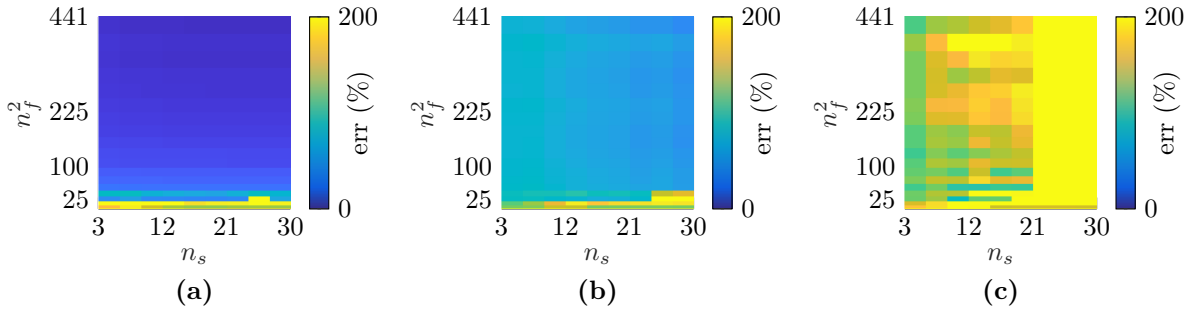

Figure 3.4. Percent relative error between the truth sinc loading and the loading estimated using Tikhonov regularization with (a) generalized regularization with $s = 0.6$ and $\boldsymbol{U}_p = \boldsymbol{U}$, (b) standard regularization with $s = 0$ and $\boldsymbol{u}_p = 1$, and (c) no regularization for various numbers of sensors and force parameters.

Fig. 3.5 shows the truth load and load reconstructions using generalized Tikhonov regularization for $n_s = 30$ and $n_f^2 = 441$ at $y/L = 1/\sqrt{2}$ and all values of x/W and f. Tikhonov regularization yields an overall high quality reconstruction. However, the reconstruction error is very large at low frequencies due to the typically low acceleration magnitudes and signal-to-noise ratios at low frequencies. These errors decrease at higher frequencies as the acceleration signal quality improves.

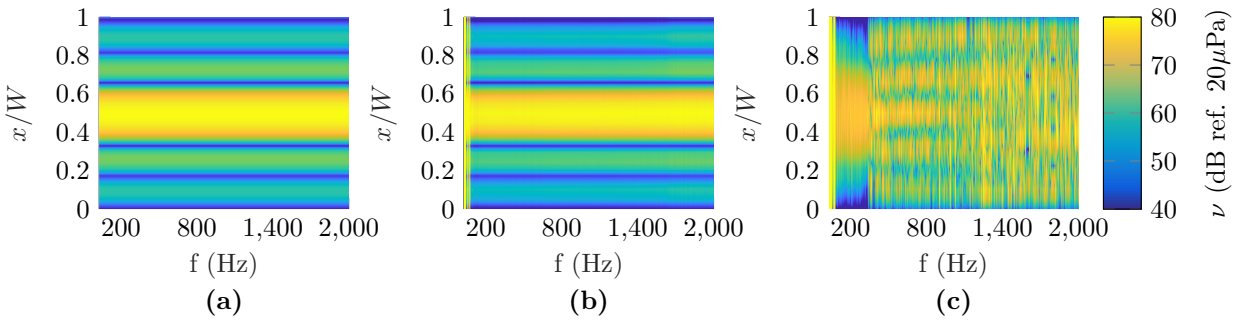

Figure 3.5. (a) Truth frequency-independent sinc pressure load at all x/W for $y/L = 1/\sqrt{2}$, (b) estimated force for $n_s = 30$ and $n_f^2 = 441$ using generalized Tikhonov regularization with $s = 0.6$ and $\hat{\boldsymbol{U}}_p = \boldsymbol{\nu}$, and (c) estimated force for $n_s = 30$ and $n_f^2 = 441$ using standard-form Tikhonov regularization with $s = 0$ and $\hat{\boldsymbol{U}}_p = 1$

3.2.1.2 Acoustic-Structural Simulation

Before conducting our experiment, we first build a numerical model of the experimental setup to validate both our method and our experimental results. A finite element (FEA) model of the system is built in ANSYS. A rigid-walled acoustic duct with dimensions of width $W = 25.4$ cm (10 in), height $L = 20.32$ cm (8in), and depth $D = 60.96$ cm (24in) is coupled on one end to the CCCC plate shown in Fig. 3.2. The plate is identical to the steel plate used in Sec. 3.2.1.1. The duct is filled with moist air (speed of sound $c = 346$m/s, density $\rho = 1.05$ kg/m^3). Some representative acoustic mode shapes on the steel plate surface are shown in Fig. 3.3. The plate is assumed to have a uniform structural modal damping ratio of $\zeta = 0.01$, the duct is assumed to have a boundary admittance of $\beta = 50$, and the plate and duct experience two-way fluid-structure coupling. The values of ζ and β are chosen arbitrarily, but represent a lightly damped plate structure and a duct that loses very little acoustic energy through its sides, respectively. A rectangular patch on the face of the duct, opposite the plate of $0.2 < x/W < 0.7$ and $0.2 < y/L < 0.7$, is assigned a FLOW load, which allows the patch to act as a speaker. The speaker patch is placed slightly off-center so that odd-numbered transverse modes are excited as they are due to asymmetries in the experimental setup. Harmonic analysis is performed between 200 Hz and 2000 Hz, and the structural response of the plate and the pressure at the plate surface are simulated at 500 evenly-spaced intermediate frequencies. The pressure and response represent the input and output of the structural system.

The plate dynamics are studied *in vacuo* using the same FEA model used in the full system described above, but decoupled from the duct. A modal analysis is used to compute the mode shapes of the plate with natural frequencies up to 4000 Hz, double the highest forcing frequency of interest. Assuming a uniform modal damping of $\zeta = 0.01$, the structural FRF $H(\omega)$ is calculated using Eq. (3.4) at 500 uniformly-spaced frequencies between 200 Hz and 2000 Hz.

The prior estimate of the force $\hat{\boldsymbol{U}}_p$ is obtained by using the same coupled model described above, but with dry air. The model for the prior uses air with a speed of sound of $c = 343$ m/s, density $\rho = 1.2\text{kg}/\text{m}^3$, and boundary admittance β =100. A harmonic analysis is performed on the dry air system, and the pressure field at the structural plate's surface is saved for use as the pressure prior.

The EI method is used to place sensors on the plate using the numerical structural modes between 200 Hz and 2000 Hz interpolated onto a 6×6 grid of points. Fig. 3.2 shows the grid of candidate locations along with the final sensor configuration at DOFs 14, 15, 17, 20, 23, and 26. Gaussian noise with a signal-to-noise ratio of 40 dB is added to the structural response at the sensor locations to synthesize sensor measurements in the frequency domain. The distributed load is modeled as a set of point loads that coincide with the 6×6 grid of DOFs (B is the 36×36 identity matrix). The 6×6 grid of DOFs corresponds to the DOFs in the experimental system. To study the effects of the choice of force model, we repeat the numerical validation twice: once with the response data generated directly in ANSYS using a fine 19×19 pressure grid, and once with the response data generated by converting the pressure to equivalent forces on a 6×6 grid, and calculating the response using Eq. (3.5). The former case is similar to estimating a true distributed load, while the latter case uses a truth force that can be exactly represented by the chosen force basis. The forces are estimated using the Tikhonov regularization method and converted to equivalent pressures using Eq. 3.22.

The estimated and truth pressures at DOF 16 generated via the fine pressure field are shown in Fig. 3.6a, and the corresponding estimates at the same location for response measurements generated via the coarse pressure field are shown in Fig. 3.6b. For the fine pressure field, the Tikhonov regularization scheme ($e_{u_t} = 49.68\%$, Mean FRAC $= 0.46$) is qualitatively similar to the truth pressure. There are short frequency ranges (e.g., near 800Hz and 1300Hz) where the estimated error diverges from the truth, but the estimate is excellent overall. Despite the force prior having slightly different resonance frequencies than the truth pressure, the peaks in the estimate align very well with the truth peaks. The results are similar using the coarse pressure

field, but the Tikhonov ($e_{u_t} = 42.26\%$, Mean FRAC $= 0.48$) estimate is improved. In this case, the short regions of larger error that are present in the fine pressure grid case now match the truth pressure more closely. This shows that the error in these frequency bands is due to a deficiency in the assumed force basis. However, even for the fairly coarse force basis assumed in this case, the errors that are present in the fine pressure grid case are small compared to the magnitudes of the resonance peaks and appear to be concentrated to short frequency bands. Hence, we can expect to get acceptable results even when using relatively coarse force bases with experimental response measurements to estimate distributed loads.

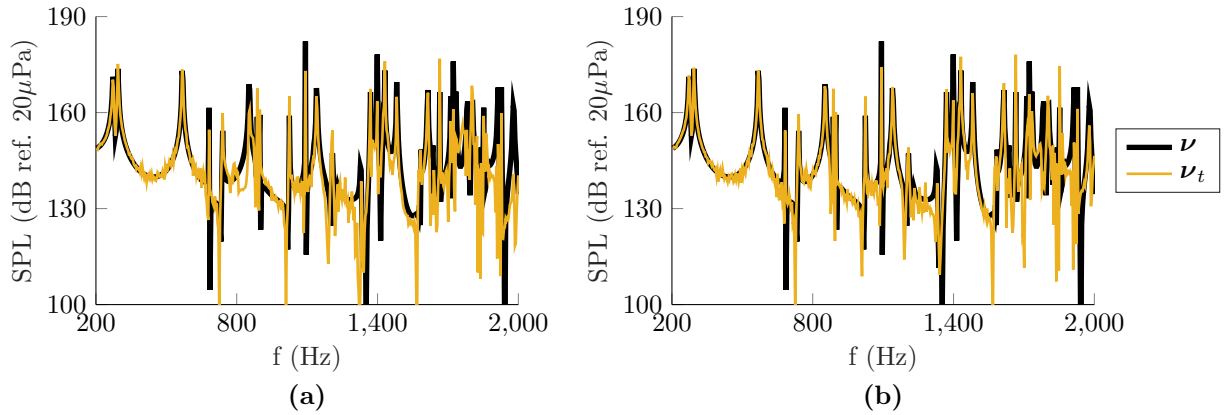

Figure 3.6. Truth and estimated pressure at DOF 16 using measured data generated from (a) forces on a fine 19×19 grid (Mean FRAC $= 0.46$), and (b) forces on a coarse 6×6 grid (Mean FRAC $= 0.48$).

Fig. 3.7 shows the truth spatial pressure distributions at representative frequencies, along with pressure distributions estimated using Tikhonov regularization. The plots show the real part of the pressure estimates (Pa) for response measurements generated using the fine pressure grid, unity normalized to better show the similarities in the spatial distributions. Figs. 3.7a and 3.7c are near resonance and have a very similar shape to the expected mode shapes near these frequencies. Figs. 3.7b and 3.7d lie between resonances and look like a combination of the neighboring mode shapes. For the four frequencies shown, the MAC values using Tikhonov regularization are 0.916, 0.998, 0.915, and 0.826. The estimates are generally similar to the truth distributions at all frequencies.

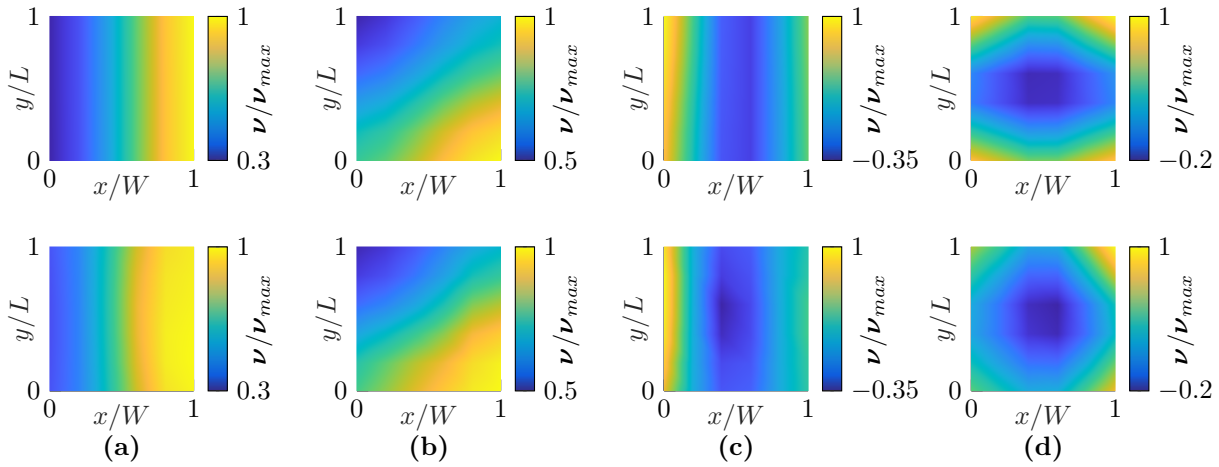

Figure 3.7. (top) Simulated acoustic pressure and (bottom) acoustic pressure estimated using Tikhonov regularization at (a) 745Hz, (b) 945Hz, (c) 1595Hz, and (d) 1750Hz.

3.2.2 Experimental Validation

3.2.2.1 Experimental System

The force estimation methods detailed in Section 3.1 are validated on an experimental acoustic loading configuration. A rectangular aluminum duct of length 61 cm (24 in), width 25.4 cm (10 in), height 20.3 cm (8 in), and wall thickness 0.64 cm (0.25 in) with open ends is placed on a bed of soft foam to isolate it from its surroundings. The duct is seam welded along all edges to maintain rigid boundaries. A speaker (Kicker 46CSC654) is mounted in a hole in a plate with thickness 1.3 cm (0.5 inch), and the plate is clamped to one end of the duct using a flange-collar assembly. Gaskets of the same shape as the flange-plate interface are layered between both the speaker-mounting plate and duct, and the plate and collar to maintain a rigid-wall acoustic boundary at the plate. The experimental duct and speaker plate are shown in Fig. 3.8a. A baseline pressure field is measured using a microphone array. A 1.27 cm (0.5 in) thick aluminum plate with 36 uniformly-spaced threaded holes is clamped to the far end of the duct away from the speaker plate using a similar flange-collar-gasket assembly as the speaker plate. Seven microphones are fitted into threaded plastic housings, which are then threaded into seven of the holes in the plate. The remaining holes are plugged with bolts that pass through thick washers. The microphone and bolt tips sit flush with the interior

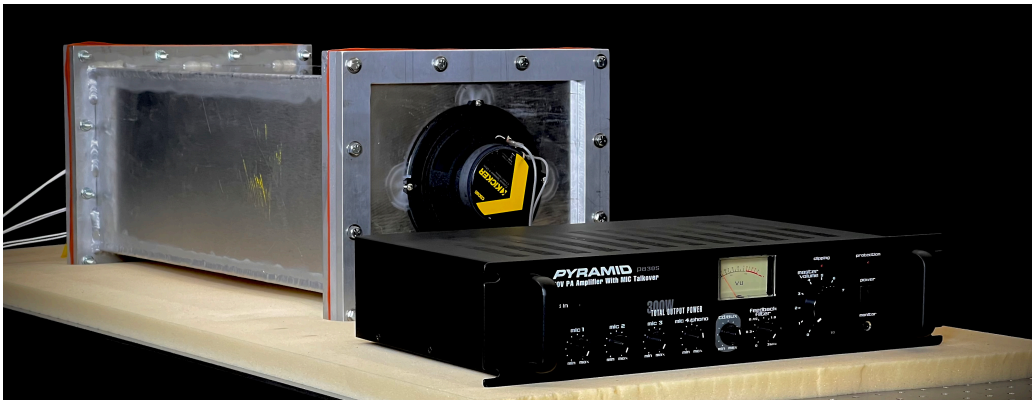

(a)

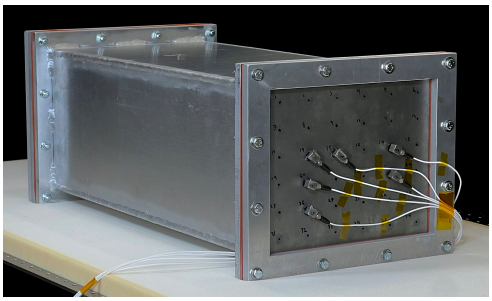

(b)

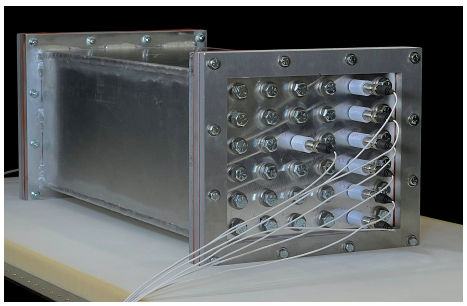

(c)

Figure 3.8. The experimental system showing (a) the duct with mounted speaker and amplifier, (b) the duct assembly with structural transducer plate and accelerometers attached according to the EI results, and (c) the duct assembly with rigid microphone plate and microphones arranged in an example configuration for pressure field measurement.

side of the plate to prevent reflection and refraction off of protruding objects, and all bolts and housings are fitted with o-rings on the exterior side to ensure an airtight seal. A MATLAB script is used to generate and play a linear sine sweep from 200 Hz to 2000 Hz with a linear sweep rate of 12.8 Hz/s through an amplifier (Pyramid PA305) connected to the speaker. The sweep rate is chosen so that the response reaches at least 95% of the steady-state response at all frequencies in the excitation range assuming $\zeta \geq 1\%$ for all modes, per the results in Ref. [86]. The microphones capture the pressures at the measurement locations. Six of the seven microphones are then moved to a different set of six holes, the previous holes are plugged, and the experiment is repeated until the pressure time history at all 36 hole locations has been measured. One microphone is kept near the center of the plate (DOF 15 in Fig. 3.2) during all sine sweeps to ensure the

placement of the microphones does not significantly affect the pressure field. Fig. 3.8c shows the pressure measurement plate attached to the duct and fitted with microphones, housings, and interior bolts.

The microphone array plate is then replaced with a steel transducer plate of thickness 1/16 in (1.6 mm) with no holes, and a roving hammer test is performed to calculate the plate FRF matrix. A 6×6 array of points coincident with the positions in the microphone array is drawn on the plate's surface to maintain consistency between DOFs of the acoustic and structural measurements. Six accelerometers are attached to the plate at a subset of the drawn points using stiff wax, and a calibrated hammer with a steel tip is used to tap the plate at all points. The FRF of the plate between every excitation and response point on the 6×6 grid is calculated as the ratio of the Fourier transform (DFT) of the accelerometer response to the DFT of the hammer impulse. The FRF functions are refined by using a local modeling technique to reduce noise [87]. The accelerometers are moved around the plate and the experiment is repeated until the entire FRF matrix is populated.

The acoustic excitation experiment is then performed. Six accelerometers are attached to the plate using wax according to the results of the EI method using the numerical mode shapes of the transducer plate between 200 Hz and 2000 Hz and sampled at the experimental DOFs. (Fig. 3.2). A MATLAB script is used to generate and play a linear sine sweep from 200 Hz to 2000 Hz with a rate of 3.20 Hz/s through an amplifier connected to the speaker. The sweep rate is chosen so that the response reaches at least 99% of the steady-state response at all frequencies in the excitation range assuming $\zeta \geq 1\%$ for all modes [86]. Note that the sine sweep for the acoustic excitation experiment has a slower rate than the sweep for the acoustic pressure measurement experiment because small errors in the response measurements can yield large errors during the system inversion process, but the difference between the measured pressure field using a 3.20 Hz/s or 12.8 Hz/s sweep would be negligible. The transducer plate fitted with accelerometers according to the results of the EI placement method is shown in Fig. 3.8b.

The sine sweep data are processed to capture the steady-state magnitude and relative phase between simultaneous pressure or acceleration measurements. The time series are first trimmed to the duration of the sine sweep. The time series are divided into 0.1 s windows that are linearly mapped onto frequency bins from 200 Hz to 2000 Hz. For each window, the first sensor is arbitrarily assumed to have a phase angle of zero, and the locations of all peaks in the first sensor's time history are detected. The wavelength is estimated as the average distance between consecutive peaks. The peaks of each other sensor are then

detected, and the phase angle is estimated as the ratio of the mean distance between peaks in each sensor and the first sensor, and the wavelength. That is,

$$\phi_j = 2\pi \frac{\sum_1^{N_p} t_{pj} - t_{p1}}{N_p l}, \tag{3.25}$$

where ϕ_j is the phase angle of sensor j relative to the first sensor, N_p is the number of detected peaks, t_{pj} are the times at which the peaks in sensor j occur, and l is the wavelength. The complex-valued steady-state response amplitude for each sensor in each frequency bin is then calculated as

$$\hat{P}_j = \bar{P}_j(\cos(\phi_j) + i\sin(\phi_j)), \tag{3.26}$$

where $\bar{P}_j$ is the average values of the peaks in sensor j. Note that this method only preserves phase information within the pressure and acceleration datasets but does not capture phase information between data sets. The steady state response at frequencies between those explicitly calculated via the above method is estimated via linear interpolation.

A force prior is calculated using finite element analysis in the ANSYS model. The duct is modeled as a rigid-walled duct with the same dimensions as the real duct. All nodes on the wall corresponding to the speaker plate are assigned a "flow" boundary condition with a unit magnitude, which corresponds to a piston driving the acoustic fluid. A harmonic analysis is performed between 200 Hz and 2000 Hz, and the resulting pressure field on the rigid wall corresponding to the transducer plate is saved. The force prior is generated by mapping the pressure values from the FEA model at the desired frequencies onto the locations of the forces to be estimated. Notice that the FEA model used to create the force prior for this experimental case is simpler than the model used in the numerical validation. The model used in the numerical validation is a two-way coupled acoustic-structural model with the speaker modeled over a portion of the speaker plate. We use a simple, purely acoustic model here to create the prior for the experimental case to demonstrate that the prior need not be a perfect reflection of reality in order to accurately estimate the real pressure distribution. Note that this experiment represents an example of a case where classical generalized regularization (Eq. (3.17)) would be unsuitable since the form of the pressure distribution can be easily estimated via FEA, but the speaker volume and corresponding pressure magnitude cannot be easily estimated without directly measuring the pressure field.

3.2.2.2 Experimental Results

The estimated pressure at DOF 16 on the plate using our generalized Tikhonov regularization scheme is shown in Fig. 3.9. For the experimental configuration, $n_s = n_f = 6$. Overall the Tikhonov estimates $\boldsymbol{\nu}_t$ ($err_{\boldsymbol{\nu}_t} = 52.75\%$, Mean FRAC $= 0.59$) are similar to the numerical results shown in Fig. 3.6. The estimates also match the truth pressure distribution much more closely than the prior pressure distribution $\boldsymbol{\nu}_p$ (Mean FRAC $= 0.02$), which implies that the regularization scheme correctly incorporates measurements to refine the prior estimate. The scaling of the prior is arbitrary for force estimation purposes, but is scaled to match the truth pressure at 200Hz for visualization. The estimated resonance peaks occur at similar frequencies and have similar quality to the measured peaks. The estimated magnitudes of the peaks up to around 1000 Hz also tend to match the truth magnitudes. The lowest-frequency measured peak at approximately 280 Hz does not match the estimated magnitude because the microphones begin clipping at approximately 128 dB. However, the accuracy of the other peaks up to 1000 Hz suggests that it may be possible to use system inversion methods to reconstruct high-magnitude loads that would otherwise require specialized sensors using common acceleration sensors. Above 1000 Hz, the resonance locations are still accurately estimated, but the magnitudes are frequently underestimated. We believe that this degradation in the estimation quality is due to a degradation of quality in the experimental structural FRFs at high frequencies. Due to the relatively compliant structure, the hammer taps excite the higher structural modes significantly less than the lower frequency modes, leading to a decrease in FRF quality with frequency. Nonetheless, the overall reconstruction quality across the entire frequency range from 200 Hz to 2000 Hz is adequate to understand the loading environment.

The unity-normalized measured spatial pressure distribution at a few representative frequencies, along with the normalized real part of the pressure distribution estimated using our new Tikhonov regularization, are shown in Fig. 3.10. For the four frequencies shown, the MAC values using Tikhonov regularization are 0.947, 0.379, 0.644, and 0.032. The Tikhonov regularization method yields adequate spatial reconstructions near resonance (Fig. 3.10a and c). The reconstruction quality above 1000 Hz – where the estimated peak amplitude is underestimated – is lower near resonance (Fig. 3.10c), but the estimates are still visually similar to the measured distribution. The spatial reconstructions resemble the measured pressure field far from resonance as well (Fig. 3.10b), but the results are not as high quality as the equivalent numerical results in Fig. 3.7. We believe that the reduced quality of these results may be due to a higher influence of measurement

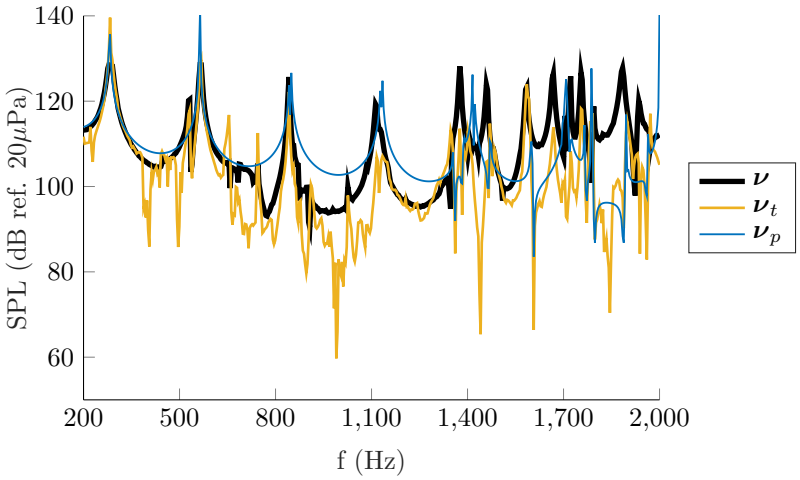

Figure 3.9. Measured acoustic pressure, pressure estimated from measured response data with $n_s = 6$, and pressure prior at DOF 16.

bias and noise on the low response amplitudes that occur off-resonance. At high frequency and off resonance (Fig. 3.10d), the lower signal-to-noise ratio and poorer FRF quality compound to yield force estimates that do not visually resemble the truth.

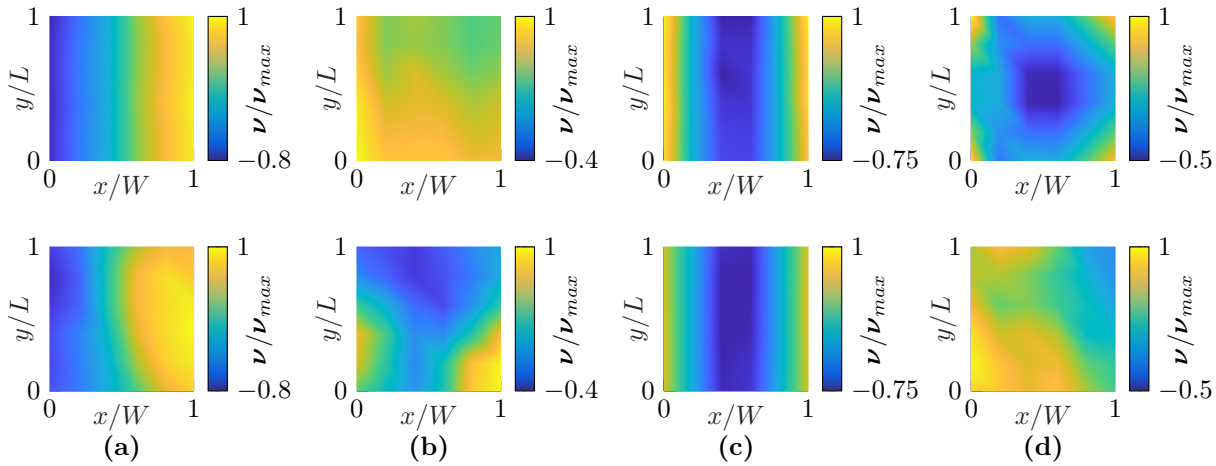

Figure 3.10. (top) Measured acoustic pressure and (bottom) acoustic pressure estimated using Tikhonov regularization at (a) 745Hz, (b) 945Hz, (c) 1595Hz, and (d) 1750Hz.

3.3 Conclusions

Distributed loads are common in engineered systems, but these loads are often difficult or impossible to measure directly. However, it is usually feasible to measure the system response at a relatively small number of locations. It is possible in principle to estimate the distributed loads from response measurements, but the number of sensors required to render a well-posed problem is often infeasible. The present work adapts a novel Bayesian spatial prior term for use with a classical Tikhonov regularization scheme. Results show that the new regularization term is able to estimate complicated distributed pressure fields from a small number of measurements with acceptable accuracy. Our numerical results are validated with experimental data taken on a steel plate coupled to an acoustic duct. We expect the results of the present work to help bridge the gap between input estimation approaches using classical regularization and Bayesian inference.

While the results shown here are promising, future work is still needed. The Tikhonov regularization approach proposed here is only applicable to inversion methods based on direct matrix inversion. Hence, the method in its current form is inapplicable to nonlinear systems. A nonlinear analogue could be derived by replacing the force covariance matrix with a function representation, replacing the Cholesky decomposition

with a square root operation, and solving the resulting problem via direct optimization. A nonlinear form of the method presented here would make the method suitable to a much wider variety of problems.

The smoothing parameter s is also difficult to estimate without performing a full parameter study. The optimal choice of the parameter depends on the form of the truth force, which itself is typically only known up to the form of the prior. Further, the quality of the estimate typically has a complicated relationship with the value of s, making an optimal choice of s difficult. While an estimate based on trial and error is often sufficient, a method of choosing s automatically would make the prior selection process simpler and more robust.

Chapter 4

Dynamic Moving Force Estimation

Estimating the dynamic forces on a structure from sparse response measurements is a well-known inverse problem. The problem is typically ill-conditioned, and requires regularization to obtain a stable solution. If the force is distributed or moves with time, standard regularization goals such as small force magnitudes or sparse forces are often insufficient to obtain an acceptable force estimate. In such cases, additional information about the force is required to constrain the estimates to reasonable values. This chapter proposes a moving force estimation technique based on the augmented Kalman filter (AKF) that uses a convecting force model to include additional information on the expected motion of the force. The force model does not assume the truth force consists of point loads, so the method is suitable for traveling point loads and convecting distributed loads such as those due to flowing fluids. The force model in combination with regularization terms from pseudo measurements and the Kalman filter force covariance parameter yields estimates that are very close to the specified traveling loads. Results show that the AKF with convecting force model yields significantly improved traveling load estimates when compared to the standard AKF, and comparable results to those from modern methods for traveling load estimation. Furthermore, the method is robust to errors in the assumed force velocity because of the statistical nature of the Kalman filter.

4.1 Methods

4.1.1 Structural Model

The equations of motion for a general linear elastic structure may be written as

$$\ddot{\boldsymbol{q}} + C\dot{\boldsymbol{q}} + K\boldsymbol{q} = \Phi^T F\boldsymbol{u} + \boldsymbol{w}, \tag{4.1}$$

where $\boldsymbol{q}$ is a vector of N generalized coordinates, C is the modal damping matrix, K is the modal stiffness matrix, Φ is the mode shape matrix, F is a matrix that maps forces to the appropriate degrees of freedom (DOFs) in physical coordinates, $\boldsymbol{u}$ is a vector of forces, and $\boldsymbol{w}$ is a random vector with the model covariance matrix Q_w. The model covariance Q_w represents the amount of uncertainty in the model. When a force is assumed at every DOF, F becomes the identity. Equation (4.1) may be rewritten in first-order form as

$$\begin{Bmatrix} \dot{\boldsymbol{q}} \\ \ddot{\boldsymbol{q}} \end{Bmatrix} = \begin{bmatrix} 0 & I \\ -K & -C \end{bmatrix} \begin{Bmatrix} \boldsymbol{q} \\ \dot{\boldsymbol{q}} \end{Bmatrix} + \begin{bmatrix} 0 \\ \Phi^T F \end{bmatrix} \boldsymbol{u} + \begin{Bmatrix} 0 \\ \boldsymbol{w} \end{Bmatrix}, \tag{4.2}$$

where I is the identity. Instead of treating the force as a known input, $\boldsymbol{u}$ can be appended to the state vector and modeled as an unknown, which requires a corresponding force model in the state transition matrix. When no prior information is available, a zero-order hold model, which assumes the force is static apart from uncertainty, is typically used. If the force is known to convect at nearly constant velocity, a convecting force model may be used instead. However, this model cannot be incorporated directly into the continuous-time Kalman filter. We therefore begin by discretizing the system using the zero-order hold model, and then substitute the discrete force model with the convecting version. The zero-order hold model is given by

$$\dot{\boldsymbol{u}} = 0 + \boldsymbol{z}, \tag{4.3}$$

where $\boldsymbol{z}$ is a random noise vector with covariance Q_z. Equation (4.2) can now be rewritten with the force augmented to the state,

$$\dot{\hat{\boldsymbol{q}}} = A\hat{\boldsymbol{q}} + G \begin{Bmatrix} 0 \\ \boldsymbol{w} \\ \boldsymbol{z} \end{Bmatrix}, \tag{4.4}$$

where

$$\hat{\boldsymbol{q}} = \begin{Bmatrix} \boldsymbol{q} \\ \dot{\boldsymbol{q}} \\ \boldsymbol{u} \end{Bmatrix}, \tag{4.5}$$

$$A = \begin{bmatrix} 0 & I & 0 \\ -K & -C & \Phi^T F \\ 0 & 0 & 0 \end{bmatrix}, \tag{4.6}$$

and

$$G = \begin{bmatrix} 0 & 0 & 0 \\ 0 & I & 0 \\ 0 & 0 & I \end{bmatrix}. \tag{4.7}$$

The noise vector covariance matrix for this system may be written

$$Q = \begin{bmatrix} 0 & 0 & 0 \\ 0 & Q_w & 0 \\ 0 & 0 & Q_z \end{bmatrix}. \tag{4.8}$$

During numerical simulation, the equations of motion are sampled at regular time intervals of duration Δt. Equation (4.4) must be cast as a discrete-time recursive equation where the state at time step $k+1$ may be calculated from the state at time step k

$$\hat{\boldsymbol{q}}_{k+1} = A^* \hat{\boldsymbol{q}}_k + G^* \begin{Bmatrix} 0 \\ \boldsymbol{w} \\ \boldsymbol{z} \end{Bmatrix}_k, \tag{4.9}$$

where

$$A^* = e^{A\Delta t}, G^* = \left[\int_0^{\Delta t} e^{At} dt \right] G. \tag{4.10}$$

In practice, the matrices A^* and G^* are converted from their continuous time counterparts numerically, using, for example, the Matlab function *c2d*. The discretized augmented model covariance matrix is

$$Q^* = G^* Q G^{*T}. \tag{4.11}$$

4.1.2 Measurement Equation

System measurements via sensors are modeled as a linear combination of the state variables.

$$\boldsymbol{y} = H\hat{\boldsymbol{q}} + \boldsymbol{v}, \tag{4.12}$$

where $\boldsymbol{y}$ is the vector of sensor measurements, H is a measurement matrix that transforms the state vector into the measurement vector, and $\boldsymbol{v}$ is a random vector of zero mean with a covariance matrix R representing sensor noise. Displacement measurements are used in the present work, but formulations for H exist for other types of measurement as well (*e.g.*, accelerometers and strain gauges). If we assume that the measurements are not correlated, R is a diagonal matrix.

The measurement matrix H includes a map from the state vector in physical coordinates to the measurement vector, and a map from modal coordinates to physical coordinates. The physical state $\hat{\boldsymbol{x}}$ can be

mapped on the measurements using the physical measurement matrix H_x

$$\boldsymbol{y} = H_x \hat{\boldsymbol{x}} + \boldsymbol{v}, \tag{4.13}$$

where $\hat{\boldsymbol{x}} = [\boldsymbol{x}, \dot{\boldsymbol{x}}, \boldsymbol{u}]^T$ is a physical state vector composed of the physical displacement $\boldsymbol{x}$, physical velocity $\dot{\boldsymbol{x}}$, and force $\boldsymbol{u}$. The augmented state vector in physical coordinates is related to the modal augmented state vector by

$$\hat{\boldsymbol{x}} = \begin{bmatrix} \Phi & 0 & 0 \\ 0 & \Phi & 0 \\ 0 & 0 & I \end{bmatrix} \hat{\boldsymbol{q}} = \tilde{\Phi} \hat{\boldsymbol{q}} \tag{4.14}$$

For displacement sensors, H_x is a selection matrix with rows of zeros except at indices corresponding to the measured displacement DOFs.Alternatively, H_x may be thought of as a reduced identity matrix where only the rows corresponding to the measured DOFs are retained. Substituting Eq. (4.14) into Eq. (4.13), we arrive at an expression for H,

$$H = H_x \tilde{\Phi}. \tag{4.15}$$

4.1.3 Convecting Force Model

If the force moves across the spatial domain at a nearly constant velocity ν, the zero-order hold model can be replaced with a convecting force model. This assumption may be appropriate for a vehicle traveling across a bridge or for vortex-induced forces convecting along an aircraft wing in a uniform freestream. The convecting force model assumes that the force travels in the flow direction by a distance $\nu \Delta t$ every timestep. That is,

$$\boldsymbol{u}_{k+1}^{\xi+\nu\Delta t} = \boldsymbol{u}_k^{\xi} + \boldsymbol{z}, \tag{4.16}$$

where ξ is a physical location along the flow direction, and $\boldsymbol{u}^{\xi}$ is the force at ξ. This model is applied to every force at least $\nu \Delta t$ from the leading edge of the domain. However, near the leading edge, there is no upstream value to convect from, so the model must be modified. At these locations, the force is instead assumed to originate from the leading edge itself, i.e.,

$$\boldsymbol{u}_{k+1}^{\xi} = \boldsymbol{u}_k^{0} + \boldsymbol{z}, \tag{4.17}$$

where $\xi < \nu \Delta t$ is a distance less than the convection distance from the leading edge of the domain.

It is also possible to introduce a decay term into the force model. The decay term models situations where the forces are expected to decay exponentially as they convect across the domain. If a decay term is included, Eqs. (4.16) and (4.17) respectively become

$$\boldsymbol{u}_{k+1}^{\xi+\nu\Delta t} = (1-\alpha\Delta t)\boldsymbol{u}_k^{\xi} + \boldsymbol{z}, \tag{4.18}$$

$$\boldsymbol{u}_{k+1}^{\xi} = (1-\alpha\Delta t)\boldsymbol{u}_k^{0} + \boldsymbol{z}, \tag{4.19}$$

where $0 \leq \alpha \leq 1$ is a constant that controls the rate of decay. When $\alpha = 0$, Eqs. (4.18) and (4.19) become Eqs. (4.16) and (4.17) respectively. When $\alpha > 0$, the force is assumed to decay by approximately $\alpha \boldsymbol{u}_k$ per second.

These equations replace the standard zero-order hold equations in Eq. (4.9). Rows in the force model section of A^* are replaced with Eqs. (4.16) and (4.17). If ν is constant, A^* is a static matrix. Otherwise, A^* must be re-calculated at every timestep. The convecting force equations cannot be incorporated into the continuous state transition matrix Eq. (4.4) since the spatial derivative of the force cannot be easily related to the time derivative. Instead, the standard zero-order hold model is used to obtain a discrete-time form of the equations of motion that is later replaced with the convecting force model.

4.1.4 Kalman Filter

The Kalman Filter consists of a time update step, during which the system equations of motion Eq. (4.9) are used to predict the state in the next time step, and a measurement update step, during which the measured data are used to correct the prediction. The Kalman gain matrix K_g decides how much correction to perform at each time step based on the covariance of the estimation error P. The algorithm may be written as follows:

Time update:

$$\hat{\boldsymbol{q}}_k^- = A^* \hat{\boldsymbol{q}}_{k-1}^+, \tag{4.20}$$

$$P_k^- = A^* P_{k-1}^+ A^{*T} + Q^*, \tag{4.21}$$

Measurement update:

$$K_g = P_k^- H^T \left(H P_k^- H^T + R\right)^{-1}, \tag{4.22}$$

$$\hat{\boldsymbol{q}}_k^+ = \hat{\boldsymbol{q}}_k^- + K_g \left(\boldsymbol{y} - H\hat{\boldsymbol{q}}_k^-\right), \tag{4.23}$$

$$P_k^+ = (I - K_g H)\, P_k^-, \tag{4.24}$$

where the $-$ and $+$ superscripts represent quantities before and after measurement update, the subscript k represents the timestep, and P is the covariance of the estimation error.

4.1.5 ℓ_1 Regularization

We implement ℓ_1 regularization via the method of Ref. [70] to encourage sparsity in the estimated forces. The Kalman filter is an optimal state estimator that provides a minimum mean square error solution between the estimated state $\hat{\boldsymbol{q}}$ and the true state $\bar{\boldsymbol{q}}$,

$$\hat{\boldsymbol{q}} = \arg\min_{\hat{\boldsymbol{q}}}(||\hat{\boldsymbol{q}} - \bar{\boldsymbol{q}}||_2^2). \tag{4.25}$$

The force portion of this equivalent optimization formulation can be regularized by introducing a penalty term,

$$\hat{\boldsymbol{q}} = \arg\min_{\hat{\boldsymbol{q}}}(||\hat{\boldsymbol{q}} - \bar{\boldsymbol{q}}||_2^2 + \gamma||\boldsymbol{u}||_1), \tag{4.26}$$

where γ is a regularization parameter that controls the strength of the regularization, and $||\boldsymbol{u}||_1$ is the ℓ_1 norm of the force portion of $\hat{\boldsymbol{q}}$, which is simply the sum of the absolute values of the components of $\boldsymbol{u}$. Equation (4.26) can be rewritten as an equivalent constrained optimization problem,

$$\hat{\boldsymbol{q}} = \arg\min_{\hat{\boldsymbol{q}}}(||\hat{\boldsymbol{q}} - \bar{\boldsymbol{q}}||_2^2), \quad \text{s.t.}||\boldsymbol{u}||_1 < \epsilon_\gamma, \tag{4.27}$$

where ϵ_γ is a threshold that takes the place of the regularization parameter γ. The solution of Eq. (4.27) lies on the boundary $||\boldsymbol{u}||_1 - \epsilon_\gamma = 0$ for sufficiently small ϵ_γ. We can rewrite this boundary as a pseudo-measurement, which can be directly incorporated into the measurement update portion of the Kalman filter.

$$0 = \bar{H}\hat{\boldsymbol{q}}_k - \epsilon_\gamma, \tag{4.28}$$

where $\bar{H}(\boldsymbol{u}_k) = [0_{1\times 2N}, \text{sign}(\boldsymbol{u}_k)]$ is the pseudo-measurement matrix that takes the form of zeros in the indices corresponding to the modal displacements and velocities, and the sign of each force in the corresponding force indices. The threshold parameter ϵ_γ can now be treated as a random variable with variance R_γ. A small value of R_γ corresponds to a large regularization parameter γ, and results in a strong ℓ_1 regularization.

The pseudo-measurement equation can be appended directly to the measurement equation Eq. (4.13) and incorporated into the standard Kalman filter, Eqs. (4.20)-(4.24). Alternatively, a second measurement update step following the first measurement update can be iterated using just the pseudo-measurement to strengthen the regularization effect at each timestep. In this case, the following equations are repeated N_τ times, where N_τ is chosen to balance computational complexity with the completeness of the regularization process. The regularized solution typically converges after approximately $N_\tau = 10$ iterations [70].

Pseudo measurement update:

$$K_g = P_k^+ \bar{H}^T(\boldsymbol{u}_k) \left(\bar{H}(\boldsymbol{u}_k) P_k^+ \bar{H}^T(\boldsymbol{u}_k) + R_\gamma\right)^{-1}, \tag{4.29}$$

$$\hat{\boldsymbol{q}}_k^+ = \left(I - K_g \bar{H}\right) \hat{\boldsymbol{q}}_k^+, \tag{4.30}$$

$$P_k^+ = \left(I - K_g \bar{H}\right) P_k^+, \tag{4.31}$$

4.1.6 Error Quantification

The force predicted using the AKF with or without the convecting force model tends to have a different magnitude and covers a different sized patch of the beam than the truth force. Since the beam's response is similar whether a distributed force with a small magnitude or a concentrated force with a large magnitude is applied, it is difficult for the AKF method to determine the correct magnitude and distribution of the force without prior knowledge of one or the other. However, engineers are often only concerned with the total force and center location of a locally distributed load such as the force of a large vehicle on a bridge or the resultant force induced by a small vortex as it convects across a structure.

In the present work, we quantify how well the force estimates match reality by integrating the force estimate over a portion of the beam's span. The integrated force as a function of time is given by

$$\hat{u}_{r\%}(t) = \int_l^L \boldsymbol{u} dl, \tag{4.32}$$

where $r = l/L$ is a fraction of the length of the beam, l is a distance along the beam, and L is the total length of the beam. For example, $\hat{u}_{70\%}$ represents the integrated force from $r = 0.7$ to 1. For validation purposes, the resulting values of $\hat{u}_{r\%}$ can then be normalized by the largest integrated truth force in the time range of

interest so that the force estimate can be easily compared to the known truth. We define

$$\bar{u}_{r\%} = \hat{u}_{r\%}/\hat{u}_{\max}, \tag{4.33}$$

where $\bar{u}_{r\%}$ is the normalized integrated force, and $\hat{u}_{\max}$ is the largest value of $\hat{u}_{r\%}$ in the time range of interest.

To directly compare the error between the truth and approximated integrated force, we define a mean squared error metric,

$$\varepsilon_{r\%} = 100 \times \frac{|\hat{u}_{r\%,t} - \hat{u}_{r\%,a}|_2^2}{|\hat{u}_{r\%,t}|_2^2} \tag{4.34}$$

where $\hat{u}_{r\%,t}$ and $\hat{u}_{r\%,a}$ are the integrated truth and approximated forces over the last $r\%$ of the beam, respectively. The 2-norms are taken over the vector of integrated force values at all timesteps.

4.1.7 Parameter Selection

In addition to the physical parameters that describe the system parameters and force dynamics, the method described in the preceding sections depends on several user-specified parameters including the model covariance matrix Q_w, the force covariance matrix Q_z, the measurement covariance R and the ℓ_1 pseudo-measurement variance R_γ. The parameters in the present work are selected by trial and error, but this section describes how parameters might be chosen systematically.

The measurement covariance matrix R can typically be measured experimentally. It represents the covariance of the noise present in the measurements. The noise level can be calculated by measuring a time series with only noise (no response), and calculating the variance of this time series. If all measurements from all sensors are not correlated, R is a diagonal matrix with R_{jj} equal to the noise variance of the sensor j.

The model covariance matrix Q_w represents the level of discrepancy between the structural model and the physical system, and is more difficult to quantify than R. When measurements are synthesized using the same model for both the forward and inverse problems, $Q_w = 0$. Otherwise, Q_w is often taken as a diagonal matrix with entries on the order of the squared maximum expected state values [65]. A rough estimate of Q_w is generally adequate, as the quality of the force estimate is usually not very sensitive to the choice of Q_w.

The force covariance matrix Q_z acts as an ℓ_2 regularization parameter that directly controls how much the force magnitudes are allowed to change each timestep. A large Q_z allows the forces to change quickly, which can result in the response portion of the state overfitting to the measurements and a nonsmooth force estimate that poorly matches the true force. A small value of Q_z does not allow the forces to change quickly enough to match the true force, resulting in an overly smooth force estimate and a poor match between the state and the measurements. The unknown force magnitudes are typically assumed to be uncorrelated and have similar dynamic characteristics, so Q_z is usually assumed to be a scaled identity matrix $Q_z = \beta I$, where β is a scaling parameter. The well-known L-curve method can then be used to find the optimal value of β.

The pseudo measurement variance R_γ acts as an ℓ_1 regularization parameter, and is used in tandem with Q_z to control the characteristics of the force estimate. A small R_γ yields a strong ℓ_1 regularization and a sparse force estimate [70]. The R_γ parameter can also be chosen using the L-curve method. However, the L-curve method in its classical form is only used to estimate one regularization parameter. In the presented case where $Q_z = \beta I$ and R_γ both must be specified, it should be possible to construct a multidimensional L-hypersurface where the fitting norm and regularization norm are calculated for every combination of β and R_γ. The optimal values of both parameters could then be calculated by choosing a configuration that balances the regularization and the fitting errors. However, this method would be computationally intensive to implement.

4.2 Results

The AKF method is verified numerically on the cantilevered beam system shown in Fig. 4.1. The beam is 12.7 cm long and made of steel with a Young's modulus of 200 GPa, Shear modulus of 79.3 GPa, Poisson's ratio of 0.3, and density of 7850 kg/m^3. The beam's cross section has an area moment of inertia of 4.34E-11 m^4. The beam is modeled using 1000 Timoshenko beam elements implemented in the commercial finite element package ANSYS, wherein the mode shape matrix, ϕ, is calculated.

The beam is subject to a train of distributed forces. The forces take the spatial form of Gaussian normal distributions with peak magnitudes $\kappa_i(t)$ and mean locations $\lambda_i(t)$. The distributed force on the beam F_x is

given by

$$F_x(l,t) = \sum_{i=1}^{N_f} \kappa_i(t) \exp\left(\frac{-(l-\lambda_i(t))^2}{2\sigma^2}\right), \tag{4.35}$$

where N_f is the number of pulses, and σ is the standard deviation. The center point of the pulse is controlled by λ_i, κ_i controls the magnitude of the pulse, and σ controls the width of the pulse. The values of these parameters change depending on the experiment. The values of λ_i, κ_i, and σ for each case are given in Table 4.1. The velocity of the pulses is defined by the total number of pulses that travel across the beam N_f, the number of pulses that exist on the beam simultaneously N_s, and the simulation duration T. These parameters can be converted to a truth pulse velocity using

$$\nu_t = \frac{N_f L}{N_s T}. \tag{4.36}$$

For all cases studied here, $T = 1$ s, $N_f = 6$, and $N_s = 2$. The "Varying Magnitude" and "Varying Spacing" cases contain parameters $\boldsymbol{A}$ = [20, -30, 10, 20, -5, 40] and $\boldsymbol{B}$ = [0.005, -0.014, 0.032, 0.013, 0.022, 0.026] that explicitly dictate the magnitude and spacing of each force, respectively.

Response measurements are synthesized by simulating the system response to the applied force. The system is assumed to start from rest, and Eq. (4.9) is used to simulate the displacement response in discrete time. When simulating the forward problem, F_x is assigned to every DOF at every timestep by evaluating F_x at the position of each DOF l. The structural model is truncated to the first 25 modes for the forward problem. The displacement response is converted to displacement measurements by sampling the response at the measurement locations and adding Gaussian noise with a signal-to-noise ratio (SNR) of 40dB. Measurements are taken at 50 uniformly spaced locations along the beam's length. This number of measurement points would be infeasible using traditional sensors, but is practical using modern laser displacement sensor systems.

The synthesized measurements are then passed to the force estimation process. The same nominal structural model is used for the forward and inverse processes, but the model for inversion is truncated to 10 modes instead of the 25 used for the forward model. A vertical force with independent magnitude is assumed at each DOF on the beam, so F is the identity, and $\boldsymbol{u}$ has 1000 elements. Fewer modes are used in the inverse model to emulate the truncation error that would be expected when modeling a real system. The same parameter values are used for most cases. The quality of the estimation is insensitive to the exact

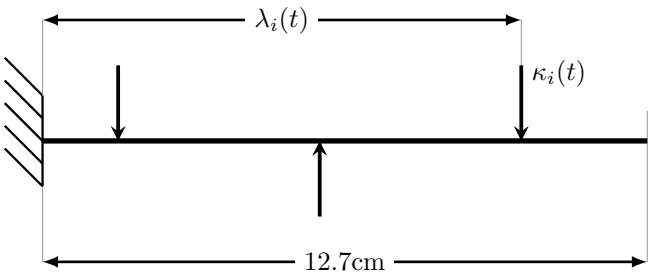

Figure 4.1. Schematic of the cantilevered beam system with alternating pulse train forcing. Forces convect from left to right (λ_i monotonically increases for all cases)

values of Q_w and R, so small values are arbitrarily chosen. The model covariance matrix Q_w is a multiple of the identity matrix with values approximately equal to 10% of the square of the largest value in the state estimated by inverting the measurement matrix. That is,

$$Q_{w,ii} = 0.1\text{max}(|H^{\dagger}y|)^2, \tag{4.37}$$

where † indicates the pseudo-inverse. A nonzero value of Q_w is chosen to account for the truncation error, even though a value of zero would be appropriate if the forward and inverse models are identical. The measurements are assumed to be uncorrelated, so R is also assumed to be a diagonal matrix with values equal to 5% of the square of the largest measurement.

The values of Q_z and R_γ are chosen by trial and error. The force estimates are insensitive to changes in these parameters within an order of magnitude, so the parameters are tuned to an acceptable order of magnitude. The forces at every DOF are assumed to be uncorrelated and to change at approximately the same rate, so Q_z is a diagonal matrix with 1E4 along the diagonal while R_γ is assigned a value of 1E6. In the "Larger Varience" case, no ℓ_1 regularization is used because the force is distributed enough that a sparsity constraint is unnecessary.

4.2.1 AKF Without convecting Force Model

We first evaluate the performance of the force estimation via the standard AKF with no convecting force model and no sparsity constraint. Fig. 4.2 shows a surface plot of the standard AKF results along with the corresponding force integral plot over the trailing 30% of the beam. For this case, $\varepsilon_{70\%} = 16.37\%$. The

Case	λ_i	κ_i	σ
Baseline	$-(i-1)\frac{L}{N_s}+\nu t$	$20(-1+2(i \bmod 2))$	0.001
Varying Magnitude	$-(i-1)\frac{L}{N_s}+\nu t$	$A_i(-1+2(i \bmod 2))$	0.001
Varying Spacing	$-(i-1)\frac{L}{N_s}+\nu t+B_i$	$20(-1+2(i \bmod 2))$	0.001
Larger Variance	$-(i-1)\frac{L}{N_s}+\nu t$	$20(-1+2(i \bmod 2))$	0.01
Decaying	$-(i-1)\frac{L}{N_s}+\nu t$	$20\exp(-10\lambda_i(t))(-1+2(i \bmod 2))$	0.001

Table 4.1. Equations for λ_i, κ_i, and σ for various cases. Here, mod is the modulo operator.

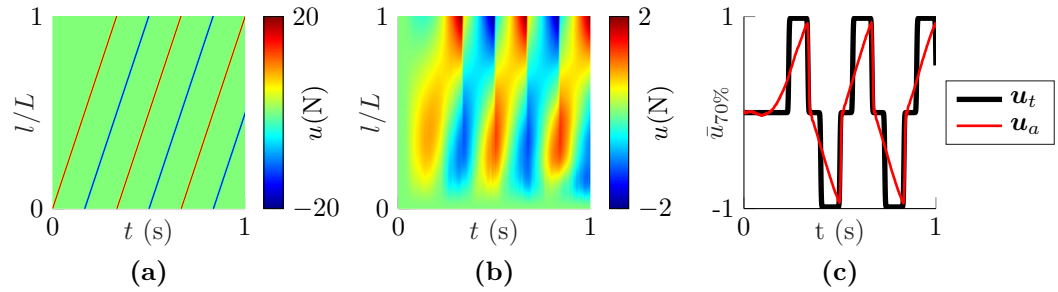

Figure 4.2. (a) Truth force, (b) force estimated using the AKF with a zero-order hold force model, and (c) force integral over the last 30% of the beam. $\varepsilon_{70\%} = 16.37\%$.

force integrals for all cases are taken over the last 30% of the beam to measure each pulse individually, since this range can capture an entire single distributed pulse without also measuring upsteam pulses. The AKF force estimate is much more spread out in space and time, and has a much smaller magnitude than the truth force. However, the force integral shows that the total force is similar for both cases near the beam tip. The state response at the beam tip also matches the input measurements very well as shown in Fig. 4.3, so the estimated force affects the structure similarly to the truth force. No force is estimated near the beam's base at all timesteps because forces near the fixed boundary yield very little response, so the AKF has difficulty inferring force in this region.

Notice also that the middle point of each pulse seems to rest at one of two positions near the midpoint and tip of the beam. The standard zero-order hold force model favors force configurations that are similar to the previous force estimate, while still yielding a response similar to the measurements. Hence, this model tends to yield force estimates that stay in the same location for as long as possible. The holding location seems to depend on the number of modes retained in the inverse structural model as shown in Fig. 4.4 where the ten-mode case is the same as the case presented in Fig 4.2. We suspect that the forces tend to hold at

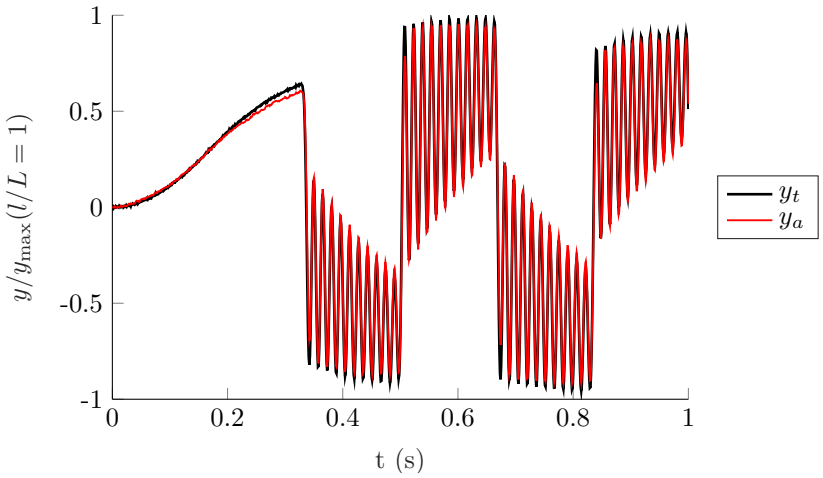

Figure 4.3. Measured truth response (black) and response estimated by the standard AKF (blue) at the beam tip.

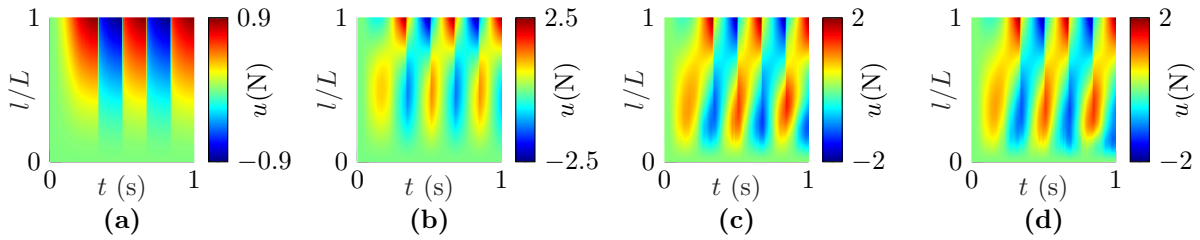

Figure 4.4. Force distribution estimated by the standard AKF using an inverse model truncated to (a) 1 mode, (b) 2 modes, (c) 5 modes, (d) 10 modes.

the anti-nodes of the set of included modes, since these are locations where the force can maximally affect the response without changing locations. When one mode is used, the force is always located near the beam tip coincident with the sole anti-node. When two modes are used, the holding location sits near either the midpoint or the tip, and has a low magnitude where it transitions between these points. With more than five modes, the force still holds at the tip, but the midpoint location shifts slightly toward the root, and the magnitude in the transition region is comparable to the magnitude at the peak.

4.2.2 AKF With Convecting Force Model

We now evaluate the performance of the AKF with both the convecting force model and ℓ_1 regularization via pseudo-measurements. Figure 4.5 shows the results using the AKF with the convecting force model and ℓ_1 regularization for different variations of the pulse train loading configuration. The surface plots in this

figure are all normalized by the largest force in the domain $u_{\max}$ so that all the colorbars vary from -1 to 1. The upper row shows the same configuration as used in Fig. 4.2 with uniform pulse magnitude and spacing. Compared to the results using the standard AKF, the results incorporating the convecting force model and ℓ_1 regularization demonstrate less spatial smearing, no holding locations, and lower overall error ($\varepsilon_{70\%} = 9.66\%$ versus 16.37% in the standard case). Further, because of the reduced smearing of the force estimates, the force integral plots more closely resemble the square-wave pulses of the truth force. The integrated force magnitude is similar to the truth but tends to slightly underestimate the truth. These properties can be seen in the force estimates for all cases presented here.

Immediately after each pulse leaves the beam tip in all cases, the estimated magnitude near the beam tip briefly reverses. This can be seen in both the force estimate surface plots and the integral plots in Fig. 4.5. We suspect that this artifact is due to the way the AKF estimates forces. Each pulse in the truth pulse train emerges on the beam discontinuously, but the Q_z force covariance term in the AKF attempts to smooth discontinuities. Forces near the root also yield lower magnitude responses and therefore lower quality information for the AKF. These effects result in the force magnitude near the root being initially underestimated while the force at the tip briefly reverses direction so that the estimated response can match the measured displacement.

The Larger Variance case in the bottom row of Fig. 4.5 demands additional discussion because no ℓ_1 regularization via pseudo-measurements is performed. In this case, the truth force is much less sparse than in the other cases, so no ℓ_1 regularization is required. Adding ℓ_1 regularization in this case still encourages a sparse estimate with less smearing, but that is undesirable when the truth force is smeared. This case shows that ℓ_1 regularization serves only to promote sparsity and is not essential to the underlying performance of the convecting force model.

4.2.3 Effects of Assumed Force Parameters

The convecting force model depends on the parameters ν and α to accurately model the spatial evolution of the truth force. The velocity parameter ν controls the expected convection velocity, while the decay coefficient α controls the amount of exponential decay that expected in the truth force. Figure 4.6a shows a plot of error as a function of the ratio between the assumed and truth velocities, ν/ν_t. As ν/ν_t approaches zero, the force estimate approaches the standard, zero-order hold AKF error of 16.37%. Error decreases

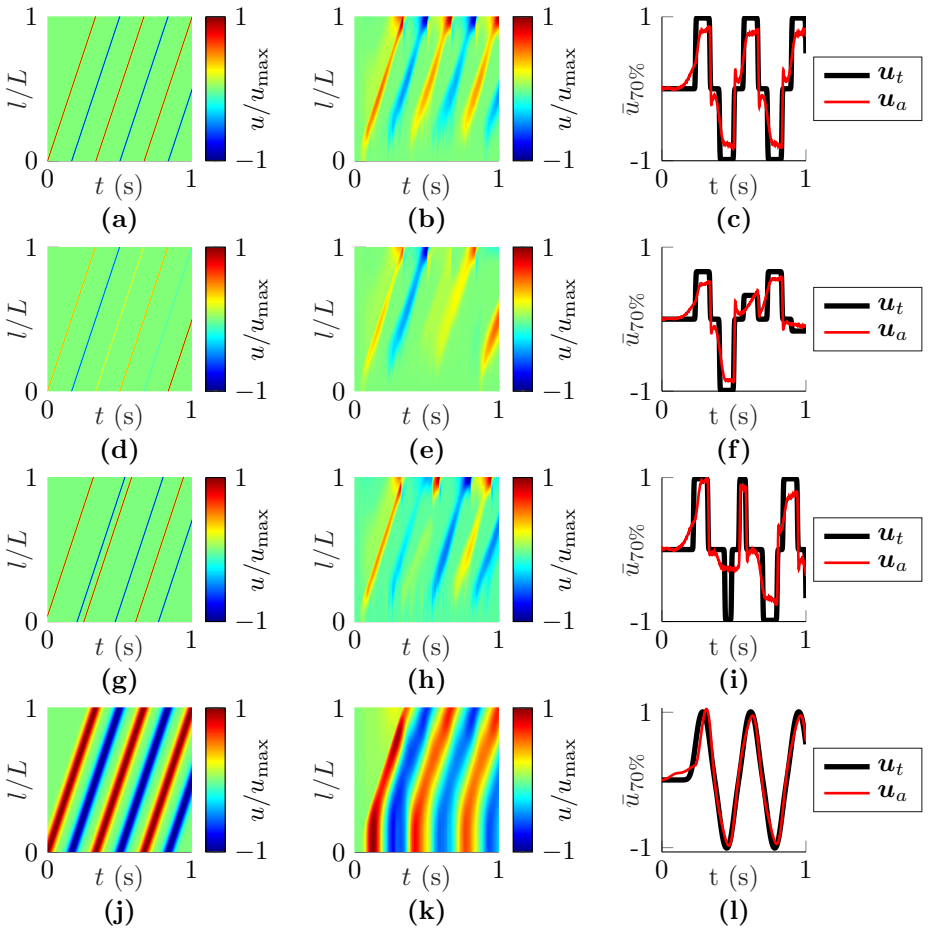

Figure 4.5. (left) Normalized truth force, (middle) normalized force estimated using the AKF with a convecting force model, and (right) force integral over the last 30% of the beam for (top row) evenly spaced, equal magnitude forces (Baseline, $\varepsilon_{70\%} = 9.66\%$); (second row) evenly spaced, unequal magnitude forces (Varying Magnitude, $\varepsilon_{70\%} = 10.93\%$); (third row) unevenly spaced, equal magnitude forces (Varying Spacing, $\varepsilon_{70\%} = 9.14\%$); and (bottom row) equal spacing, equal magnitude forces with larger variance (Larger Variance, $\varepsilon_{70\%} = 4.08\%$). No ℓ_1 regularization is performed for the final, large variance case.

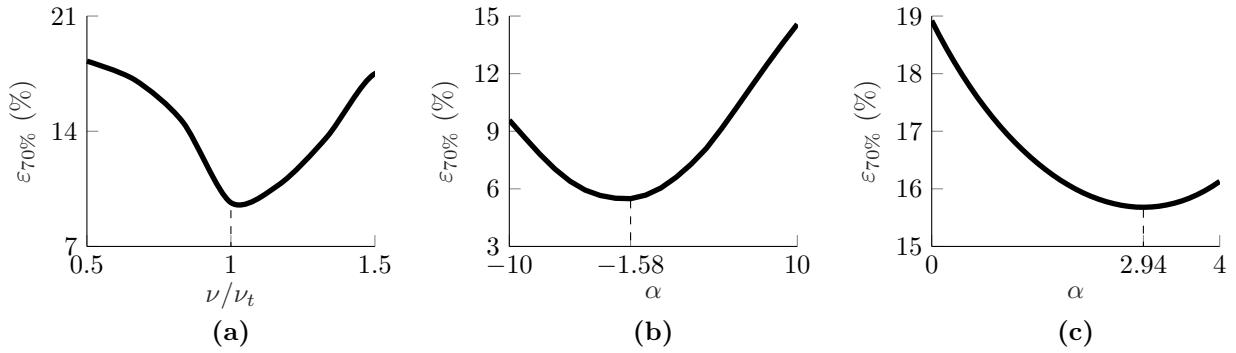

Figure 4.6. Mean squared error of force integrated over the last 30% of the beam as a function of (a) assumed velocity ν normalized by the truth velocity ν_t, (b) decay parameter α with $Q_z = 1\text{E}4$, and (c) decay parameter α with $Q_z = 1\text{E}2$.

monotonically toward the minimum-error case where the assumed velocity is the same as the truth, $\nu/\nu_t = 1$. At $\nu/\nu_t > 1$, the error again increases. Notice that the estimation error is less than the standard AKF error over the entire range of $0.5 < \nu/\nu_t < 1.5$ shown in the figure. Hence, if even a rough approximation of ν is known, the convecting force model can yield a better force estimate than the standard zero-order hold model. Additionally, ν can typically be accurately measured using radar or machine vision methods to detect the speed of vehicles, or a flow meter to detect the free-stream velocity of a flowing fluid.

To demonstrate the effects of adding a decay term, we simulate the response of the same system to the same smeared pulse train, except now the magnitude of each pulse takes the form of a decaying exponential. The equations for the truth load in this case are given in the "Decaying" row of Table 4.1. Figure 4.6b shows error for varying values of α. In this case $\alpha = -1.58$ yields the lowest error, which implies that a model that amplifies the force yields the lowest error even when the actual force decays. This is because the chosen $Q_z = 1\text{E}4$ slightly underestimates the force integral for $\alpha = 0$, so adding an amplification term helps the integral match the truth force. If we instead specify $Q_z = 1\text{E}2$, the force integral magnitude is slightly overestimated for $\alpha = 0$, and a positive α attenuates the force estimate. The parameter study for the $Q_z = 1\text{E}2$ case is shown in Fig. 4.6c, and $\alpha = 2.94$ minimizes the error. Figure 4.7 shows the force integral for $Q_z = 1\text{E}4$ and $\alpha = 0$ and $\alpha = -1.6$, as well as for $Q_z = 1\text{E}2$ and $\alpha = 0$ and $\alpha = 2.94$. The force integral plots reveal that the force estimate does not change appreciably between the $\alpha = 0$ case and the minimum error case for either choice of force covariance. From these results, we can see that there

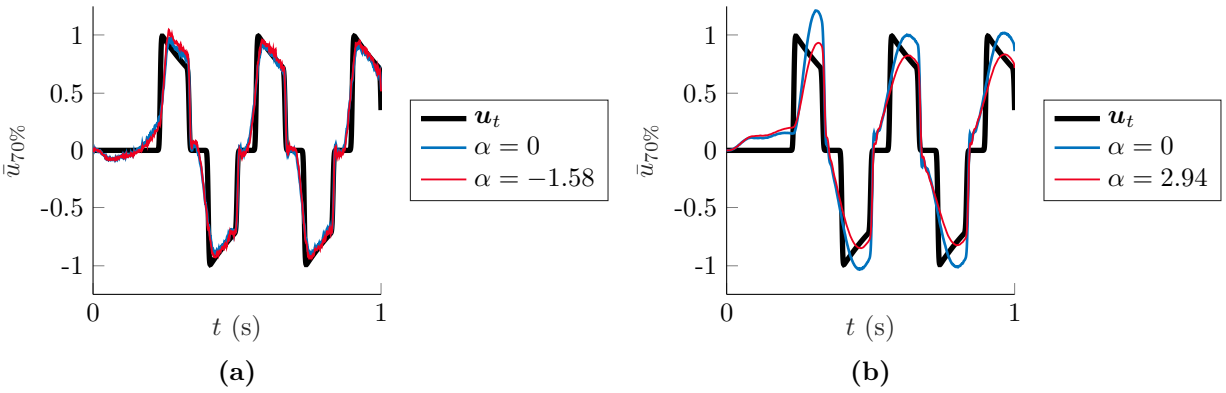

Figure 4.7. Force integral estimates for (a) $Q_z = 1\text{E}4$ and (b) $Q_z = 1\text{E}2$ with $\alpha = 0$ and the α that takes the value that minimizes the error.

is a complicated relationship between Q_z and α since both directly affect the estimated force magnitude. However, the error changes slowly over a wide range of α. Recall also that α is a physical parameter that represents a decay rate and should not be arbitrarily specified just to minimize error. Hence, the value of α should be specified as either 0 (no decay) or an appropriate estimate of the actual decay rate. Both values will typically yield an acceptable force estimate since the function of Q_z is to correct the force estimate based on response measurements.

4.3 Conclusions

The AKF-based force estimation method with novel convecting force model presented here yields significantly improved results for moving force estimation problems when compared to the standard zero-order hold model. Although the method still struggles to correctly identify the correct spatial distribution and magnitude of each force in the cases studied here, spatially integrating the truth force yields a resultant that is very similar to the truth force. The difficulty of correctly estimating the magnitude and spatial distribution of the force stems from the similarity between responses due to either low magnitude, highly spread forces or high magnitude concentrated forces. If the expected force magnitude or distribution was known *a priori*, it may be possible to include this information using the force model and R_γ terms, respectively. In many applications, however, the exact force distribution and magnitude are of lesser importance than the resultant force, so the force integration method used in the present work to compare the truth and estimated forces is

sufficient. The level of error presented in our force integral results is similar to the error achieved by modern moving load estimation techniques, and our technique does not require a precise estimate of the force velocity [72, 76]. The method is suitable for moving concentrated loads using an ℓ_1 regularization scheme, but the convecting force model can also be used to estimate distributed loads moving if ℓ_1 regularization is not used. We expect that the convecting force model should be immediately applicable to moving force problems in various domains, including weigh-in-motion systems and dynamic fluid pressure estimation.

The techniques described here require more parameters to be specified than the standard AKF. These parameters were specified using trial and error in the present work, but more robust automatic parameter selection techniques should be developed for critical applications. In addition to the standard AKF parameters of the measurement covariance, model covariance, and force covariance, the convecting force model contains a decay term and assumed velocity term, while the ℓ_1 regularization technique introduces a pseudo-measurement covariance. The pseudo-measurement covariance can be tuned in the same way as the force covariance from the standard AKF using the L-curve method [84]. The assumed velocity parameter can usually be measured directly from the system, but our results show that even an imprecise estimate still yields improved results over the standard zero-order hold model. One might expect that adding the decay term (or another appropriate model of the force magnitude) would yield an improved estimate as well, but the results presented here suggest that adding a decay term can actually hinder the estimation process because of the complicated interactions between the decay parameter and force covariance. We therefore recommend ignoring the decay term and allowing the force covariance term to control the force estimate.

The convecting force model presented here is a simple way to incorporate additional information about the expected behavior of the force into the AKF since the state transition matrix A^* remains static. However, it would be possible to specify other types of assumed force motions by recalculating the state transition matrix at every timestep based on the instantaneous assumed velocity. This could be useful, for instance, for weigh-in-motion systems on roads that occasionally reverse directions or fluid systems where the free-stream velocity changes. In both these cases, the AKF could be augmented by using a velocimeter to continuously correct the assumed velocity parameter and recalculate the associated state transition matrix. This would be especially helpful for estimating the fluid pressure over 2D surfaces where the flow can change magnitude and direction.

Chapter 5

Conclusions and Future Work

5.1 Conclusions

Forces on structures can broadly be categorized as static, harmonic, or general dynamic forces. This dissertation presents a set of methods for estimating loads from each of these categories using sparse measurements of the structural response. While the methods presented in the preceding chapters by no means represent a comprehensive set of modern techniques for inverse force estimation, the cited literature together with the details of the described techniques should provide the interested reader with a sufficient set of methods for solving a wide variety of input estimation problems.

The analytical methods for distributed static force estimation from strain measurements (Ch. 2) demonstrate how cumbersome the equations governing inverse force estimation problems can be if the equations are derived analytically. Even for the simplest case of distributed force estimation on a classical beam with constraints on both ends, the governing equations are unwieldy, and the optimal sensor configurations are counter-intuitive. Even when the system equations are known exactly and an optimal sensor configuration is used, the force estimates obtained by inverting the system matrix without regularization are unimpressive. However, the methods described in the static force estimation chapter are valuable because they provide insights into both the fine details of the influence coefficient model and the mathematical difficulties inherent to inverse problems.

The methods for distributed harmonic force estimation from acceleration measurements (Ch. 3) is an expansion on the static force estimation techniques. The static and harmonic techniques both ultimately rely on inverting a system matrix, but numerical techniques are used to construct the system matrix for the harmonic force estimation techniques, and modern regularization techniques are used to obtain better force

estimates using fewer measurements. In addition, the chapter on harmonic force estimation highlights the relative importance of sensor placement and regularization. While careful sensor placement is important to ensure the inversion process has enough information to yield an acceptable estimate, regularization is far more important to improving the results than optimal sensor placement as long as the sensor configuration is chosen intelligently. Additionally, including prior knowledge of the spatial form of the force in the regularization process enables high-quality force estimates in situations where standard regularization is inadequate. It is important to note that since the underlying matrix inversion that makes the static and harmonic force estimation techniques possible is very similar between the two cases, the numerical regularization and structural matrix generation techniques that enhance the harmonic force estimates can also be directly applied to the static load estimation case.

The moving force estimation technique differs from the static and harmonic force estimation methods because the dynamic method is not based on direct matrix inversion. Instead, the Kalman filter-based method provides computational complexity that scales linearly with time, like the harmonic force estimation method scales with frequency. However, because the method is not based on matrix inversion and the time steps are interdependent, unlike the frequency steps in the harmonic forcing case, regularization in the dynamic case must be handled differently. Part of the regularization for the AKF technique is accomplished using a convecting force model. This model provides additional general information about the force beyond what is normally captured using the standard zero-order hold force model. Together, the techniques presented here for static, harmonic, and general dynamic force estimation provide a representative overview of the state of the art in structural input estimation techniques, complete with a complete discussion of the challenges inherent to the solution of inverse problems.

5.2 Future Work

Among the three methods presented above, there are many opportunities for future research. This section outlines some of these possibilities, along with some initial thoughts on research methods and possible challenges.

5.2.1 Automatic parameter estimation

When regularization is used, the estimation quality depends on a set of parameters. This is true for matrix regularization as well as the regularization used by the AKF. For instance, the Tikhonov regularization described in Ch. 3 requires a regularization parameter and a smoothing parameter, while the AKF regularization scheme requires a force covariance and pseudo measurement variance. In classical regularization, only one parameter (the regularization parameter) is estimated. In this case, the L-curve method can be used to estimate the optimal value that minimizes both the fitting norm and solution norm [84]. It should be theoretically possible to use an L-curve like technique to optimize multiple hyperparameters simultaneously by calculating the fitting and solution norms for combinations of parameters over a wide range of values, but the computational complexity of this method would scale poorly with the number of parameters. It may also be possible to take inspiration from hierarchical Bayesian techniques that frame the force estimation problem such that the hyperparameters and force estimates are estimated simultaneously via MCMC sampling [45]. However, it may be impossible to implement such a technique in other frameworks since it requires probability distribution representations of the relevant equations to rapidly sample solution and parameter configurations.

5.2.2 Concentrated forces at unknown locations

The static and harmonic force estimation methods presented in this work are suitable for estimating loads distributed across a domain, but their ability to estimate point loads at unknown locations has not been tested. If concentrated loads are applied at known locations, it is trivial to incorporate knowledge about their locations by reducing the influence coefficient or FRM matrix to a form in which the force magnitudes are estimated only at the desired locations. However, if the location is not known, it must be estimated along with the magnitude. The assumed distributed force basis used in the static case would be useless in this case since that force basis is incapable of yielding concentrated forces. It would be necessary instead to parameterize the problem as in the harmonic force case by assuming forces at every DOF across the domain. The ℓ_2 regularization used to promote a smooth, distributed solution could be replaced with the ℓ_1 regularization that would promote a sparse solution. The same method of incorporating prior knowledge of the assumed form of the force could still be used with the new ℓ_1 regularization scheme. If ℓ_1 regularization was used instead of ℓ_2 regularization, the method would no longer be suitable for distributed loads. In

the general case where it is unknown whether the structure will be subject to distributed or point loads, it may be possible to implement q-norm regularization instead. This technique would introduce another hyperparameter that controls the regularization norm, but would allow for general forcing as long as the new hyperparameter could be tuned automatically.

5.2.3 Distributed transient dynamic forces

The problem of estimating distributed transient dynamic loads on structures can theoretically be handled using the same AKF method described for moving load estimation in Ch. 4, but the details of the problem make it much more difficult. First, the convecting force model and pseudo-measurement-based regularization methods do not work for general distributed loads because the force does not necessarily convect monotonically, and sparsity is not desired. It is possible to provide the AKF with an assumed force at every time step by returning the AKF state transition equation to its standard Kalman filter form that includes a control input and using the assumed force at every timestep as a control input. In this case, the force estimate from the AKF becomes a perturbation term that must be added to the assumed force to obtain the final force estimate. However, it would likely be impractical in most applications to time-synchronize an assumed force to the time series response data unless force or pressure sensors are used to supply the force prior in real time. The only regularization technique remaining then is the force covariance matrix Q_z, which acts as the regularization parameter in standard Tikhonov regularization. It may be possible to obtain an acceptable force estimate by simply tuning the force covariance matrix for force configurations that vary slowly in space, but short-wavelength forces may not be adequately reconstructed in the absence of a prior force estimate, since Tikhonov regularization operates by discarding high-frequency content in the solution vector, as described by the Picard condition [84]. In this case, the AKF may not be suitable for short-wavelength distributed force reconstruction. Instead, better results may be achieved by using a Bayesian inference scheme with a prior estimate of the force to estimate the force across the full time series simultaneously. As long as the force profile changes slowly compared to the timestep and continuously in time, it may be acceptable to roughly synchronize the force estimate with the response data for offline applications.

5.2.4 Different AKF Force Models

The traveling force estimation technique presented here uses a convecting force model that assumes that force moves monotonically at an approximately constant speed, but other force models are likely possible. The convecting force model can be readily modified for use with non-constant velocities by recalculating the augmented state transition matrix at every timestep using the instantaneous assumed force velocity. While computationally expensive, this technique would be simple to implement since the instantaneous velocity can be directly measured in many applications.

Other types of force models that are not based on force position are also possible. If the prior estimate of a force can be represented as a linear combination of state variables (positions, velocities, force magnitudes), the same force modeling technique demonstrated here can be used. For instance, if a force is due to a linear spring or damper connected to a structural DOF, the force prior could be represented by placing a stiffness or damping coefficient in the state transition matrix in the force's row and the column corresponding to the DOF's displacement or velocity. As another example, if all the forces in a region are expected to be approximately equal (as in the case of a large sled being dragged across the domain), it would be possible to specify that the associated forces take the mean value of these forces during the next prediction step.

Appendices

Appendix A

Boundary Condition Coefficients

This appendix contains the expressions for the boundary condition coefficients C_V and C_M found in Eqs. (2.6) and (2.8). The coefficients depend on the boundary condition and the type of loading (UDL or LDL). The formulations for each configuration are separated into subsections. For the following equations, we define the following terms for convenience

$$\begin{aligned}
\tau_f(s,x) &= \int \mu_f dx = \\
&\left(\frac{-1}{a_{s+1}-a_s}\right)\left(a_s\frac{x^3}{6} - \frac{x^4}{24} - a_s a_{s+1}\frac{x^2}{2} + \frac{a_{s+1}^2}{2}\frac{x^2}{2} + a_s\frac{a_{s+1}^2}{2}x - \frac{a_{s+1}^3}{3}x\right) \\
&+ a_{s+1}\frac{x^2}{2} - \frac{x^3}{6} - \frac{a_{s+1}^2}{2}x \\
\tau_c(s,x) &= \int \mu_c dx = \\
&\left(\frac{-1}{a_{s+1}-a_s}\right)\left(\frac{x^2}{2}\left(\frac{a_s^2}{2} - a_s a_{s+1} + \frac{a_{s+1}^2}{2}\right) - \frac{a_s^3}{6}x + a_s\frac{a_{s+1}^2}{2}x - \frac{a_{s+1}^3}{3}x\right) \\
&+ a_{s+1}\frac{x^2}{2} - \frac{x^3}{6} - \frac{a_{s+1}^2}{2}x \\
\tau_l(s,x) &= \int \mu_l dx = \left(\frac{-1}{a_{s+1}-a_s}\right)\left(\frac{a_s^2}{2}\frac{x^2}{2} - \frac{a_s^3}{6}x\right) - \frac{x^3}{6}
\end{aligned} \quad , \tag{A.1}$$

$$
\begin{aligned}
\nu_f(s,x) &= \int \tau_f dx = \\
&\left(\frac{-1}{a_{s+1}-a_s}\right)\left(a_s\frac{x^4}{24} - \frac{x^5}{120} - a_s a_{s+1}\frac{x^3}{6} + \frac{a_{s+1}^2}{2}\frac{x^3}{6} + a_s\frac{a_{s+1}^2}{2}\frac{x^2}{2} - \frac{a_{s+1}^3}{3}\frac{x^2}{2}\right) \\
&+ a_{s+1}\frac{x^3}{6} - \frac{x^4}{24} - \frac{a_{s+1}^2}{2}\frac{x^2}{2} \\
\nu_c(s,x) &= \int \tau_c dx = \\
&\left(\frac{-1}{a_{s+1}-a_s}\right)\left(\frac{x^3}{6}\left(\frac{a_s^2}{2} - a_s a_{s+1} + \frac{a_{s+1}^2}{2}\right) - \frac{a_s^3}{6}\frac{x^2}{2} + a_s\frac{a_{s+1}^2}{2}\frac{x^2}{2} - \frac{a_{s+1}^3}{3}\frac{x^2}{2}\right) \\
&+ a_{s+1}\frac{x^3}{6} - \frac{x^4}{24} - \frac{a_{s+1}^2}{2}\frac{x^2}{2} \\
\nu_l(s,x) &= \int \tau_l dx = \left(\frac{-1}{a_{s+1}-a_s}\right)\left(\frac{a_s^2}{2}\frac{x^3}{6} - \frac{a_s^3}{6}\frac{x^2}{2}\right) - \frac{x^4}{24}
\end{aligned}
\tag{A.2}
$$

A.0.1 UDL

A.0.1.1 Clamped-Free (CF)

$$
\begin{aligned}
C_V &= p_l a_l \\
C_M &= -p_l\frac{a_l^2}{2}
\end{aligned}
\tag{A.3}
$$

A.0.1.2 Simply Supported (SS)

$$
\begin{aligned}
C_V &= \frac{1}{a_l}\left(p_l\frac{a_l^2}{2} - p_1\frac{a_1^2}{2} + p_l\frac{a_{l-1}^2}{2} + \sum_{j=2}^{l-1} p_j\left(\frac{a_{j-1}^2}{2} - \frac{a_j^2}{2}\right)\right) \\
C_M &= p_1\frac{a_1^2}{2} - p_l\frac{a_{l-1}^2}{2} - \sum_{j=2}^{l-1} p_j\left(-\frac{a_j^2}{2} + \frac{a_{j-1}^2}{2}\right)
\end{aligned}
\tag{A.4}
$$

A.0.1.3 Clamped-Clamped (CC)

$$
\begin{aligned}
C_w &= p_1 \frac{a_1^4}{24} - p_l \frac{a_{l-1}^4}{24} - \sum_{j=2}^{l-1} p_j \left(\frac{a_{j-1}^4}{24} - \frac{a_j^4}{24} \right) \\
C_\theta &= p_l \frac{a_{l-1}^3}{6} - p_1 \frac{a_1^3}{6} - \sum_{j=2}^{l-1} p_j \left(\frac{a_j^3}{6} - \frac{a_{j-1}^3}{6} \right) \\
C_M &= \left(\frac{2}{a_l^2} \right) \left(p_l \frac{a_l^4}{24} - C_\theta a_l - C_w - C_V \frac{a_l^3}{6} \right) \\
C_V &= \left(\frac{6}{a_l^2} \right) \left(p_l \frac{a_l^3}{12} + C_\theta + \frac{2}{a_l} C_w \right)
\end{aligned}
\tag{A.5}
$$

A.0.1.4 Clamped-Simply Supported (CS)

$$
\begin{aligned}
C_u &= p_1 \frac{a_1^4}{24} - p_l \frac{a_{l-1}^4}{24} - \sum_{j=2}^{l-1} p_j \left(\frac{a_{j-1}^4}{24} - \frac{a_j^4}{24} \right) \\
C_\theta &= -p_1 \frac{a_1^3}{6} + p_l \frac{a_{l-1}^3}{6} - \sum_{j=2}^{l-1} p_j \left(\frac{a_j^3}{6} - \frac{a_{j-1}^3}{6} \right) \\
C_V &= p_l \left(\frac{5 a_l}{8} \right) + C_\theta \frac{3}{a_l^2} + C_w \frac{3}{a_l^3} \\
C_M &= p_l \frac{a_l^2}{2} - C_V a_l
\end{aligned}
\tag{A.6}
$$

A.0.2 LDL

A.0.2.1 Clamped-Free (CF)

$$
\begin{aligned}
C_V &= p_{l+1} \left(\left(\frac{-1}{a_{l+1} - a_l} \right) \left(a_l a_{l+1} - \frac{a_{l+1}^2}{2} \right) \right) + p_l \left(\left(\frac{1}{a_{l+1} - a_l} \right) \left(a_l a_{l+1} - \frac{a_{l+1}^2}{2} \right) + a_{l+1} \right) \\
C_M &= p_{l+1} \left(\left(\frac{1}{a_{l+1} - a_l} \right) \left(\frac{-a_{l+1}^3}{3} + a_l \frac{a_{l+1}^2}{2} \right) \right) + p_l \left(\left(\frac{-1}{a_{l+1} - a_l} \right) \left(\frac{-a_{l+1}^3}{3} + a_l \frac{a_{l+1}^2}{2} \right) - \frac{a_{l+1}^2}{2} \right)
\end{aligned}
\tag{A.7}
$$

A.0.2.2 Simply Supported (SS)

$$
\begin{aligned}
C_M &= -p_1(\mu_f(1,0)) - p_2(\mu_c(2,0) - \mu_f(1,0)) - p_l(\mu_l(l,0) - \mu_c(l-1,0)) + p_{l+1}(\mu_l(l,0)) \\
&\quad - \left(\sum_{j=3}^{l-1} p_j \left(\mu_c(j,0) - \mu_c(j-1,0) \right) \right) \\
C_V &= \frac{1}{a_{l+1}} \left(p_{l+1} \left(\left(\frac{-1}{a_{l+1} - a_l} \right) \left(\frac{-a_{l+1}^3}{6} + a_l \frac{a_{l+1}^2}{2} \right) \right) \right. \\
&\quad \left. + p_l \left(\left(\frac{1}{a_{l+1} - a_l} \right) \left(\frac{-a_{l+1}^3}{6} + a_l \frac{a_{l+1}^2}{2} \right) + \frac{a_{l+1}^2}{2} \right) - C_M \right)
\end{aligned}
\tag{A.8}
$$

A.0.2.3 Clamped-Clamped (CC)

$$
\begin{aligned}
C_w &= p_1(\nu_f(1,a_2) - \tau_f(1,a_2)a_2) \\
&+ p_2(-\nu_f(2,a_2) + \nu_c(2,a_2) - \nu_f(1,a_2) + \tau_f(2,a_2)a_2 + \tau_f(1,a_2)a_2 - \tau_c(2,a_2)a_2 + \nu_f(2,a_3) - \tau_f(2,a_3)a_3) \\
&+ p_l \left(\text{-}\nu_f(l-1,a_{l-1}) - \nu_c(l-1,a_{l-1}) + \tau_c(l-1,a_{l-1})a_{l-1} - \tau_f(l-1,a_{l-1})a_{l-1} \right. \\
&\quad + \left(\frac{1}{a_{l+1}-a_l}\right)\left(\frac{a_l^5}{30}\right) + \frac{a_l^4}{24} + \nu_l(l,a_l) - \nu_f(l-1,a_l) \\
&\quad \left. + \left(\frac{-1}{a_{l+1}-a_l}\right)\left(\frac{a_l^5}{8} - \frac{a_l^4}{6}\right) - \tau_l(l,a_l)a_l + \tau_f(l-1,a_l)a_l \right) \\
&+ p_{l+1}\left(\left(\frac{-1}{a_{l+1}-a_l}\right)\left(\frac{a_l^5}{30}\right) - \nu_l(l,a_l) - \frac{a_l^4}{24} + \left(\frac{1}{a_{l+1}-a_l}\right)\left(\frac{a_l^5}{8}\right) + \tau_l(l,a_l)a_l + \frac{a_l^4}{6}\right) \\
&+ \sum_{j=3}^{l-1} p_j \left(\nu_f(j-1,a_{j-1}) - \nu_c(j-1,a_{j-1}) - \tau_f(j-1,a_{j-1})a_{j-1}\right. \\
&\quad + \tau_c(j-1,a_{j-1})a_{j-1} - \nu_f(j-1,a_j) + \tau_f(j-1,a_j)a_j - \nu_f(j,a_j) + \nu_c(j,a_j) + \tau_f(j,a_j)a_j \\
&\quad \left. - \tau_c(j,a_j)a_j + \nu_f(j,a_{j+1}) - \tau_f(j,a_{j+1})a_{j+1}\right) \\
C_\theta &= p_1(\tau_f(1,a_2)) + p_2(-\tau_f(2,a_2) - \tau_f(1,a_2) + \tau_c(2,a_2) + \tau_f(2,a_3)) \\
&+ p_l\left(-\tau_c(l-1,a_{l-1}) + \tau_f(l-1,a_{l-1}) + \left(\frac{1}{a_{l+1}-a_l}\right)\left(\frac{a_l^4}{8}\right) + \frac{a_l^3}{6} + \tau_l(l,a_l) - \tau_f(l-1,a_l)\right) \\
&+ p_{l+1}\left(\left(\frac{-1}{a_{l+1}-a_l}\right)\left(\frac{a_l^4}{8}\right) - \tau_l(l,a_l) - \frac{a_l^3}{6}\right) \\
&+ \sum_{j=3}^{l-1} p_j \left(\tau_f(j-1,a_{j-1}) - \tau_c(j-1,a_{j-1}) - \tau_f(j-1,a_j) - \tau_f(j,a_j) + \tau_c(j,a_j) + \tau_f(j,a_{j+1})\right) \\
C_M &= \frac{6}{a_{l+1}^2}\left(p_l\left(\left(\frac{1}{a_{l+1}-a_l}\right)\left(\frac{-a_{l+1}^5}{120} + a_l\frac{a_{l+1}^4}{24}\right) + \frac{a_{l+1}^4}{24}\right)\right. \\
&\quad \left. + p_{l+1}\left(\left(\frac{-1}{a_{l+1}-a_l}\right)\left(\frac{-a_{l+1}^5}{120} + a_l\frac{a_{l+1}^4}{24}\right)\right) - C_\theta a_{l+1} - C_w\right) \\
&\quad - \frac{2}{a_{l+1}}\left(p_l\left(\left(\frac{1}{a_{l+1}-a_l}\right)\left(\frac{-a_{l+1}^4}{24} + a_l\frac{a_{l+1}^3}{6}\right) + \frac{a_{l+1}^3}{6}\right)\right. \\
&\quad \left. + p_{l+1}\left(\left(\frac{-1}{a_{l+1}-a_l}\right)\left(\frac{-a_{l+1}^4}{24} + a_l\frac{a_{l+1}^3}{6}\right)\right) - C_\theta\right) \\
C_V &= \frac{2}{a_{l+1}^2}\left(p_l\left(\left(\frac{1}{a_{l+1}-a_l}\right)\left(\frac{-a_{l+1}^4}{24} + a_l\frac{a_{l+1}^3}{6}\right) + \frac{a_{l+1}^3}{6}\right)\right. \\
&\quad \left. + p_{l+1}\left(\left(\frac{-1}{a_{l+1}-a_l}\right)\left(\frac{-a_{l+1}^4}{24} + a_l\frac{a_{l+1}^3}{6}\right)\right) - C_M a_{l+1} - C_\theta\right)
\end{aligned}
\tag{A.9}
$$

A.0.2.4 Clamped-Simply Supported (CS)

C_θ and C_w take the same form as in Eqs. A.9.

$$
\begin{aligned}
C_V = \frac{1}{a_{l+1}} \Bigg(& p_l \left(\left(\frac{1}{a_{l+1} - a_l} \right) \left(\frac{-a_{l+1}^3}{6} + a_l \frac{a_{l+1}^2}{2} \right) + \frac{a_{l+1}^2}{2} \right) + p_{l+1} \left(\left(\frac{-1}{a_{l+1} - a_l} \right) \left(\frac{-a_{l+1}^3}{6} + a_l \frac{a_{l+1}^2}{2} \right) \right) - C_M \Bigg) \\
C_M = \frac{3}{a_{l+1}^2} \Bigg(& p_l \left(\left(\frac{1}{a_{l+1} - a_l} \right) \left(\frac{-a_{l+1}^5}{120} + a_l \frac{a_{l+1}^4}{24} \right) + \frac{a_{l+1}^4}{24} \right) + p_{l+1} \left(\left(\frac{-1}{a_{l+1} - a_l} \right) \left(\frac{-a_{l+1}^5}{120} + a_l \frac{a_{l+1}^4}{24} \right) \right) \\
& - \frac{a_{l+1}^2}{6} \Bigg(p_l \left(\left(\frac{1}{a_{l+1} - a_l} \right) \left(\frac{-a_{l+1}^3}{6} + a_l \frac{a_{l+1}^2}{2} \right) + \frac{a_{l+1}^2}{2} \right) \\
& + p_{l+1} \left(\left(\frac{-1}{a_{l+1} - a_l} \right) \left(\frac{-a_{l+1}^3}{6} + a_l \frac{a_{l+1}^2}{2} \right) \right) \Bigg) - C_\theta a_{l+1} - C_w \Bigg)
\end{aligned}
\tag{A.10}
$$

Appendix B

Special Cases for small l

This appendix contains the moment equations and corresponding boundary condition coefficients for UDL loading with $l = 1$, and LDL loading with $l = 1$ or $l = 2$.

B.0.1 UDL, $l = 1$

$$M(x) = -p_1 \frac{x^2}{2} + C_V x + C_M \tag{B.1}$$

B.0.1.1 Clamped-Free (CF)

$$\begin{aligned} C_V &= p_1 a_1 \\ C_M &= -p_1 \frac{a_1^2}{2} \end{aligned} \tag{B.2}$$

B.0.1.2 Simply Supported (SS)

$$\begin{aligned} C_V &= p_1 \frac{a_1}{2} \\ C_M &= 0 \end{aligned} \tag{B.3}$$

B.0.1.3 Clamped-Clamped (CC)

$$\begin{aligned} C_V &= p_1 \frac{a_1}{2} \\ C_M &= -p_1 \frac{a_1^2}{12} \end{aligned} \tag{B.4}$$

B.0.1.4 Clamped-Simply Supported (CS)

$$\begin{aligned} C_V &= p_1 \frac{15a_1}{24} \\ C_M &= -p_1 \frac{3a_1^2}{24} \end{aligned} \tag{B.5}$$

B.0.2 LDL, $l = 1$

$$\begin{aligned} M(x) = p_1 &\left(\left(\frac{1}{a_2 - a_1} \right) \left(\frac{x^3}{6} - a_1 \frac{x^2}{2} \right) - \frac{x^2}{2} \right) \\ &+ p_2 \left(\left(\frac{-1}{a_2 - a_1} \right) \left(\frac{x^3}{6} - a_1 \frac{x^2}{2} \right) \right) + C_V x + C_M \end{aligned} \tag{B.6}$$

B.0.2.1 Clamped-Free (CF)

$$\begin{aligned} C_V &= p_1 \left(\left(\frac{-1}{a_2 - a_1} \right) \left(\frac{a_2^2}{2} - a_1 a_2 \right) + a_2 \right) + p_2 \left(\left(\frac{1}{a_2 - a_1} \right) \left(\frac{a_2^2}{2} - a_1 a_2 \right) \right) \\ C_M &= p_1 \left(\left(\frac{-1}{a_2 - a_1} \right) \left(\frac{a_2^3}{6} - a_1 \frac{a_2^2}{2} \right) + \frac{a_2^2}{2} \right) + p_2 \left(\left(\frac{1}{a_2 - a_1} \right) \left(\frac{a_2^3}{6} - a_1 \frac{a_2^2}{2} \right) \right) - C_V a_2 \end{aligned} \tag{B.7}$$

B.0.2.2 Simply Supported (SS)

$$\begin{aligned} C_V &= \frac{1}{a_2} \left(p_1 \left(\left(\frac{-1}{a_2 - a_1} \right) \left(\frac{a_2^3}{6} - a_1 \frac{a_2^2}{2} \right) + \frac{a_2^2}{2} \right) + p_2 \left(\left(\frac{1}{a_2 - a_1} \right) \left(\frac{a_2^3}{6} - a_1 \frac{a_2^2}{2} \right) \right) \right) \\ C_M &= 0 \end{aligned} \tag{B.8}$$

B.0.2.3 Clamped-Clamped (CC)

$$\begin{aligned} C_V = &\frac{-6}{a_2^2} \left(p_1 \left(\left(\frac{1}{a_2 - a_1} \right) \left(\frac{a_2^4}{24} - a_1 \frac{a_2^3}{6} \right) - \frac{a_2^3}{6} \right) + p_2 \left(\left(\frac{-1}{a_2 - a_1} \right) \left(\frac{a_2^4}{24} - a_1 \frac{a_2^3}{6} \right) \right) \right. \\ &\left. + \frac{-2}{a_2} \left(p_1 \left(\left(\frac{1}{a_2 - a_1} \right) \left(\frac{a_2^5}{120} - a_1 \frac{a_2^4}{24} \right) - \frac{a_2^4}{24} \right) + p_2 \left(\left(\frac{-1}{a_2 - a_1} \right) \left(\frac{a_2^5}{120} - a_1 \frac{a_2^4}{24} \right) \right) \right) \right) \\ C_M = &\frac{-2}{a_2^2} \left(p_1 \left(\left(\frac{1}{a_2 - a_1} \right) \left(\frac{a_2^5}{120} - a_1 \frac{a_2^4}{24} \right) - \frac{a_2^4}{24} \right) + p_2 \left(\left(\frac{-1}{a_2 - a_1} \right) \left(\frac{a_2^5}{120} - a_1 \frac{a_2^4}{24} \right) \right) + C_V \frac{a_2^3}{6} \right) \end{aligned} \tag{B.9}$$

B.0.2.4 Clamped-Simply Supported (CS)

$$
\begin{aligned}
C_V &= \frac{-3}{2a_2}\left(p_1\left(\left(\frac{1}{a_2-a_1}\right)\left(\frac{a_2^3}{6}-a_1\frac{a_2^2}{2}\right)-\frac{a_2^2}{2}\right)+p_2\left(\left(\frac{-1}{a_2-a_1}\right)\left(\frac{a_2^3}{6}-a_1\frac{a_2^2}{2}\right)\right)\right.\\
&\left.+\frac{-2}{a_2^2}\left(p_1\left(\left(\frac{1}{a_2-a_1}\right)\left(\frac{a_2^5}{120}-a_1\frac{a_2^4}{24}\right)-\frac{a_2^4}{24}\right)+p_2\left(\left(\frac{-1}{a_2-a_1}\right)\left(\frac{a_2^5}{120}-a_1\frac{a_2^4}{24}\right)\right)\right)\right)\\
C_M &= \frac{-2}{a_2^2}\left(p_1\left(\left(\frac{1}{a_2-a_1}\right)\left(\frac{a_2^5}{120}-a_1\frac{a_2^4}{24}\right)-\frac{a_2^4}{24}\right)+p_2\left(\left(\frac{-1}{a_2-a_1}\right)\left(\frac{a_2^5}{120}-a_1\frac{a_2^4}{24}\right)\right)+C_V\frac{a_2^3}{6}\right)
\end{aligned}
\tag{B.10}
$$

B.0.3 LDL, $l = 2$

$$
\begin{aligned}
M_i(x) &= p_i(\mu_f(i,x)) + p_{i+1}(\mu_l(i+1,x)-\mu_f(i,x))\\
&\quad - p_{l+1}(\mu_l(l,x)+\frac{x^2}{2}) + C_V x + C_M, && i = l-1,\\
M_i(x) &= p_l\left(\left(\frac{-1}{a_{l+1}-a_l}\right)\left(\frac{-x^3}{6}+a_l\frac{x^2}{2}\right)-\frac{x^2}{2}\right)\\
&\quad + p_{l+1}\left(\left(\frac{1}{a_{l+1}-a_l}\right)\left(\frac{-x^3}{6}+a_l\frac{x^2}{2}\right)\right)+C_V x + C_M, && i = l
\end{aligned}
\tag{B.11}
$$

B.0.3.1 Clamped-Free (CF)

$$
\begin{aligned}
C_V &= p_{l+1}\left(\left(\frac{-1}{a_{l+1}-a_l}\right)\left(a_l a_{l+1}-\frac{a_{l+1}^2}{2}\right)\right)+p_l\left(\left(\frac{1}{a_{l+1}-a_l}\right)\left(a_l a_{l+1}-\frac{a_{l+1}^2}{2}\right)+a_{l+1}\right)\\
C_M &= p_{l+1}\left(\left(\frac{1}{a_{l+1}-a_l}\right)\left(\frac{-a_{l+1}^3}{3}+a_l\frac{a_{l+1}^2}{2}\right)\right)+p_l\left(\left(\frac{-1}{a_{l+1}-a_l}\right)\left(\frac{-a_{l+1}^3}{3}+a_l\frac{a_{l+1}^2}{2}\right)-\frac{a_{l+1}^2}{2}\right)
\end{aligned}
\tag{B.12}
$$

B.0.3.2 Simply Supported (SS)

$$
\begin{aligned}
C_V &= \frac{1}{a_3}\left(p_2\left(\left(\frac{1}{a_3-a_2}\right)\left(\frac{-a_3^3}{6}+a_2\frac{a_3^2}{2}\right)+\frac{a_3^2}{2}\right)+p_3\left(\left(\frac{-1}{a_3-a_2}\right)\left(\frac{-a_3^3}{6}+a_2\frac{a_3^2}{2}\right)\right)-C_M\right)\\
C_M &= -p_1(\mu_f(1,0))-p_2(\mu_l(2,0)-\mu_f(1,0))+p_3(\mu_l(2,0))
\end{aligned}
\tag{B.13}
$$

B.0.3.3 Clamped-Clamped (CC)

$$
\begin{aligned}
C_w &= -p_1(-\nu_f(1,a_2)+\tau_f(1,a_2)a_2) \\
&\quad - p_2\left(\left(\frac{-1}{a_3-a_2}\frac{a_2^5}{30}\right)-\frac{a_2^4}{24}-\nu_l(2,a_2)+\nu_f(1,a_2)+\left(\frac{1}{a_3-a_2}\right)\left(\frac{a_2^4}{8}\right)a_2+\frac{a_2^3}{6}a_2+\tau_l(2,a_2)a_2-\tau_f(1,a_2)a_2\right) \\
&\quad - p_3\left(\left(\frac{1}{a_3-a_2}\frac{a_2^5}{30}\right)+\frac{a_2^4}{24}+\nu_l(2,a_2)+\left(\frac{-1}{a_3-a_2}\right)\left(\frac{a_2^4}{8}\right)a_2-\frac{a_2^3}{6}a_2-\tau_l(2,a_2)a_2\right) \\
C_\theta &= -p_1(-\tau_f(1,a_2)) - p_2\left(\left(\frac{-1}{a_3-a_2}\right)\left(\frac{a_2^4}{8}\right)-\frac{a_2^3}{6}-\tau_l(2,a_2)+\tau_f(1,a_2)\right) \\
&\quad - p_3\left(\left(\frac{1}{a_3-a_2}\right)\left(\frac{a_2^4}{8}\right)+\tau_l(2,a_2)+\frac{a_2^3}{6}\right) \\
C_M &= \frac{6}{a_{l+1}^2}\left(p_l\left(\left(\frac{1}{a_{l+1}-a_l}\right)\left(\frac{-a_{l+1}^5}{120}+a_l\frac{a_{l+1}^4}{24}\right)+\frac{a_{l+1}^4}{24}\right)\right. \\
&\quad \left. +p_{l+1}\left(\left(\frac{-1}{a_{l+1}-a_l}\right)\left(\frac{-a_{l+1}^5}{120}+a_l\frac{a_{l+1}^4}{24}\right)\right)-C_\theta a_{l+1}-C_w\right) \\
&\quad - \frac{2}{a_{l+1}}\left(p_l\left(\left(\frac{1}{a_{l+1}-a_l}\right)\left(\frac{-a_{l+1}^4}{24}+a_l\frac{a_{l+1}^3}{6}\right)+\frac{a_{l+1}^3}{6}\right)+p_{l+1}\left(\left(\frac{-1}{a_{l+1}-a_l}\right)\left(\frac{-a_{l+1}^4}{24}+a_l\frac{a_{l+1}^3}{6}\right)\right)-C_\theta\right) \\
C_V &= \frac{2}{a_{l+1}^2}\left(p_l\left(\left(\frac{1}{a_{l+1}-a_l}\right)\left(\frac{-a_{l+1}^4}{24}+a_l\frac{a_{l+1}^3}{6}\right)+\frac{a_{l+1}^3}{6}\right)\right. \\
&\quad \left. +p_{l+1}\left(\left(\frac{-1}{a_{l+1}-a_l}\right)\left(\frac{-a_{l+1}^4}{24}+a_l\frac{a_{l+1}^3}{6}\right)\right)-C_M a_{l+1}-C_\theta\right)
\end{aligned}
\tag{B.14}
$$

B.0.3.4 Clamped-Simply Supported (CS)

C_θ and C_w take the same form as in Eqs. B.14.

$$
\begin{aligned}
C_V &= \frac{1}{a_{l+1}}\left(p_l\left(\left(\frac{1}{a_{l+1}-a_l}\right)\left(\frac{-a_{l+1}^3}{6}+a_l\frac{a_{l+1}^2}{2}\right)+\frac{a_{l+1}^2}{2}\right)+p_{l+1}\left(\left(\frac{-1}{a_{l+1}-a_l}\right)\left(\frac{-a_{l+1}^3}{6}+a_l\frac{a_{l+1}^2}{2}\right)\right)-C_M\right) \\
C_M &= \frac{3}{a_{l+1}^2}\left(p_l\left(\left(\frac{1}{a_{l+1}-a_l}\right)\left(\frac{-a_{l+1}^5}{120}+a_l\frac{a_{l+1}^4}{24}\right)+\frac{a_{l+1}^4}{24}\right)+p_{l+1}\left(\left(\frac{-1}{a_{l+1}-a_l}\right)\left(\frac{-a_{l+1}^5}{120}+a_l\frac{a_{l+1}^4}{24}\right)\right)\right. \\
&\quad -\frac{a_{l+1}^2}{6}\left(p_l\left(\left(\frac{1}{a_{l+1}-a_l}\right)\left(\frac{-a_{l+1}^3}{6}+a_l\frac{a_{l+1}^2}{2}\right)+\frac{a_{l+1}^2}{2}\right)\right. \\
&\quad \left.\left. +p_{l+1}\left(\left(\frac{-1}{a_{l+1}-a_l}\right)\left(\frac{-a_{l+1}^3}{6}+a_l\frac{a_{l+1}^2}{2}\right)\right)\right)-C_\theta a_{l+1}-C_w\right)
\end{aligned}
\tag{B.15}
$$

Bibliography

[1] E. Turco, "Tools for the numerical solution of inverse problems in structural mechanics: review and research perspectives," European Journal of Environmental and Civil Engineering, vol. 21, no. 5, pp. 509–554, 2017.

[2] D. K. Gupta and A. K. Dhingra, "Input load identification from optimally placed strain gages using D-optimal design and model reduction," Mechanical Systems and Signal Processing, vol. 40, no. 2, pp. 556–570, 2013.

[3] M. Zhang, B. Qiu, M. Zhu, and X. Qu, "Novel computation method of reducing ill-posedness for structural static distributed load identification by optimising strain gauge locations," Mechanical Systems and Signal Processing, vol. 124, pp. 83–110, 2019.

[4] A. Gallet, S. Rigby, T. N. Tallman, X. Kong, I. Hajirasouliha, A. Liew, D. Liu, L. Chen, A. Hauptmann, and D. Smyl, "Structural engineering from an inverse problems perspective," Proceedings of the Royal Society A: Mathematical, Physical and Engineering Sciences, vol. 478, no. 2257, p. 20210526, 2022.

[5] A. P. Ruybalid, J. P. M. Hoefnagels, O. van der Sluis, and M. G. D. Geers, "Comparison of the identification performance of conventional FEM updating and integrated DIC," International Journal for Numerical Methods in Engineering, vol. 106, no. 4, pp. 298–320, 2016.

[6] B. Lecampion and J. Gunning, "Model selection in fracture mapping from elastostatic data," International Journal of Solids and Structures, vol. 44, no. 5, pp. 1391–1408, 2007.

[7] F. Amiot, F. Hild, and J. Roger, "Identification of elastic property and loading fields from full-field displacement measurements," International Journal of Solids and Structures, vol. 44, no. 9, pp. 2863–2887, 2007.

[8] J. Waeytens, B. Rosić, P.-E. Charbonnel, E. Merliot, D. Siegert, X. Chapeleau, R. Vidal, V. le Corvec, and L.-M. Cottineau, "Model updating techniques for damage detection in concrete beam using optical fiber strain measurement device," Engineering Structures, vol. 129, pp. 2–10, 2016. SI: Structures Rehabilitation.

[9] A. Kefal, E. Oterkus, A. Tessler, and J. L. Spangler, "A quadrilateral inverse-shell element with drilling degrees of freedom for shape sensing and structural health monitoring," Engineering Science and Technology, an International Journal, vol. 19, no. 3, pp. 1299–1313, 2016.

[10] B. Shen, I. Stanciulescu, and G. H. Paulino, "Inverse computation of cohesive fracture properties from displacement fields," Inverse Problems in Science and Engineering, vol. 18, no. 8, pp. 1103–1128, 2010.

[11] M. Hashemi, R. Izadifard, and O. Yazdanpanah, "Experimental static data based damage localization of beam-like structures considering axial load," Inverse Problems in Science and Engineering, vol. 29, no. 12, pp. 1729–1745, 2021.

[12] I. T. Ardekani, J. Kaipio, and D. Castello, "Bayesian damage identification of simply supported beams from elastostatic data," Inverse Problems in Science and Engineering, vol. 29, no. 13, pp. 2895–2922, 2021.

[13] A.-J. Romppanen, Inverse load sensing method for line load determination of beam-like structures. PhD thesis, Oct. 2008. Awarding institution: Tampere University of Technology.

[14] A.-J. Romppanen, E. Keskinen, J. Miettinen, and V. Järvinen, "Line load determination of press rolls by inverse sensing method," in Proceedings of the 2005 SEM Annual Conference and Exposition on Experimental and Applied Mechanics, June 7 - 9, 2005, Portland, OR, USA, p. 9, 2005.

[15] A. Kobiske, Inverse Approaches for Recovery of Distributed Loads. Thesis, University of Wisconsin, Aug. 2015. Awarding institution: University of Wisconsin, Milwaukee.

[16] A. N. Tikhonov and V. Y. Arsenin, Solutions of Ill-Posed Problems. New York, NY: Wiley, 1977.

[17] A. Maniatty, N. Zabaras, and K. Stelson, "Finite element analysis of some inverse elasticity problems," Journal of Engineering Mechanics, vol. 115, no. 6, pp. 1303–1317, 1989.

[18] G. H. Golub and C. F. Van Loan, Matrix Computations (3rd ed.). Baltimore, MD: The Johns Hopkins University Press, 1996.

[19] T. Nakamura, H. Igawa, and A. Kanda, "Inverse identification of continuously distributed loads using strain data," Aerospace Science and Technology, vol. 23, no. 1, pp. 75–84, 2012.

[20] H. Liu, Q. Liu, B. Liu, X. Tang, H. Ma, Y. Pan, and J. Fish, "An efficient and robust method for structural distributed load identification based on mesh superposition approach," Mechanical Systems and Signal Processing, vol. 151, p. 107383, 2021.

[21] R. K. Kapania and J. Li, "A formulation and implementation of geometrically exact curved beam elements incorporating finite strains and finite rotations," Computational Mechanics, vol. 30, pp. 444–459, 2003.

[22] J. Li, Inverse Problems in Structural Mechanics. Dissertation, Dec. 2005.

[23] X. Cao, Y. Sugiyama, and Y. Mitsui, "Application of artificial neural networks to load identification," Computers & Structures, vol. 69, no. 1, pp. 63–78, 1998.

[24] L. Wang, Y. Liu, K. Gu, and T. Wu, "A radial basis function artificial neural network (RBF ANN) based method for uncertain distributed force reconstruction considering signal noises and material dispersion," Computer Methods in Applied Mechanics and Engineering, vol. 364, p. 112954, 2020.

[25] J. Li, J. Yan, J. Zhu, and X. Qing, "K-BP neural network-based strain field inversion and load identification for CFRP," Measurement, vol. 187, p. 110227, 2022.

[26] D. Wada, Y. Sugimoto, H. Murayama, H. Igawa, and T. Nakamura, "Investigation of inverse analysis and neural network approaches for identifying distributed load using distributed strains," Transactions of the Japan Society for Aeronautical and Space Sciences, vol. 62, no. 3, pp. 151–161, 2019.

[27] S. B. Cooper and D. DiMaio, "Static load estimation using artificial neural network: Application on a wing rib," Advances in Engineering Software, vol. 125, pp. 113–125, 2018.

[28] A. Baz and S. Poh, "Modal and physical deflections of beams using distributed wire sensors," Smart Materials and Structures, vol. 5, p. 261, jun 1996.

[29] P. Suh and D. Mavris, "Modal filtering for control of flexible aircraft," in 54th AIAA/ASME/ASCE/AHS/ASC Structures, Structural Dynamics, and Materials Conference, 2013.

[30] H.-P. Wang, C. Chen, Y.-Q. Ni, M. Jayawickrema, and J. Epaarachchi, "Computer-aided feature recognition of cfrp plates based on real-time strain fields reflected from fbg measured signals," Composites Part B: Engineering, vol. 263, p. 110866, 2023.

[31] A. Roknizadeh, A. Nobari, M. Mohagheghi, and H. Shahverdi, "Stability analysis of aeroelastic systems based on aeroelastic frf and condition number," Aircraft Engineering and Aerospace Technology, vol. 84, no. 5, pp. 299–310, 2012.

[32] M. Nikbay and P. Acar, "Aeroelastic predictions for steady and unsteady flow characteristics of the hirenasd wing," Progress in Computational Fluid Dynamics, an International Journal, vol. 16, no. 1, pp. 26–37, 2016.

[33] R. Davis, L. Virgin, and A. Brown, "Cylindrical shell submerged in bounded acoustic media: A modal approach," Aiaa Journal - AIAA J, vol. 46, pp. 752–763, 03 2008.

[34] J. C. French, "Nozzle acoustic dynamics and stability modeling," Journal of Propulsion and Power, vol. 27, no. 6, pp. 1266–1275, 2011.

[35] S. R. Fischbach, G. A. Flandro, and J. Majdalani, "Acoustic streaming in simplified liquid rocket engines with transverse mode oscillations," Physics of Fluids, vol. 22, p. 063602, 06 2010.

[36] B. K. Morris and R. B. Davis, "Optimal design of strain sensor placement for distributed static load determination," Inverse Problems, vol. 39, p. 125017, nov 2023.

[37] Y. Qin, Y. Zhang, and V. V. Silberschmidt, "Distributed dynamic load in structural dynamics by the impulse-based force estimation algorithm," CMES-Computer Modeling in Engineering & Sciences, vol. 139, no. 3, pp. 2865–2891, 2024.

[38] M. Blau, "Indirect measurement of multiple excitation force spectra by FRF matrix inversion: Influence of errors in statistical estimates of FRFs and response spectra," Acta Acustica united with Acustica, vol. 85, no. 4, pp. 464–479, 1999.

[39] P. Guillaume, E. Parloo, P. Verboven, and G. De Sitter, "An inverse method for the identification of localized excitation sources," in Proceeding of IMAC, 2002.

[40] P. C. Hansen, "Regularization tools: A matlab package for analysis and solution of discrete ill-posed problems," Numerical Algorithms, vol. 6, no. 1, pp. 1–35, 1994.

[41] A. M. Maniatty and N. J. Zabaras, "Investigation of regularization parameters and error estimating in inverse elasticity problems," International Journal for Numerical Methods in Engineering, vol. 37, no. 6, pp. 1039–1052, 1994.

[42] M. Casero, E. Covián, and A. González, "Regularization methods applied to noisy response from beams under static loading," Journal of Engineering Mechanics, vol. 146, no. 6, p. 04020038, 2020.

[43] A. Rezayat, V. Nassiri, B. De Pauw, J. Ertveldt, S. Vanlanduit, and P. Guillaume, "Identification of dynamic forces using group-sparsity in frequency domain," Mechanical Systems and Signal Processing, vol. 70-71, pp. 756–768, 2016.

[44] C. Pan, X. Ye, J. Zhou, and Z. Sun, "Matrix regularization-based method for large-scale inverse problem of force identification," Mechanical Systems and Signal Processing, vol. 140, p. 106698, 2020.

[45] W. Feng, Q. Li, Q. Lu, B. Wang, and C. Li, "Time domain force localization and reconstruction based on hierarchical bayesian method," Journal of Sound and Vibration, vol. 472, p. 115222, 2020.

[46] H. Zou and T. Hastie, "Regularization and variable selection via the elastic net," Journal of the Royal Statistical Society Series B: Statistical Methodology, vol. 67, pp. 301–320, 03 2005.

[47] A. Pereira, J. Antoni, and Q. Leclère, "Empirical bayesian regularization of the inverse acoustic problem," Applied Acoustics, vol. 97, pp. 11–29, 2015.

[48] G. K. Lopp and R. Schultz, "A Bayesian approach for identifying the spatial correlation of acoustic loads during vibroacoustic testing.," 1 2020.

[49] M. Aucejo and O. De Smet, "Bayesian source identification using local priors," Mechanical Systems and Signal Processing, vol. 66-67, pp. 120–136, 2016.

[50] M. Aucejo and O. De Smet, "On a full bayesian inference for force reconstruction problems," Mechanical Systems and Signal Processing, vol. 104, pp. 36–59, 2018.

[51] C. Faure, F. Ablitzer, J. Antoni, and C. Pézerat, "Empirical and fully Bayesian approaches for the identification of vibration sources from transverse displacement measurements," Mechanical Systems and Signal Processing, vol. 94, pp. 180–201, 2017.

[52] S. Luo, J. Jiang, F. Zhang, and M. S. Mohamed, "Distributed dynamic load identification of beam structures using a Bayesian method," Applied Sciences, vol. 13, no. 4, 2023.

[53] Z. Chen, S. Weng, H. Yu, J. Li, H. Zhu, Y. Yan, and L. Wu, "Bayesian-based method for the simultaneous identification of structural damage and moving force," Mechanical Systems and Signal Processing, vol. 185, p. 109742, 2023.

[54] M. S. Allen and T. G. Carne, "Delayed, multi-step inverse structural filter for robust force identification," Mechanical Systems and Signal Processing, vol. 22, no. 5, pp. 1036–1054, 2008.

[55] L. M. Zapata, W. Desmet, and F. Naets, "Validation of an impulse response filter for impact force reconstruction on a hammer drill," in Special Topics in Structural Dynamics & Experimental Techniques, Volume 5 (M. Allen, S. Davaria, and R. B. Davis, eds.), (Cham), pp. 51–56, Springer International Publishing, 2023.

[56] H. Devriendt, F. Naets, P. Kindt, and W. Desmet, "Inverse reconstruction of the spatial distribution of dynamic tire-road contact forces in time domain using impulse response matrix deconvolution for different measurement types," tech. rep., SAE Technical Paper, 2021.

[57] C.-D. Pan, L. Yu, H.-L. Liu, Z.-P. Chen, and W.-F. Luo, "Moving force identification based on redundant concatenated dictionary and weighted l1-norm regularization," Mechanical Systems and Signal Processing, vol. 98, pp. 32–49, 2018.

[58] Q. Li and Q. Lu, "A revised time domain force identification method based on bayesian formulation," International Journal for Numerical Methods in Engineering, vol. 118, no. 7, pp. 411–431, 2019.

[59] L. Zhang, S. Lyu, and J. Trinkle, "A dynamic bayesian approach to real-time estimation and filtering in grasp acquisition," in 2013 IEEE International Conference on Robotics and Automation, pp. 85–92, 2013.

[60] D. Teymouri, O. Sedehi, L. S. Katafygiotis, and C. Papadimitriou, "Data-driven reconstruction of dynamical forces and responses through bayesian expectation-maximization and modal reduction methods," Journal of Engineering Mechanics, vol. 149, no. 6, p. 04023030, 2023.

[61] D. Calvetti and E. Somersalo, "Inverse problems: From regularization to bayesian inference," WIREs Computational Statistics, vol. 10, no. 3, p. e1427, 2018.

[62] J. Weese, "A regularization method for nonlinear ill-posed problems," Computer Physics Communications, vol. 77, no. 3, pp. 429–440, 1993.

[63] M. Aucejo, O. De Smet, and J.-F. Deü, "Practical issues on the applicability of kalman filtering for reconstructing mechanical sources in structural dynamics," Journal of Sound and Vibration, vol. 442, pp. 45–70, 2019.

[64] F. Naets, J. Cuadrado, and W. Desmet, "Stable force identification in structural dynamics using kalman filtering and dummy-measurements," Mechanical Systems and Signal Processing, vol. 50-51, pp. 235–248, 2015.

[65] E. Lourens, E. Reynders, G, G. Degrande, and G. Lombaert, "An augmented kalman filter for force identification in structural dynamics," Mechanical Systems and Signal Processing, vol. 27, pp. 446–460, 2012.

[66] R. Álvarez Briceño and L. P. de Oliveira, "Combining strain and acceleration measurements for random force estimation via kalman filtering on a cantilevered structure," Journal of Sound and Vibration, vol. 469, p. 115112, 2020.

[67] G. Reina and A. Messina, "Vehicle dynamics estimation via augmented extended kalman filtering," Measurement, vol. 133, pp. 383–395, 2019.

[68] F. Naets, R. Pastorino, J. Cuadrado, and W. Desmet, "Online state and input force estimation for multibody models employing extended kalman filtering," Multibody System Dynamics, vol. 32, no. 3, pp. 317–336, 2014.

[69] W. Feng, Q. Li, and Q. Lu, "Force localization and reconstruction based on a novel sparse kalman filter," Mechanical Systems and Signal Processing, vol. 144, p. 106890, 2020.

[70] C. Zhang, J.-Z. Huang, G.-Q. Song, and L. Chen, "Structural damage identification by extended kalman filter with l1-norm regularization scheme," Structural Control and Health Monitoring, vol. 24, no. 11, p. e1999, 2017. e1999 STC-16-0111.R2.

[71] Y. Wang and W.-L. Qu, "Moving train loads identification on a continuous steel truss girder by using dynamic displacement influence line method," International Journal of Steel Structures, vol. 11, no. 2, pp. 109–115, 2011.

[72] H. Wang, Q. Zhu, J. Li, J. Mao, S. Hu, and X. Zhao, "Identification of moving train loads on railway bridge based on strain monitoring," Smart Struct. Syst, vol. 23, no. 3, pp. 263–278, 2019.

[73] L. Yu and T. H. Chan, "Recent research on identification of moving loads on bridges," Journal of Sound and Vibration, vol. 305, no. 1, pp. 3–21, 2007.

[74] S. Pourzeynali, X. Zhu, A. Ghari Zadeh, M. Rashidi, and B. Samali, "Comprehensive study of moving load identification on bridge structures using the explicit form of newmark-β method: Numerical and experimental studies," Remote Sensing, vol. 13, no. 12, 2021.

[75] S. Law, T. Chan, and Q. Zeng, "Moving force identification: A time domain method," Journal of Sound and Vibration, vol. 201, no. 1, pp. 1–22, 1997.

[76] Z. Hu and Z. Xiang, "Noise-enhanced effect in moving dynamic force identification," Journal of Sound and Vibration, vol. 557, p. 117742, 2023.

[77] S. S. Law, T. H. T. Chan, and Q. H. Zeng, "Moving force identification—a frequency and time domains analysis," Journal of Dynamic Systems, Measurement, and Control, vol. 121, pp. 394–401, 09 1999.

[78] L. Yu and T. H. Chan, "Moving force identification based on the frequency–time domain method," Journal of Sound and Vibration, vol. 261, no. 2, pp. 329–349, 2003.

[79] Z. Chen, T. H. Chan, and L. Yu, "Comparison of regularization methods for moving force identification with ill-posed problems," Journal of Sound and Vibration, vol. 478, p. 115349, 2020.

[80] S. Boyd and L. Vandenberghe, Convex Optimization, ch. 4.2.2, pp. 138–139. The Edinburgh Building, Cambridge, CB2 2RU, UK: Cambridge University Press, 1 ed., Dec. 2004.

[81] M. R. Bonyadi and Z. Michalewicz, "Particle Swarm Optimization for Single Objective Continuous Space Problems: A Review," Evolutionary Computation, vol. 25, pp. 1–54, 03 2017.

[82] G. Albertin, "Piecewise linear least square fit," 2022.

[83] L. S. Rolls, "Comparison between flight-measured and calculated span load distribution at high mach numbers," Tech. Rep. RM No.A7G17, NACA, Ames Aeronautical Laboratory, Moffett Field, California, November 1947.

[84] P. C. Hansen, "Regularization tools version 4.0 for matlab 7.3," Numerical Algorithms, vol. 46, no. 2, pp. 189–194, 2007.

[85] K. Liu, R.-J. Yan, and C. Guedes Soares, "Optimal sensor placement and assessment for modal identification," Ocean Engineering, vol. 165, pp. 209–220, 2018.

[86] J. Lollock, The Effect of Swept Sinusoidal Excitation on the Response of a Single-Degree-of-Freedom Oscillator. 2002.

[87] K. Coletti, S. Carter, and R. Schultz, "Local modeling for FRF estimation with noisy input measurements," Journal of Sound and Vibration, vol. 576, p. 118289, 2024.